Chair of Physical Metallurgy and Metallic Materials

Master's Thesis

Lukas Walch, BSc

March 2021

Damage initiation in hard-coated hard metal substrates under normal and tangential loads at elevated temperature

Lukas Walch, BSc.

Thesis in partial fulfilment of the requirements for the degree of a

Master of Science (MSc)

at the University of Leoben

Leoben, March 21

EIDESSTATTLICHE ERKLÄRUNG

Ich erkläre an Eides statt, dass ich diese Arbeit selbständig verfasst, andere als die angegebenen Quellen und Hilfsmittel nicht benutzt, und mich auch sonst keiner unerlaubten Hilfsmittel bedient habe.

Ich erkläre, dass ich die Richtlinien des Senats der Montanuniversität Leoben zu "Gute wissenschaftliche Praxis" gelesen, verstanden und befolgt habe.

Weiters erkläre ich, dass die elektronische und gedruckte Version der eingereichten wissenschaftlichen Abschlussarbeit formal und inhaltlich identisch sind.

Datum 30.03.2021

Unterschrift Verfasser/in
Lukas Walch

Acknowledgments

Here, I want to take a moment to thank those who made this thesis possible. Firstly, I want to thank Prof. Dr. Reinhold Ebner who acted as my academic supervisor in spite of his numerous other duties. I also want to express my gratitude to Dr. Thomas Klünsner, who was my technical supervisor and always had time for discussions, regarding any detail or problem. Likewise, I want to thank DI Kathrin Maier, who took what time she had left to give to participate in lengthy discussions. I am also excessively grateful to the MCL team and everyone who helped me, in particular Dr. Philip Pichler and Dr. Julian Wagner, without whom I would have been lost among the various machines I needed.

In particular, I also want to thank all my family; that is, my parents, my sister and last but not least my girlfriend, who supported me throughout my studies and made everything possible.

Table of contents

List of Abbreviations

Chemical elements and compounds

Here all chemical elements and compounds mentioned in the text body are listed. In the text, they are introduced in the form of e.g. tungsten (W) and afterwards used in abbreviated form.

W	Tungsten
C	Carbon
WC	Tungsten carbide
Co	Cobalt
TiC	Titanium carbide
TaC	Tantalum carbide
B	Boron
TiN	Titanium nitride
TiB_2	Titanium diboride
WO_3	Tungsten trioxide
$CoWO_4$	Cobalt tungstate
CO_2	Carbon dioxide

Terminology

In the following all technical terms either used repeatedly in the text body or in equations are listed. They are introduced identically as chemical elements but are, in contrast, given in italics.

BIC	ball-in-cone (test/ test setup)
FE	Finite element (simulation)
R_{metal}	Atomic radius of a metal

$R_{non\text{-}metal}$	Atomic radius of a non-metal
FCC	Face-centered cubic (lattice)
HCP	Hexagonal close-packed (lattice)
α_t	Thermal expansion coefficient
λ	Thermal conductivity
LEFM	Linear elastic fracture mechanics
K	Stress intensity factor
K_{IC}	Critical stress intensity factor (mode 1)
σ	Stress
RT	Room temperature
R-curve	Crack-growth resistance-curve
PVD	Physical vapor deposition
CVD	Chemical vapor deposition
ROI	Region of interest
R	Stress ratio
P1	Central position
P2	Outer-fringe position
P3	Inner-fringe position
FIB	Focused ion beam
SEM	Scanning electron microscope / microscopy
SE	Secondary electron (contrast mode)
EBS	Electron back-scatter (contrast mode)

$D\beta$--	Abbreviation for specimen type (with added number)
$\emptyset_{max}$	Maximum measurable diameter
ND	Size category: Nanodefect ($\emptyset_{max}$ < 0.1 µm)
MD	Size category: Microdefect (0.1 µm < $\emptyset_{max}$ < 1 µm)
TI	Shape category: $\emptyset_{max} \geq 3* \emptyset_{min}$
TII	Shape category: $\emptyset_{max} < 3* \emptyset_{min}$
TIII	Shape category: Hybrid of TI and TII shape
D	Size category: Defect ($\emptyset_{max}$ > 1 µm)
C_{WC}	Contiguity of tungsten carbide
$\bar{C}_{WC}$	Average of contiguity values of tungsten carbide
$S_{WC/WC}$	WC to WC interface area in a specimen
$S_{WC/Co}$	WC to Co interface area in a specimen
$N_{WC/WC}$	Number of WC to WC transitions along a line in a cross-section
$N_{WC/Co}$	Number of WC to Co transitions along a line in a cross-section
Std	Standard deviation
l_{Co}	Mean free path in cobalt
th_{Co}	Thickness of cobalt sections along a line in a cross-section
N_{Co}	Number of cobalt sections along a line in a cross-section

Kurzfassung

In der metallverarbeitenden Industrie gehören WC-Co Hartmetalle zu den wichtigsten Werkstoffen für Werkzeuge. Sie werden zum Beispiel zum Fräsen höchstfester Materialien genutzt. Ihre Lebendsauer wird aber oft durch Defekte im Hartmetallsubstrat begrenzt. Zu den Hauptgründen für Defektinitiation und -wachstum zählen die signifikanten, multiaxialen Lasten und hohen Temperaturen an den Schnittkanten solcher Fräswerkzeuge. Derzeit gibt es einen Mangel an Testmethoden, die diese Bedingungen kontrolliert nachstellen können. In dieser Arbeit nutzt ein neuartiger Ball-in-Cone Test einen sphärischen Indenter und eine geneigte Probenoberfläche zur Aufbringung multiaxialer zyklischer Lasten in einer Vakuumkammer bei 700 °C. Mit diesem Aufbau wurden mit TiN-TiB$_2$ hartbeschichtete WC-12 wt. % Co Hartmetallproben mit einer durchschnittlichen Karbidkorngröße von 2 µm hinsichtlich ihres Kontaktermüdungsverhaltens geprüft. Die Gefüge der Proben wurden im Rasterelektronenmikroskop an mittels fokussiertem Ionenstrahl eingebrachten Schnitten dokumentiert. Die im Substrat auftretenden Spannungen wurden mit einer Finite Elemente Simulation untersucht. Dazu wurde ein das Kriechverhalten berücksichtigendes und experimentell parametrisiertes Materialmodell genutzt. Die Simulation ergab Spannungen, die vom reinen Druckbereich bis hin zu Zug-Druckspannungen reichten. Trends in der Defektentwicklung bis zu 10.000 Lastzyklen wurden mit der eingebrachten Mittelspannung in Verbindung gebracht. Eine Mischung aus zyklisch eingebrachten Zug-Druckspannungen führte immer zu einer höheren Defektanzahl als reine Druckspannungen. Mit dem Ball-in-Cone Test kann so die Schadensinitiation in multiaxialen Lastsituationen bei hohen Temperaturen untersucht werden.

Abstract

In the manufacturing industry, WC-Co hard metals are among the most important tool materials. They are used for machining applications like the milling of high-strength materials. Their lifespan is often limited by defects in the hard metal substrate. Among the main causes for defect initiation and growth are the significant multi-axial loads and high temperatures present e.g. at the cutting edge of milling inserts. Presently there is a lack of testing methods capable of reproducing such conditions in controlled environments. In the current work a novel ball-in-cone test setup utilizes a spherical indenter and an inclined sample surface to introduce cyclic multi-axial loads into the specimen substrate in isothermal conditions. The setup is used to study the contact fatigue behavior of TiN-TiB$_2$ hard-coated WC-12 wt.% Co hard metal specimens with a mean grain size of 2 µm. Cyclic loads of a level comparable to that seen at the cutting edge of milling tools were applied to tested specimens at a temperature of 700 °C induced via eddy current heating in a vacuum. The specimens' microstructures were documented using scanning electron microscopy on sections exposed via focused ion beam milling. The stress situation in the specimen substrate was studied with a finite element simulation using an experimentally parameterized materials model also considering creep. The simulation showed stresses ranging from mainly compressive to tensile-compressive. Defect formation trends at up to 10,000 load cycles could be correlated with the applied stress ratio. Positions subjected to a combination of tensile and compressive stresses showed a significantly higher defect formation rate than positions with mainly compressive stresses. The defect initiation behavior in specimens under multi-axial loads at elevated temperature can be studied using the ball-in-cone test method.

1. Introduction

Almost a century has passed since the first industrial application of a tungsten carbide-cobalt (WC-Co) hard metal metalworking tool [1], [2, pp. 3–4]. Since then, the importance of these WC-Co hard metals has increased significantly; their unique mechanical strength and wear resistance enabled and fueled ever-improving manufacture and processing of metals and alloys of increasing strength [1]. In recent decades, the fatigue behavior of WC-Co hard metals has seen increased attention [3]–[8]. The modern drive towards tool-life optimization lead to a growing focus on damage initiation and crack propagation [9]–[15].

At the beginning of the current work a theoretical examination of the studied material with respect to current literature is given. The focus lies on the WC and Co system, the failure mechanisms of WC-Co hard metals and their applications. The main part of the presented work considers a novel test method, the *ball-in-cone* (*BIC*) test setup, which is proposed as a means to study damage initiation mechanisms in hard coated specimen. Besides the concept design, a standard methodology for use of the ball-in-cone test will be proposed as guideline for future applications. In addition to experiments, a finite element simulation by *Krobath* [16] will be discussed with a focus on the implications for the practical application of the test. Using the *BIC* test, the damage initiation in the substrate of TiN-TiB$_2$ hard-coated WC-12 wt.% Co hard metal specimen with a mean grain size of 2 μm was studied with the results presented and discussed in the following. The core questions of this thesis regarding the usability of the test, the validity of the simulation and the observed material behavior will subsequently be addressed.

2. Hard metals

Since the first inception of tungsten carbide in 1893 by H. Moissard [17, p. 2] hard metals or, in English literature, "Cemented Carbides" [2, pp. 3–4] revolutionized the field of high-performance materials. The greatest impact was on the market of machining tools from the presentation of the first commercial hard metal "WIDIA" by the Friedrich Krupp AG at the Leibzig Spring Fair in 1927 onwards [1], [2, pp. 3–4]. Those tools enabled a significant increase in cutting speeds in machining processes as well as the efficient machining of hard cast iron and steels [18, p. 120]. Today, they can rightfully be considered the foundation of the tool manufacturing industry [19, pp. 29–30]. This was possible due to the unique make-up and the resulting material properties of hard metals, which are discussed in this chapter.

2.1. Tungsten carbide and cobalt as a composite

A hard metal is a composite material made up of a hard and brittle carbide or nitride phase and a softer, more ductile binder phase cementing the carbide grains together [18, p. 121], hence the term "cemented carbides" [20, p. 215]. The first commonly used hard metal was tungsten carbide (WC) with cobalt (Co) as binder phase. Other compositions like titanium carbide with a nickel binder phase have been developed and are in use for special applications [19, p. 38]. They were developed for applications unsuited for WC hard metal tools and also because Co is considered possibly carcinogenic [18, p. 120], [21]. Still, WC-Co still makes up the bulk of the produced mass of hard metals [1]. This is because, despite the higher cost of tungsten, WC-Co offers excellent mechanical properties in a wide temperature range [1], [17, pp. 1–2], [22], [23].

2.1.1. The WC-Co pseudo-binary phase system

The tungsten - carbon (*W-C*) system shows several distinct phases stable at high temperatures in certain concentration ranges. However, at room temperature and at temperatures up to 1200 °C only the δ-WC phase, also referred to as simply WC phase, is stable [17, p. 6], [24]. As first proposed by Hägg, nonstoichiometric interstitial compounds are formed when the atomic radii of a metal (R_{metal}) and a non-metal ($r_{non-metal}$) form a ratio $r_{non-metal}/R_{metal}$ with a value from 0.41 to 0.59 [17, p. 5], [25, p. 154]. Since carbon (C) has an atomic radius of 70 pm and tungsten (W) one of 135 pm [26], the relevant ratio of 0.519 fulfills that condition.

Therefore, the WC phase is a Hägg phase. It features the typical high stability of such interstitial compounds. W arranges in a simple hexagonal lattice with two atoms per unit cell and C occupies the trigonal prismatic interstitial positions of the W-sublattice [17, pp. 19–21], [27], [28, pp. 94–97]. Figure 1 *(a)* outlines the structure of a unit cell and Figure 1 *(b)* that of an WC crystal in equilibrium [27].
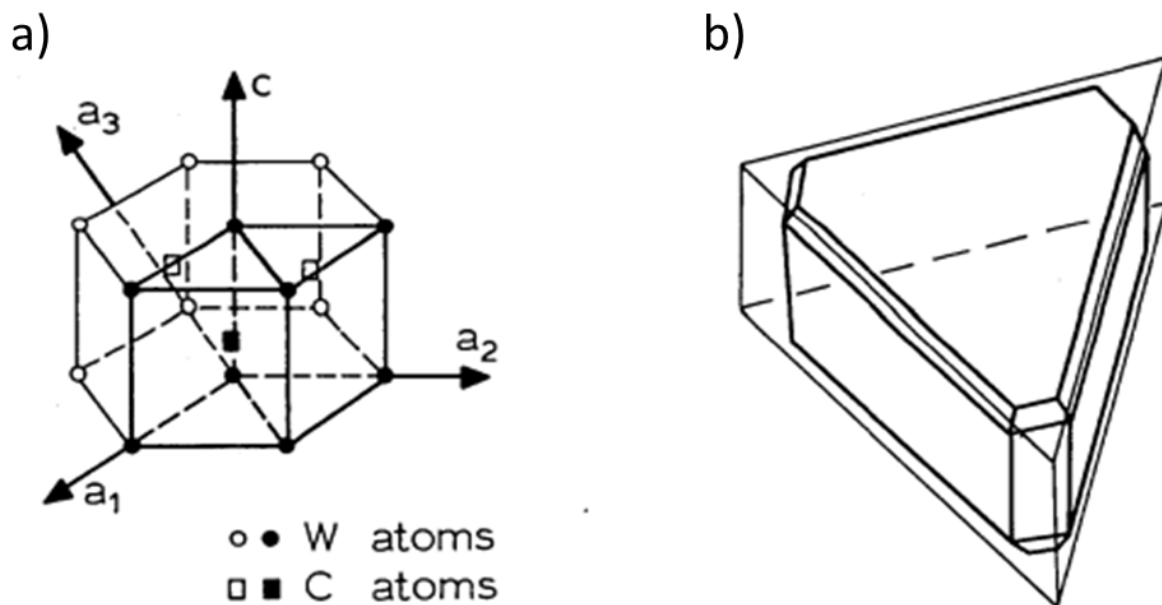
Figure 1: Visual representation of the WC unit cell and equilibrium crystal by Exner in [27]. *(a) The WC unit cell. (b) A schematic approximation to an equilibrium crystal.*

Cobalt is a relatively rare ferromagnetic metal with a high-temperature *face-centered-cubic* (*FCC*) phase above 417 °C and a low-temperature *hexagonal-close-packed* (*HCP*) phase below that temperature [29]–[31]. In respect to hard metals, it is the most commonly used binder material; particularly so with WC, in part because of its high solubility of W and C and the superior mechanical properties of the composite [17, pp. 25–28]. One of the main advantages of Co as a binder phase for WC is its ability for wetting the carbide grains due to the sufficiently low surface interfacial energy of WC and Co phases [28, pp. 93–97]. Additionally, the ferromagnetic behavior of Co allows for a nondestructive evaluation of the WC-Co hard metal composition through coercivity measurement [19, pp. 39–40]. A partial replacement of the Co binder phase with iron or nickel yields harder and tougher compounds respectively, albeit always with lower strength. They are used mainly in specialized applications [19, p. 39].

Although W-C-Co is a ternary system with complex carbide phases and ternary compounds in a wide range of temperatures, the system acts in a "pseudo-binary" way [17, pp. 25–28] when the correct stoichiometry is adhered to. Following *Kurlov and Gusev*, this leads from what can be seen in *Figure 2 (a)* to the phase diagram along the binary WC-Co cross section of the ternary system, shown in *Figure 2 (b)* as presented in [17, p. 27]. As has been mentioned, pure Co has a hexagonal lattice at *RT*.
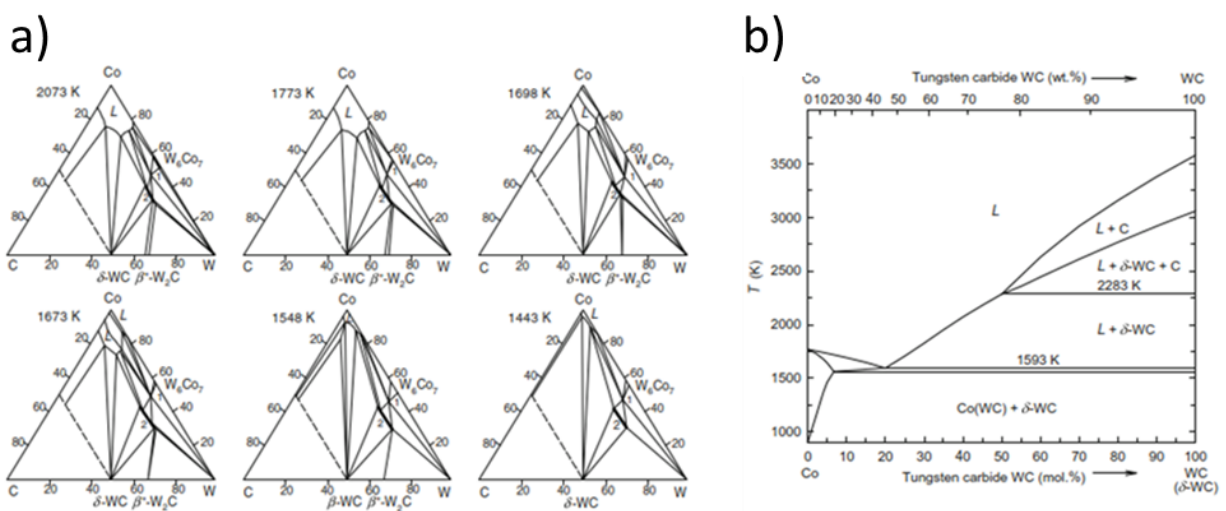
Figure 2: The ternary W-C-Co system as discussed in [17, p. 27] is shown. (a) Cross-sections of the ternary W-C-Co system at various temperatures presented by [17, p. 27]. (b) The binary section of the ternary system, i.e. a cut along the WC-Co cross section.

As can be seen in *Figure 2 (b)*, Co is largely insoluble in the carbide phase. The latter in turn shows a solubility in the binder metal of up to 10 % at ~ 1230 °C. The content of the binder phase is in most WC-Co hard metals between 0 and 30 wt. % [1], [19, pp. 39–40]. In recent decades the addition of so-termed mixed carbides gained traction because of their hardness improving and grain growth inhibiting tendencies [32, pp. 501–503]. However, the content of those mixed carbides typically does not exceed 3 % [19, p. 37].

The microstructure of WC-Co hard metals is fairly unique. The WC grains often exhibit rigid geometric shapes, embedded in a Co matrix. This matrix is mainly dependent on the Co content (either as volume fraction [33] or weight percentage [19, pp. 39–40]), but other carbides used as additives also influence the appearance of the microstructure [34]. Albeit not all WC-Co hard

metals share the same microstructure, most exhibit certain similarities. Representatively, *Figure 3*, originally presented in [34], aptly visualizes the main variations in microstructure of WC-Co hard metals.
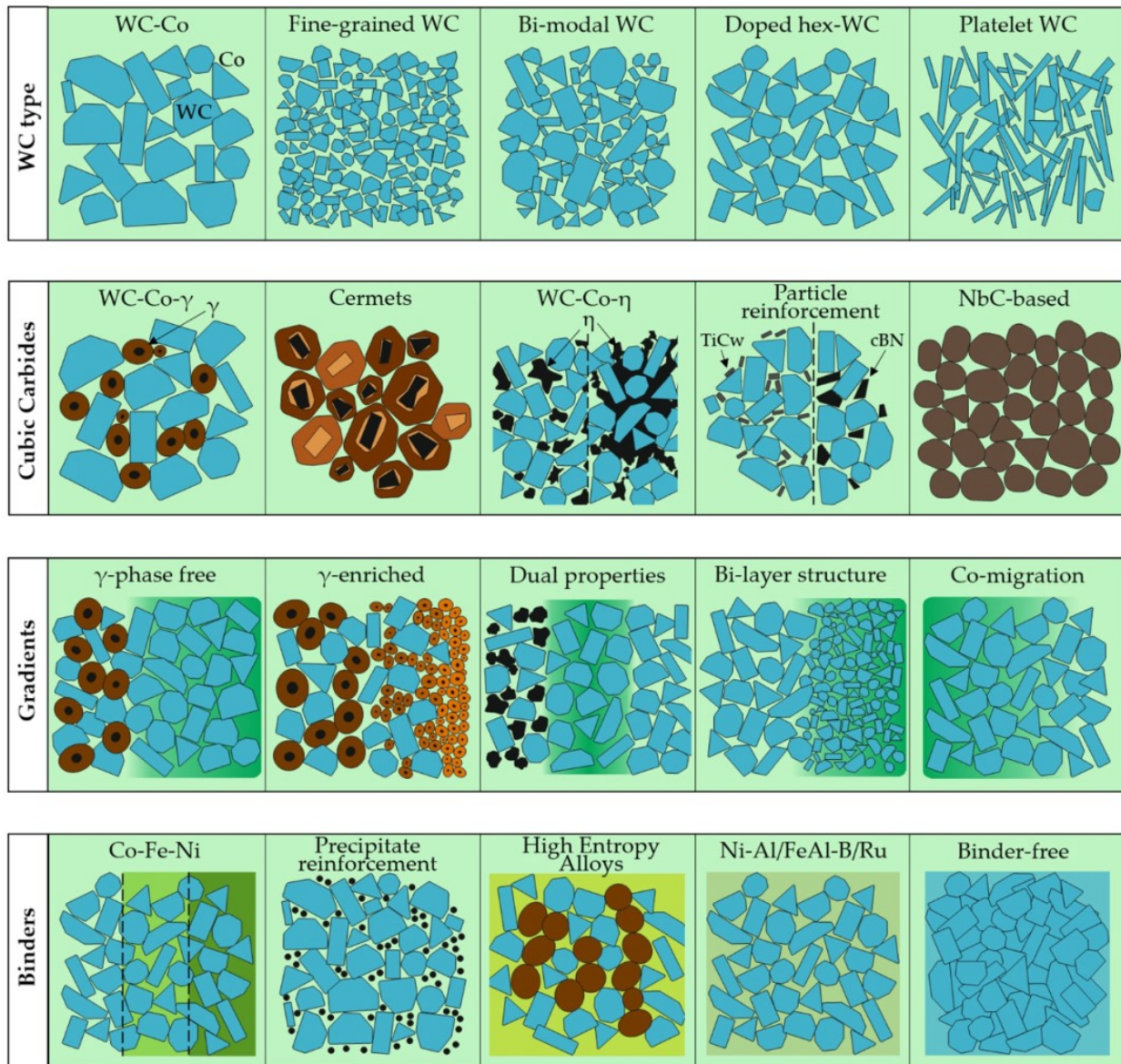
Figure 3: This illustration by Garcia et al. *in* [34] *provides an overview of several typical WC-Co hard metal microstructures. The microstructures are grouped by causal factors for the respective microstructures. The γ-phase denotes the presence of cubic carbides. The η-phase represents a sub-stoichiometric WC-phase found in WC-Co hard metals with a low carbon content* [34].

2.1.2. Physical properties of WC-Co hard metals

The particular nature of the WC-Co hard metals results in properties making the composite well-suited for applications with extreme mechanical or thermal conditions. For example, regardless of the Co content, no liquid phase is present until well above 1200 °C in the WC-Co pseudo-binary phase system [17, p. 27]. Thermal expansion is linearly proportional on the Co content [35]. The *thermal expansion coefficient* (α_t) consistently remains small compared to high-strength steels, as e.g. described by *Kieffer* in [32, p. 179] and later *Chawla* in [36, pp. 352–358]. The *thermal conductivity* (λ) of WC-Co hard metals is inversely proportional to the Co content. For most WC-Co hard metals, λ is two to three times as high as it is for high-strength steels [32, p. 178], [35]. The combination of these properties makes WC-Co hard metals ideally suited for many high-temperature applications, since it remains stable in form and composition while at the same time draining excess heat from its source.

Hard metals exhibit a strong dependency of their mechanical properties on their microstructures. A close relation to the phase composition (i.e. the Co content) as well as the distribution of the carbide phase in the Co matrix and the mean grain size has been found [28, p. 91]. Notably, WC-Co hard metals are brittle materials with limited plastic behavior for most compositions and specimen sizes [19, pp. 43–47], [37], [38], [39, pp. 412–416]. Their respective mechanical properties depend on the size of the loaded volume, with large loaded volumes showing considerably lower strength values than small loaded volumes [40]. This is due to the size-effect in brittle materials and can be explained by the fact that in a material showing little to none plastic deformation, fracture at a singular critical defect can lead to failure of the whole specimen [41]. Such critical defects can be estimated using the linear elastic fracture mechanics (*LEBM*) [42, pp. 69–119] by referring to the *fracture toughness* (K_{IC}), which is the *stress intensity* (K) at which unstable crack growth occurs [43, pp. 399–400]. Since K is directly proportional to the *applied stress* (σ) and to the square root of the defect size, K_{IC} can be exceeded either by increasing σ or the size of defects. Consequently, the defect size is important for most applications in which WC-Co hard metals are used.

Typically, WC-Co hard metals are tougher than pure ceramics, which mostly show K_{IC} values of 3 to 5 MPa√m [44]. Compared to metal alloys such as martensitic steels with K_{IC} values

often above 100 MPaVm [45], [46], WC-Co hard metals are very brittle. Their fracture toughness mostly does not exceed 26 MPaVm at *room temperature* (*RT*) [47, p. 317]. Regarding this lack of toughness of WC-Co hard metals in consideration of the size effect, it can be concluded that with the size of the loaded volume, the probability of a critical defect existing in that volume increases. This makes the measurement of e.g. ultimate tensile strengths a difficult endeavor and usually necessitates the use of Weibull statistics to reliably describe fracture strength distributions [37]. An additional influence on the mechanical properties can be found in the content of Co as well as in the WC mean grain size. A higher binder metal content reduces mechanical strength but increases the toughness [18, pp. 120–125]. Reducing the carbide's mean grain size usually results in improved hardness, generally at the cost of toughness [17, pp. 191–193], [18, pp. 120–125].

The mechanical strengths of hard metals are indisputably in the high-strength spectrum of known materials. *Klünsner et al.* e.g. measured tensile strength values of above 2,000 MPa for WC-Co hard metals with a Co content of above 8 wt. % and mean grain sizes in the submicron spectrum at *RT*. By significantly decreasing the size of the loaded volume, they observed an increase of those strength values to about 6,000 MPa [40]. Like most materials, WC-Co hard metals show a greater ultimate compressive than tensile strength. In the case of WC-Co hard metals it is approximately three times the value of tensile strength [19, pp. 43–47], [32, p. 175].

In combination with their mechanical properties and relatively high toughness compared to ceramics [44], [48], their high hardness is one of the key advantages of WC-Co hard metals. That is because hardness, defined as the resistance of a material against plastic surface deformation, has a significant influence on the wear resistance of a material [32, pp. 160–167], [43, p. 120], [49, pp. 363–364]. In research work, the Vickers method for hardness measurement is considered a standard method because it can measure a broad spectrum of materials, from soft to hard, without requiring a change of the indenter [43, p. 140]. It is therefore a useful tool in evaluating the hardness of WC-Co hard metals. The Vickers hardness of WC-Co hard metals usually measures above 1,000 HV and is inversely proportional to the content of the binder metal and the mean grain size of the carbide phase [50], [51], [52, p. 127]. A WC-Co hard metal with a low Co content and small mean grain size can show a Vickers hardness of about 2000 HV [50].

As has been indicated, WC-Co hard metals are widely used in applications exhibiting very high temperatures, up to and above 1,000 °C [39, p. 405], [53, pp. 426–430]. A good understanding of their mechanical properties at those conditions is therefore essential. Findings show that with an increase in temperature, most mechanical properties, like hardness, Young's modulus and strength, degrade while the fracture toughness increases [39, pp. 408–412], [48]. Contrary to the mostly brittle behavior of WC-Co hard metals at *RT*, a significant increase in plastic deformation and ductile behavior has been observed at sufficiently high temperatures [48], [54].

Pure tungsten, albeit chemically mostly inert towards oxygen at *RT*, shows strong oxidation reactions at elevated temperatures. Pure carbon shows similar behavior at lower temperatures [55, pp. 431–432], [56], [57]. Their chemically most stable oxides are tungsten trioxide (*WO$_3$*) [57] and carbon dioxide (*CO$_2$*) [55, p. 433]. Considering this, it is to be expected that WC shows similar oxidation behavior, which was investigated in [57], [58]. *Webb et al.* found an increased oxidation rate for WC at temperatures above 700 °C compared to pure W [59].

It is a well-established fact that WC-Co hard metals are often used in high-temperature applications, e.g. as tools in machining processes [18, pp. 104–107]. The oxidation behavior of WC-Co hard metals is therefore of great interest to WC-Co hard metal manufacturers and several studies were performed e.g. by *Basu et al*. [60]., *Gu et al.* [58]. and *Chen et al.* [61]. The respective authors concluded that below 600 °C, the oxidation of their WC-Co hard metal specimens was negligible, with a marked increase above 700 °C and at heightened oxygen contents. An increase of the Co content observed a decrease in the oxidation rate [62]. The only solid oxide phases identified were WO$_3$ and CoWO$_4$, with their concentration ratios solely dependent on the content of the binder metal in the composite [60]. *Chen et al.* proposed an oxidation model for WC-Co hard metals which distinguished three distinctive temporal regions. In this model, a phase of little or no oxidation is followed by selective oxidation of the oxygen-exposed Co, characterized by the formation of CoWO$_4$-scales. In the final stage a WO$_3$-rich oxide layer forms [61].

Such inhomogeneous oxidation behavior conclusively explains the degradation of some mechanical properties like bending strength due to reduced surface integrity and introduced microstructural defects [63]. The oxidation behavior of WC-Co hard metals should therefore always be considered in the use of those composites at high temperatures. It is only logical that

many WC-Co hard metal manufacturers utilize oxidation-resistant coatings to enhance the life-time of their product [2, p. 20], [18, pp. 119–125], [58].

2.1.3. Manufacture of WC-Co hard metals

The manufacture of WC-Co hard metals is no simple task. This is largely due to their composite nature; a simple alloying process of carbide and metal is not possible. Hence, smelting is neither economically nor physically viable. From the beginning, a powder metallurgical approach had been chosen for the production of both, WC powder and WC-Co hard metals [2, p. 5], [17, pp. 34–36]. A conventional method for the synthesis of WC powder is the reduction of WO_3 by carbon at high temperatures in an inert or reductive atmosphere [17, pp. 34–36].

For further processing, powder quality is critical [20, pp. 219–222]. It is either achieved during powder synthesis or through subsequent powder granulation. Once a sufficient powder quality is achieved, it is subjected to green shaping. It is pressed to an acceptable density and into a form which it keeps owing to a fugitive, usually organic, binder system [20, p. 226]. This is done in a variety of ways, depending on the product's geometric complexity as well as the cost per piece. There is uniaxial pressing for simple pieces, utilizing one axis for pressure application [20, pp. 227–230]; cold isostatic pressing for large parts, utilizing homogenous pressure application to the outer workpiece surface and also powder injection molding for complex pieces where the powder is forcibly injected into a pre-formed mold [20, pp. 230–233]. After the initial shaping, the green body is usually post-processed; this ranges from minor adaptations to significant material removal. The main aim is to achieve a shape rather close to the final shape to limit post-processing, because the green body possesses only a fraction of the mechanical strengths of the final product after sintering [20, pp. 226; 233–234].

WC-Co hard metal is usually manufactured via sintering processes. For this purpose, carbide and metallic powder are mixed together in the appropriate composition and heated to a temperature below their respective melting points. The elevated temperature increases the diffusion rates and particle cohesion is achieved [64, pp. 238–240]. For improved product quality a liquid-phase sintering process is used with Co in the liquid state, because the melting point of Co is much lower than the decomposition point of WC (1459 °C compared to 2790 °C [17, pp. 1–

3], [65, pp. 9–10]). This takes full advantage of the wetting ability of Co respective to WC grains and forms a cohesive composite with very low porosity [64, pp. 238–240].

As in many cases, the possibility of the direct manufacture of WC-Co hard metal tools and workpieces is an attractive one. As a consequence, additive manufacturing processes using e.g. the selective electron beam melting [66] and binder jetting [67] methods have already been proposed and studied, with promising results.

Whatever the manufacture route, one lingering effect is common to all, i.e. residual stresses between binder and carbide phases. In general, residual stresses are classified as macrostresses or microstresses. The former equilibrates over at least a major part of the scale of a body and arises e.g. with deformation treatments. The microstresses are comparatively local and have measurable influence over several grains. There also exists a third class of short-ranged microstresses limited to a single grain and caused by plastic deformation [68, pp. 385–386]. The farther-reaching kind of microstresses on the other hand is a result of local differences in thermal expansion, e.g. due to a temperature gradient. For WC-Co hard metals, their main cause lies in the cooling period after sintering and notable differences in the α_t of carbide and binder metal. The characteristics of these residual stresses are described in [69] as follows: They are of significant magnitude albeit broadly distributed, especially in the Co phases. The residual stresses show mean tension in the binder and mean compression in the carbide. They also have been shown to interfere with applied stress. This can partially explain the unusual toughness of WC-Co hard metals.

2.2. Failure of WC-Co hard metals

The failure of materials is a complex and multifaceted process which includes multiple mechanisms, each dominant in different conditions, and each dependent on varying factors [70]. This is also true for WC-Co hard metals, which are a composite of a hard ceramic and a softer metal phase [18, p. 121], [32, pp. 240–259]. They show a mostly brittle behavior with limited ductility at *RT*; ductility increases with temperature [39, pp. 408–412], [71]. In addition, they exhibit creep when loaded at elevated temperatures for a prolonged time period [71], [72]. Some of the mechanisms governing the damaging and subsequent failure of WC-Co hard metals will be discussed in the following pages.

2.2.1. Damage initiation in WC-Co hard metals at room temperature

The influence of microstructure on the material behavior of WC-Co hard metals is significant [28], [73], [74]. It was found that the *contiguity parameter* (C_{WC}) and the content of Co in the composite have great influence on the deviation of the composite from linear-elastic behavior [33]. Contiguity is used to describe the WC-Co microstructure; i.e. the fraction of the total carbide grain surface area of carbide grains in direct contact with other carbide grains [28, pp. 107–110], [75]. Assuming that WC/Co to WC/WC interfaces are related to the Co content, it is an approximate function of the binder phase content [28, pp. 107–110]. At low contiguity, the load was found to also be dispersed in the binder, which deforms plastically at comparatively low stress levels. WC-Co hard metals with high contiguity values are associated with higher mechanical strengths and more brittle behavior compared to their low contiguity counterparts [33]. Contiguity has been shown to have a significant impact on the mechanical performance of WC-Co hard metals. [76]. At *RT*, WC-Co hard metals behave as mostly brittle materials with limited ductility. It is therefore prudent to discuss the failure of WC-Co hard metals in terms of brittle fracture, which is largely controlled by the already mentioned size effect [41], as well as some failure mechanisms regarding plastic deformation [36, p. 100], [47, pp. 304–305].

Generally, whether a material fails brittle or ductile is dependent on its atomic lattice structure. Ideal lattices, by definition, are without error. Real lattices in contrast show deviations from the ideal which can be either point defects like atomic voids or dislocations. The movement of dislocations along so-called slip-planes is a possible cause for ductile deformation [25, pp. 71–87]. Those slip planes often offer multiple directions of movement; such a slip direction in a slip plane is referred to as slip system. For *FCC* crystals, as in the high-temperature phase of pure Co there are 12 such systems; for *HCP* crystals like WC grains on the other hand, there are three [25, pp. 219–229]. In polycrystalline materials like WC-Co hard metals, the constraints of grain interaction requires the activation of five independent slip systems by exceedance of the critical Peierls potential [25, pp. 265–272]. Consequently, the high-temperature *FCC* phase of Co behaves most ductile in the WC-Co system [77, pp. 91–104]. The low-temperature *HCP* phase of Co exhibits reduced ductility compared to its *FCC* phase [77, pp. 91–104] and while some plastic deformation of WC grains has been observed [38], the WC phase for the most part is brittle [6],

[78]. With the carbide phase dominating, mostly brittle fracture of WC-Co hard metals is the rule [47, pp. 303–306], [79, pp. 290–291].

On the macroscopic level and at *RT*, WC-Co hard metals exhibit mostly brittle fracture following the Griffith-model for ideal-elastic material failure [47, pp. 303–306]. Especially large workpieces and specimens are subject to the size-effect, which many defect-controlled materials exhibit [41]. As discussed previously, the probability of a critical defect existing in a loaded volume increases proportionately with the size of the respective volume [41]. Barring this, WC-Co hard metals are also used in many applications where the loaded volume is rather small; beneficial effects of such a small loaded volume have been observed by *Klünsner et al.* [40]. In this case, the microscopic behavior of WC-Co hard metals is of great interest.

In literature, four fracture modes have been observed and studied, summarized e.g. by *Spiegler and Fischmeister* [80] and in [47, pp. 303–306]. They include the transgranular fracture through the carbide crystals; the intergranular fracture along the WC-WC grain boundaries; the intergranular fracture along the WC-Co grain boundaries and the ductile fracture through the binder phase [47, pp. 303–306]. The quantity of occurrences for each fracture mode was found to be in direct relation to the contiguity of the WC-Co hard metal [47, p. 306]. These fracture modes progress in the three stages of damage initiation, subcritical crack growth and catastrophic crack propagation [42, pp. 190–204], [47, p. 306]. Since all materials show initial defects (e.g. pores, precipitations or micro-cracks), the stage of damage initiation could also be termed crack initiation at preexisting defects for WC-Co hard [42, pp. 331–332]. At *RT* and for specimens with large loaded volumes however, there is only limited subcritical crack growth [43, pp. 387–390], [47, p. 306]. *Spiegler and Fischmeister* proposed a model for predicting the crack paths on the observation-based assumption of preferential cracking in the matrix. This model sees the crack path controlled by the entry angle of the crack into the binder phase [80]. For very small loaded volumes some elastic-plastic behavior has been observed [40]. Multiple studies have shown, as summarized in [47, pp. 308–311], that crack paths favor the Co intercepts for propagation. For the most part, fracture in the binder phase is ductile and brittle in the carbide phase.

2.2.2. High temperature deformation and creep in hard metals

At sufficiently high temperatures the mechanical behavior of hard metals exhibits a pronounced change compared to that at *RT*. Notably, this includes a transition from mostly brittle behavior to brittle-ductile behavior [71], [81], [82]. In literature, three distinctive temperature regions have been defined [39], [71], [81]. At *RT* the composite deforms mostly linearly elastic and shows mainly brittle material failure. At very high temperatures, a ductile deformation explained e.g. by grain-boundary sliding can be observed [83]. A direct relation of the Co content to the impact on several mechanical properties has been shown by *Teppernegg et al.* [48]. In addition, a complex relationship of the mean grain size to plasticity has been observed: coarser grades exhibit greater plastic deformation with increasing temperature; at high temperatures however, the trend reverses and submicron grade WC-Co hard metals show greater plasticity. This was explained with the above-mentioned grain boundary sliding as main contributor to deformation above a threshold temperature [84]–[86].

In addition to this short-term behavior of WC-Co hard metals, a distinctive creep behavior has also been observed and studied [71]. Both crystalline and amorphous materials show the phenomenon of creep; that is the increase of plastic deformation when stressed at a constant level for an extended period of time [43, pp. 258–259]. WC-Co hard metals are not exempt from this effect and can fail due to creep [72]. The effect is harmful mainly due to the possible formation or growth of defects in materials subjected to long-term stresses [87, pp. 123–126].

Literature differentiates three characteristic stages to creep; primary, secondary and tertiary creep [43, pp. 259–262]. Creep behavior as described in [43, pp. 259–262] can be summarized as follows: After the initial strain, the creep rate decreases rapidly due to hardening effects caused by dislocation pile-ups until it stabilizes at a steady rate, marking the beginning of the second stage. The secondary or viscous creep can be visualized as a balance of two opposing mechanisms: the strain hardening and the relaxation through recovery processes, which dominates the third stage. While the recovery processes in stage two are mostly limited to dislocation climbs, tertiary creep sees recrystallization and overaging, depending on the microstructure. Owed to increasingly ductile behavior, creep is especially pronounced at elevated temperatures. *Smith and Wood* [88] found a more pronounced creep deformation at higher Co

contents and at higher stress levels. They proposed that at low stresses, Co self-diffusion is the main creep contributing mechanism. At higher stress levels, this changes and dislocation climb in the Co binder phase acts as the major contributing mechanism [88]. This assumption was based on findings that the energy input necessary for creep to occur was at only slightly lower levels than that for Co self-diffusion [39, pp. 409–412], [88].

Cyclic creep, or ratchetting, in contrast to creep, is observed in cyclic loading situations. It describes the accumulation of plastic strain in cyclic loading with a non-zero mean stress; it was first described by *Chaboche et al.* [89], [90]. Two types of ratchetting are distinguished; one occurring with high mean stresses for quasi-repeated loading conditions. There, the inelastic flow was ascribed to viscous or creep effects. The other type is mainly attributed to cyclic plastic flow and occurs with small mean stresses for large stress amplitudes. The ratchetting effect of this type is much smaller, [91]. Working theoretically, *Kotoul* [92] developed the model to describe the ratchetting of composites like WC-Co hard metals. Since then it has been observed in experiments for WC-Co hard metals [93].

2.2.3. Fatigue and wear of hard metals

Materials which are subjected to fluctuating stresses experience fatigue and when in contact to another body with relative motion to one another they experience wear. This also includes WC-Co hard metals. Fatigue is the reduction of the stress level a material can withstand for an extended period of time. Stresses a material can withstand under monotonously increasing loading conditions may lead to failure in a cyclic load situation. Almost all metalworking tools and even most structural assemblies experience a fluctuation or cyclic repetition of stresses [43, pp. 318–319]. As summarized in [94, pp. 346–350], the strength degradation at the endurance level of WC-Co hard metals was the subject of study in several works with the following conclusions: WC-Co hard metals show a significant reduction in bending strength, a lesser reduction of ultimate tensile strengths and a comparatively light reduction of ultimate compressive strengths in several tested WC-Co hard metal grades [94, pp. 346–350],[88].

The fatigue behavior of WC-Co hard metals was subject of study in several works [95]–[97]. Applied stress intensities and mean stress were found to have "an extremely high" [97] influence. The Co content as well as the mean grain size of the carbide were linked to the

susceptibility to strength degradation. Large grains [6] and a large mean free path of the binder phase [98], which is the average linear distance between WC grains, reduce sensitivity to stress intensities and mean stress. It has been shown *by Luyckx and Love* in [99] that the mean free path, given a fixed binder phase content, is mainly a function of the carbide grain size [28, p. 107], [99]. The binder phase was also shown to have a great influence on the fatigue behavior; in several works, *Tarrago et al*. confirmed a *crack growth resistance* (*R-curve*) behavior. The *R-curve* plots stress intensity against crack growth, thereby displaying a crack growth resistance. A short and steep *R-curve* has been confirmed for WC-Co hard metals in [100]. This behavior was explained by strongly bonded and plastically restrained Co bridges connecting crack flanks. The surface condition [101] and microstructure [93] were also reported to have a significant influence on the fatigue behavior.

Furthermore*, Kindermann et al.* documented a pronounced effect of the ambient temperature and atmosphere on fatigue behavior [102]. They described the phase transition of the binder phase Co from a more ductile *FCC* to a comparatively brittle *HCP* phase as the main influencing mechanisms on WC-Co hard metal fatigue at lower temperatures. With increasing temperature, they ascribed dominance to the oxidation of Co at subcritical cracks in the ductile binder phase and subsequent embrittlement [102].

However, these are not the only mechanisms by which WC-Co hard metals can accrue damage over time; in most cases, there is also wear. Wear is tribology's subject of study, which itself is "the science of interacting surfaces in relative motion" [103, Ch. E]. There are many wear-inducing mechanisms, albeit mainly abrasion, erosion and sliding wear and a combination thereof are of significance for WC-Co hard metals [49, Ch. 364–367]. Abrasion is the scoring and chipping of material by another body's roughness peaks or spalled particles on a microscopic scale [103, Ch. E]. The conditions in which abrasion occurs were found to influence the magnitude of wear [49, pp. 364–367]. Especially the hardness and particle size of the abrasive material are reported to have great influence [104]. The volume of abrasion wear shows a strong and inverse relation to the hardness of the worn WC-Co hard metals [105]. The main mechanism of abrasion in WC-Co hard metals was found to be the removal of the exposed binder phase with subsequent spalling of WC grains [104], [105]. Given these facts, *Gee et al.* in [49, pp. 364–367] developed a mathematical model to describe the influence of microstructure on the volume of wear by

abrasion but could not fully determine the influence and value of their microstructural parameters on abrasion [49, pp. 364–367].

Sliding wear, albeit described as somewhat similar to abrasion was observed as being less dependent on the microstructure [49, pp. 364–367]. In contrast, a significant effect of the surface condition [106], the load [107] and even the pH of lubricants [108] has been found.

Erosion is the mechanical degradation of material by flowing media [109, pp. 351–352]. Literature distinguishes cavitation and wear erosion [49, pp. 367–369], [109, pp. 351–352]. The former sees material erosion due to the collapse of cavities in the fluid close to the material surface and subsequent significant stresses on the surface caused by the suction [109, pp. 351–352]. The latter is characterized by the presence of hard particles in a liquid or gaseous medium [49, pp. 367–369]. Several effects regarding erosion have been studied [49, pp. 367–369]. These effects can be summarized as a large dependence of scale as to whether brittle or ductile material response dominates erosion, studied in detail by *Anand and Conrad* [110]–[112].

2.3. Applications of WC-Co hard metals

WC-Co hard metals are known for their superior mechanical properties and relative insusceptibility towards high temperatures [48]. This makes them uniquely suited for applications in extreme conditions. *Konyashin* [53, pp. 425–451] categorized the main application fields into use as drilling bits, cutting edges and wear parts [53, pp. 425–451]. They are also used as rolls for hot rolling and as tools in cold forming [19, pp. 29–32]. *Klocke and Koenig* explained comprehensively in [18, pp. 119–137] the use of WC-Co hard metals as tools for the milling, drilling and cutting of a wide variety of materials, from rock processing to machining of high-performance alloys [18, pp. 127–129].

2.3.1. WC-Co hard metals in machining tools

In machining there are many variations which *Klocke and Koenig* summarized in [18, pp. 41–99] into three main approaches: The free orthogonal cut, the free inclined cut and the bound inclined cut. Described as default is the bound inclined cut, which allows for the main and side cutting edge to be employed at arbitrary angles for continuous as well as discontinuous cuts. An

apt sketch of the mentioned situations provided by *Klocke and Koenig* in [18, p. 49] is shown in *Figure 4*.
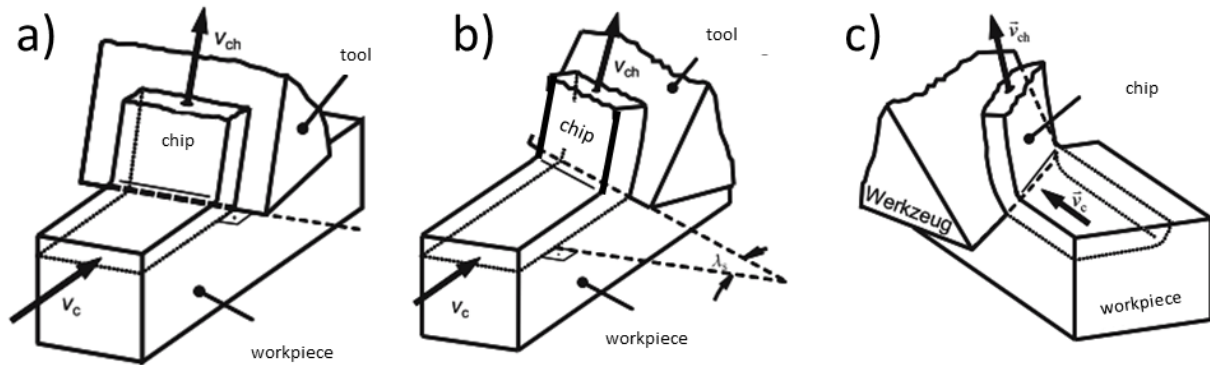
Figure 4: Visual representation of the cutting techniques outlined in [18, p. 49]. From (a-c): (a) The free orthogonal cut. (b) The free inclined cut. (c) The bound inclined cut.

The machined material usually produces chips [18, pp. 50–53]. The chipping behavior can be influenced by direction and amount of load put on the material [113]. During the chip formation, rather extreme conditions may occur; temperatures ranging from 770 to 1,700 °C as well as significant stresses are present, putting a considerate load on the tool flank [18, pp. 50–53], [114]. Naturally the chipping behavior also depends on whether or not a cut is continuous. For discontinuous cuts e.g. the heating and loading of the tool is cyclic, changing in dependence of the cycle count number, which is defined e.g. by *Nemetz et al*. as a cutting and subsequent idle period [13], [114], [115]. Chipping aside, there are many influences in machined material and machining tool alike which control the life-time of a tool.

2.3.2. Alloying concepts

To accommodate the various requirements for different purposes, WC-Co hard metals must fulfill a multiplicity of demands. Some, like toughness and hardness, are in contradiction. Since their invention, the easiest way to control the specific mechanical properties has remained with the Co content and the carbide grain size [18, pp. 127–129], [19, pp. 29–32]. Industrially used hard metal grades mainly utilize WC-Co hard metals with Co contents ranging from 4 to ~30 wt. % Co. Regarding grain sizes, industry commonly distinguishes coarse, medium, fine, submicron and ultrafine grades. The finer the grains, the greater hardness and strength, but at the cost of toughness (with exceptions) [18, pp. 127–129], [19, pp. 29–32].

For the machining of metals and their alloys, the addition of cubic transition carbides proved more than beneficial. They form a solid solution with WC which enhances the creep and oxidation resistance and also improves the wear rates [19, p. 37].

2.3.3. The coating of tools

Since the late 1960's, the coating of WC-Co hard metal products gained steadily in popularity. The significant improvement of tool lifetimes because of the added wear and oxidation protection of such coatings provided an incentive for focused research [18, pp. 137–138], [116, pp. 453–455], [117]. From the beginning, the use of particularly hard substances like TiN, TiC and aluminum oxide (Al_2O_3) was favored; after the invention of multilayer coatings often in combination [116, pp. 453–455]. In recent years, a multilayer coating composition of a titanium diboride (TiB_2) coating with a TiN interlayer has been the focus of several works [118]–[122].

Most hard coatings are produced by condensing the substance from the vapor phase, with two distinguished methods. With *physical vapor deposition* (*PVD*) the respective vapor is generated from a solid source and applied to the surface via ionization methods. Using *chemical vapor deposition* (*CVD*) requires higher temperatures, because the coating forms with chemical reaction in the gas or vapor phase [123, pp. 19–21]. Especially *CVD* is well suited for complex geometries and wide ranges of coating thicknesses [116, pp. 453–455], [124, pp. 507–511]. Which technique is used depends on the workpiece geometry and the type of coating. Oxide or nitride coatings are usually applied with *CVD* while metallic coatings are typically produced with *PVD* [116, pp. 453–455]. Many *CVD* coatings show tensile residual stresses and superficial crack networks due to greater thermal retraction of the coating compared to the substrate [125].

TiN-TiB_2 multilayer coatings usually are produced using *CVD* [120], [121]. Works performed on this subject showed that in contrast to most *CVD* coatings this particular multilayer exhibits high residual stresses in the compressive spectrum [120], [121]. Those were found to rise with the boron (B) content and layer thickness [121]. Their origins were investigated by *Schalk et al.* [121] and explained with the nano-crystalline structure of the TiB_2 phase, which is considered the result of strong covalent B-B bonds and segregational tendencies of B atoms [121]. To improve adhesion, an interlayer for TiB_2 coatings was recommended e.g. by *Kullmer et al.* [120].

3. The ball-in-cone test

The testing of materials is always a challenge in that it must not only be replicable but also well-understood. Producing results must also always be accompanied with a thorough understanding of how those results came to be. By subjecting a material to extreme situations – be they of mechanical, thermal or corrosive nature – a better understanding of the respective materials behavior is desired. Of particular interest are methods which affect the material in ways similar to what it has to cope with in its applications.

3.1.   Testing of WC-Co hard metals

Compared to most materials, WC-Co hard metals are particularly hard to reliably test. Despite their mechanical strengths and resiliencies, they are brittle and fail in accordance with Weibull distributions [41], [126]. They are often used in complex, multi-axial loading situations with high compressive and tensile loads, at temperatures often approximating 1,000 °C in cyclic loading conditions with or without pronounced impacts [13], [18], [114], [115], [127], [128].

Especially in recent years, the interest in the load situation a machining tool has to endure during use has manifested in a multitude of works by various authors regarding various applications [13], [73], [114], [115], [127], [129], [130]. The underlying desire was, and is, to understand the loads influencing the material and how they might lead to failure. Better understanding then can lead to bespoke measures regarding tool material or design, improving life expectancy and performance of tools.

Klocke in [18] differentiates three modes of machining (see *Figure 4*): The free orthogonal cut, the free inclined cut and the bound inclined cut. They can be executed continuously or discontinuously [18, pp. 48–49]. In addition to these parameters, the load situation is, among others, also influenced by the absolute amount of the machining force as well as the cutting velocity and feed velocity [18, pp. 58–72]. Furthermore, the mode of chipping, whether segmented or continuous chips are formed, and the state of wear of the tool were found to have an effect [128, pp. 113–124].

Given the number of influencing factors, a definitive answer is not possible. However, the loads a tool is subjected to, split into normal and tangential forces and as a result the tool suffers

compressive normal stresses and shear stresses at both the rake face and the cutting edge [128, pp. 117–120]. These stresses trigger damaging mechanisms which can lead to a subsequent failure of the tool. This is true particularly for tools used with materials difficult to machine, since the temperature is often limited only by the melting temperature of the machined material. There is also a necessity to avoid alteration of the workpiece's material properties by the induced high temperatures [128, pp. 121–124].

Several works found temperatures ranging from 650 °C to above 1,050 °C in the chip-tool contact area during cutting [13], [114], [127], [131]. *Klocke et al.* also described a "specific tool load" [127] calculated from the material-tool contact area and the cutting force [127]. Used as a qualitative indicator for the peak load in the material-tool contact area, the presented values were significantly above 1,000 MPa for the cutting of a Ti-Al6-V4 alloy [127]. In milling tools *Nemetz et al*. [115] found temperatures of 650 °C, with only a small volume seeing temperatures above that value [115]. In [13] *Nemetz et al.* reported stresses in milling inserts of similar value to what *Klocke et al.* found for cutting inserts [127]. Both compressive and tensile stresses were seen; also a clear development towards higher tensile stresses with progressing load cycles was observed [13].

The load situation in machining tools is complex. Yet understanding it is indispensable, especially for WC-Co hard metals. Because of the manifold and hard to separate influences, the use of a finished tools as specimen is common, as e.g. in [15]. The obvious advantage here is that the test performed is almost indistinguishable from reality; however, only the result of the whole compound of influencing factors can be observed. For better control over several of these influencing factors, a test setup to replicate the load situation at the cutting edge of milling tools at elevated temperatures was developed. This test setup shall be described in the following.

3.2. Replication of observed normal and tangential loads

Recently, the relation of normal to tangential loads in tool substrates was studied. It was shown that at the rake face in contact with the chip, the normal loads were mostly four times as large as the tangential forces, displaying a ratio of $^4/_1$. At the cutting edge of milling tools, the dominance of normal loads was even more pronounced [132]. Following these considerations, several test concepts were developed and analyzed for viability in [133].

3.2.1. The concept design

In several works an inclined surface has been used to achieve a multi-axial load situation. To the best knowledge of this author, the investigations performed foremost featured an impact test on an inclined surface introduced by *Bouzakis et al.* in [134]. This test is featured in several works studying the adhesion as well as the fatigue and wear behavior of coatings and coating-substrate interfaces [134]–[139]. While the focus of the current work lies not on the study of coating adhesion, the use of an inclined surface to achieve normal and tangential loads is rightfully attributed to these authors. On the following pages a novel material testing setup designed to emulate the loading conditions on the cutting edge of milling inserts will be explained in detail. The construction drawings used for manufacture are also included in the current work (see Appendix A).

The components were designed for radial-symmetric load application and high modularity. The central design choices, however, are integral to this concept. An inverted cone at the top end of the sample is in contact with a rounded body (referred to as "indenter"). Hence the designation, "ball-in-cone". The flank inclination of the inverted cone and the radius of the indenter can be varied to achieve different load situations. For the current work however, a fixed geometry was used. On the following pages the geometric specifications used for this setup will be laid out in detail.[1]

Any test setup needs a mechanism by which load is introduced to the tested material. For the ball-in-cone test, this falls to the so-termed indenter, illustrated in *Figure 5*. The indenter is a cylindrical rod 125 mm long and 20 mm in diameter. On one end it is spherical, displaying a curvature with a 15 mm radius. The rounded end is in contact with the specimen surface, applying the load to the tested material.

---

[1] The materials used for the samples can be found in Chapter 4.1.1.1. *Sample materials* and the materials used for indenter and sample holder are described in Chapter 4.1.1.2. *Indenter and sample holder material*.

Figure 5: Sketch of the load-transferring indenter; the full length of this component is 125 mm with a diameter of 20 mm and a curvature at the tip of a 15 mm radius.

In the following, *Figure 6* shows the design of the samples used in this novel test; the samples are made of the material to be investigated. The design is based on both an improvement on the findings of [133] and the desire to keep the specimen as modular as possible.
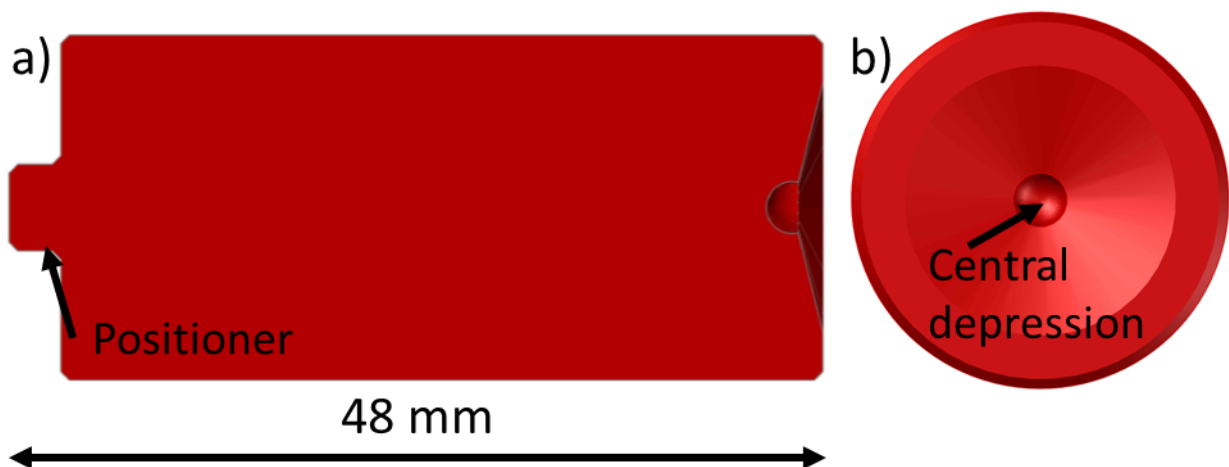
Figure 6: Schematic of the sample component. (a) The full-length sample measuring 48 mm total also with a diameter of 20 mm. (b) In the top-down view the inverted cone and the central depression are discernible.

As can be seen in *Figure 6 (b)* the sample is cylindrical. It features an inverted cone converging on a central depression. Its flank inclination is set at 14° to achieve the previously mentioned relation of normal and tangential loads [132], [133]. The full diameter of the sample is 20 mm and the diameter of the central depression is 3 mm. The length of the main body is 45 mm with a 3 mm long positioner with a 5 mm diameter at the bottom end. The positioner's main function is to fixate the samples position with the later described sample holder during assembly of the whole test setup.
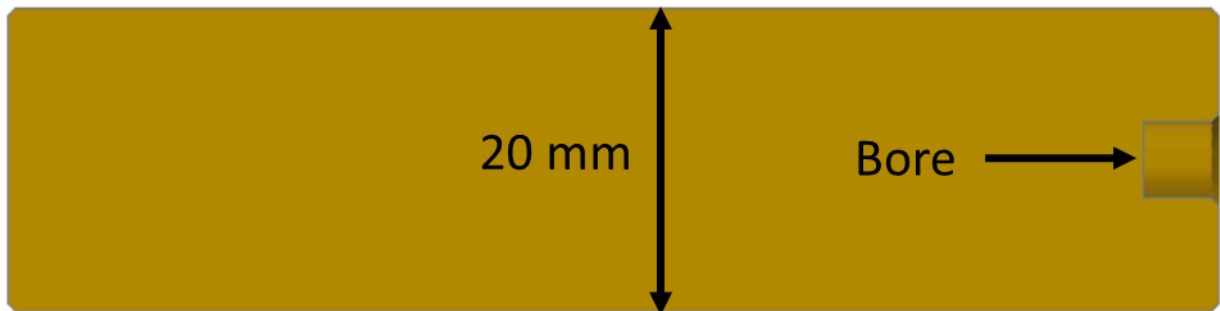
Figure 7: The sample holder with a length of 80 mm and a diameter of 20 mm is used to support and fixate the sample during installation and testing. Assembled, the 5 mm deep bore accommodates the sample's positioner.

This sample holder, shown in *Figure 7*, is necessary for two reasons: It enables a significantly reduced sample size, minimizing material waste. It also keeps the setup as modular as possible. Its length was set at 80 mm and its diameter at 20 mm. At one end a radially central bore with a diameter and a depth of 5 mm was drilled to accommodate the sample's positioner
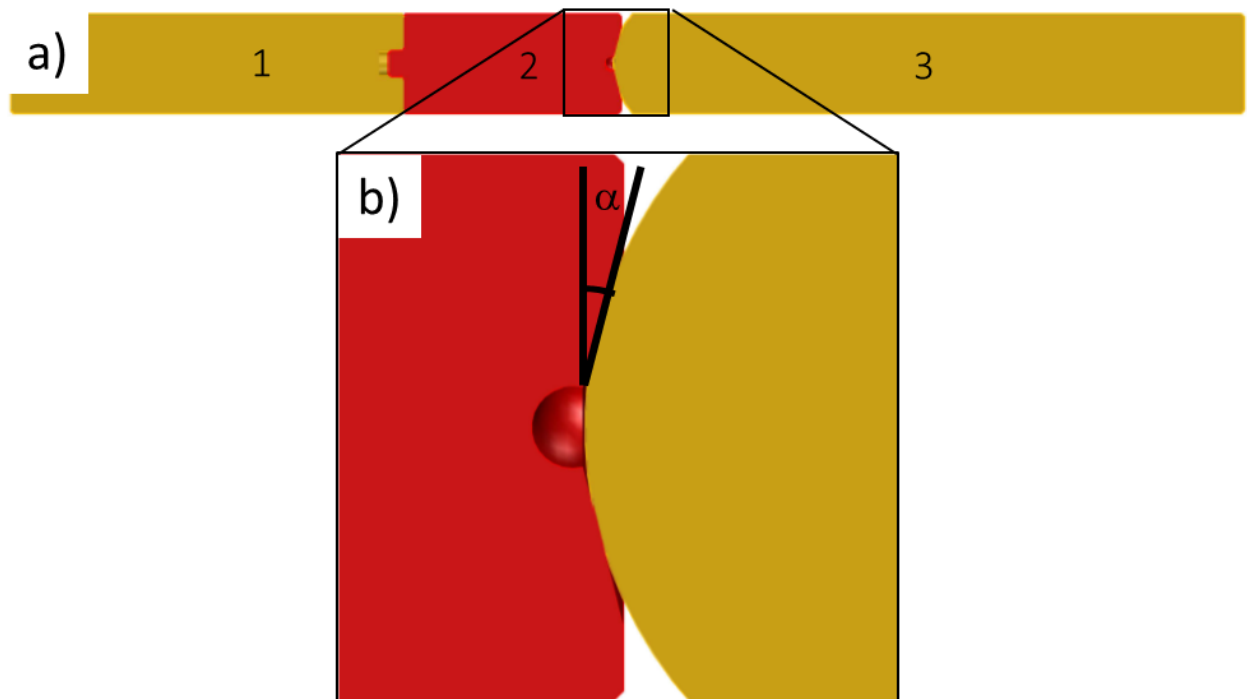
Figure 8: The assembled test setup in cross-sectional view with specimen-indenter contact established. (a) The assembled components sample-holder (1), sample (2) and indenter (3). (b)The specimen-indenter shown in contact with the sample's flank inclination of 14°marked (α).

The setup is fixated in the testing apparatus at three points: Clamps secure the sample holder and the indenter at their respective bottom ends with the sample secured via its positioner, inserted in the corresponding sample holder's bore. *Figure 8* sketches the full setup with every component in place. As implicated by the design, an uniaxial compressive load is introduced along the central rotational axis of the setup and split up into its normal and tangential components by the sample's inverted cone's flank inclination.

3.2.2. The first load cycle – a simulation

As mentioned above, previous work regarding the influence of a spherical indenter on an inclined surface does exist. The focus in these works primarily lay on the influence of high-load impacts on the coating-substrate interfaces strength properties of studied samples [134]–[139]. To the best of this author's knowledge, no work on the influence of a rounded indenter on the damage behavior of a substrate below an inclined coated surface has been done. The load situation of the *BIC* test is not trivial. A simulation based on the *finite element* (*FE*) approach was conducted[2] to better understand the load situation and guide the *BIC* test regarding specific *regions of interest* (*ROIs*) on the sample.

The commercial *FE* package ABAQUS 2018 [140] and the element type CAX4 was used. The element size ranged from 1 µm in the contact area between sample and indenter to 5 mm in regions more distant from this site. The above presented geometric dimensions were adhered to, with a 3.5 µm thick TiN-TiB$_2$ coating on the sample surface. For the coating, a purely elastic material behavior was used. The Young's moduli were taken from [120] and are shown in *Table 1.* In reality, the Young's modulus for such a multilayer coating shows a gradient. For this model a homogenous value of 475 GPa was assumed [16]. The friction behavior of a TiB$_2$-coating manufactured via plasma-spraying was studied in a ball-on-disc test using a WC-Co hard metal ball with a 5 mm diameter as counterpart at *RT* in ambient atmosphere [141]. Under 50 N contact load, the measured friction coefficient showed an initial value of 0.1 that changed during testing to 0.5. For the specimen-indenter contact of the *FE* model in the current work, a friction coefficient of 0.2 was assumed. The material parameters used for specimen and indenter

---

[2] The model, calculations and their results here presented are work performed and provided by M. Krobath (affiliated with the Materials Center Leoben Forschung GmbH) in the scope of this thesis [16].

substrate are also shown in *Table 1*. The properties of materials at elevated temperatures were based on values in [48]. The testing temperature was set at 700 °C and material parameters at this temperature were assumed for the model. Testing conditions were isothermal, therefore the simulation assumed a constant temperature of 700 °C. In [48], the Young's modulus was found to be mainly dependent on the Co content. The values provided for a WC-6 wt.% Co hard metal with a mean grain size of 2 μm were also used for the indenter material, despite the difference in mean grain size [48]. Cyclic deformation behavior of specimen substrate and indenter material was determined using the technique described in [72].

Table 1: Material parameters used as input for the FE model. For the substrate materials, values at 700 °C were used. For the coating materials, values obtained at RT were used.

Component	Material	Co content [wt. %]	Mean grain size [μm]	Young's modulus [GPa]	Poisson ratio [-]
Specimen: Substrate	WC-12 wt.% Co	12	2	495	0.21
Specimen coating: Top layer	TiB_2	-	-	525	-
Specimen coating: Interlayer	TiN	-	-	325	-
Indenter	WC-6 wt.% Co	6	0.7	590	0.22

To describe the elastic-plastic material behavior of sample and indenter, an isotropic elastic-plastic behavior model with kinematic hardening was used; a form of a Chaboche-type model based on work by *Chaboche et al.* [16]; similarly used e.g. in [8]. In addition, creep was considered using the "Strain-Hardening" model provided by the ABAQUS software. While creep was seen as accurately described with this model, the ratchetting behavior of both sample and indenter material was considered as somewhat overestimated [16].

One of the initial uses of the model was to decide upon the uniaxial load necessary for achieving the targeted stresses in the sample. Compressive stresses of - 2,000 MPa can be expected [127]. For modelled mechanical behavior, the use of principal stresses is prevalent. A principal stress features non-zero values only in the σ_{11}, σ_{22} and σ_{33} tensor positions; i.e. a stress

situation in which stresses occur only along the three spatial axes. With this approach, the otherwise complex stress situation is considerably simplified [103, Ch. C]. Based on findings regarding the stress situation of milling inserts, the target minimum principal stress was set at - 1,800 MPa [142]. The required uniaxial load was derived by loading the model with increasing loads until the calculations showed the desired stress value. The subsequently utilized loading curve as well as the thereby induced stresses are displayed in *Figure 9*.
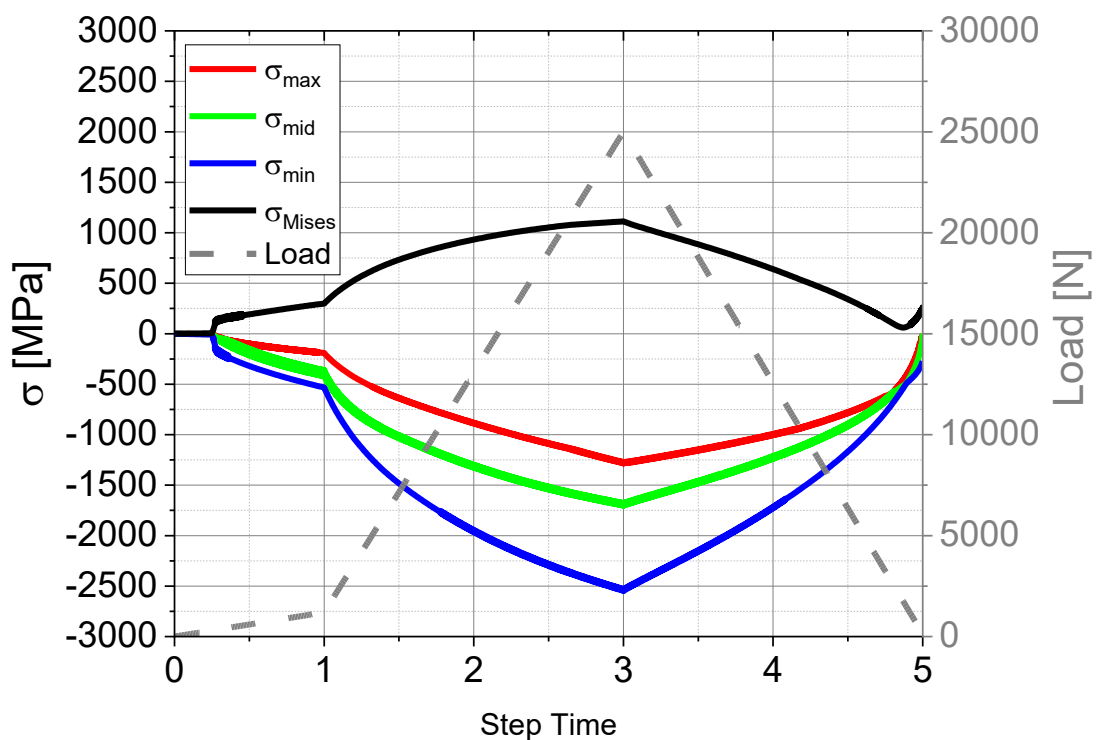
Figure 9: Precise control over the introduced minimum, medium and maximum principal stresses in the first load cycle via correlation with the load is enabled by the simulation. The shown stresses are at the position of the minimum principal stresses in the substrate. For every applied load (right ordinate) there are corresponding stresses (left ordinate). The abscissa displays the dimensionless, linear time parameter, with 0 set as the starting point and 5 as the end point of a loading-unloading cycle with a maximum load of 25,000 N. Within the first time step (0 – 1) a minimum contact load of -1,200 N is established. The irregular stress behavior within the first and the last time step is due to calculation artifacts.

As shown in *Figure 9,* the stress situation shows the target minimum principal stress as well as the medium and maximum principal stress. Using *Figure 9*, the required load for any desired maximum compressive stress up to -2,500 MPa can be inferred. To enable an observation of the damage behavior of both sample and indenter material, a further calculation for up to 10,000 load cycles was conducted. For these calculations, a maximum compressive load of -12,000 N with a resulting maximum compressive stress of -1,800 MPa in the substrate material was chosen.

3.2.3. From 1 to 10,000 load cycles

For the development of cyclic plastic deformation, ratchetting was assumed as increasing in linear fashion. In reality, this is not the case. This simplifying assumption leads to the expectation of overestimated plastic deformation with this model. Nevertheless, contact width and remaining indentation depth on the sample were calculated for several load cycle numbers. The contact width was determined on the indenter model by evaluating the distance between the innermost and outermost point of contact between sample and indenter. During the first load cycle, a contact area width of ~130 µm at a load of -1,200 N was measured. At the maximum compressive load of -12,000 N that width was ~400 µm. After 1,000 load cycles the width had increased to ~470 µm at minimum and to ~650 µm at maximum compressive load respectively. After 10,000 load cycles, the values at minimum and maximum compressive load were 489 µm and 687 µm respectively. A remaining indentation of 3 µm maximum depth was also measured for this load cycle number. The depth was calculated by comparing the distance between the surface at the point of maximum plastic deformation after 10,000 load cycles and in the initial state.

In *Figure 10,* described in the following*,* the development of the *difference of the maximum and minimum stress-values in one load cycle* ($\Delta\sigma_{max}$) and the *stress ratio* (*R*) over 10,000 load cycles is displayed*.* The left-sided ordinate plots the $\Delta\sigma_{max}$ which is the greatest possible difference between the maximum and minimum principal stress for the course of the denoted load cycle [16]. The right-sided ordinate plots the stress ratio (*R*), which is the quotient of the minimum and maximum principal stress, indicating the cyclic mean stress at the respective position. As is convention, *R* approaching negative infinity means purely compressive stresses,

while convergence to zero describes a significant tensile stress component [16], [43, Ch. 319–321]. The path on the abscissa is located in the sample's substrate about 4 elements of the FE model body below the substrate-coating interface. This represents a distance of approximately 4 μm to this interface. Distinguishing the development of these stress modes is especially important since a change in loading mode has been documented to have a notable influence on the fatigue behavior of WC-Co hard metals [5]. Understanding the *BIC* test's load situation over a wide range of load cycles enables studying such effects in coated substrates.

Of particular interest in *Figure 10* is the area from 3.25 mm to 4 mm, which is the main contact area. In this area three positions were chosen for microstructure documentation: The *central position* (*P1*), and the *outer-fringe* (*P2*) and *inner-fringe* (*P3*) *positions*. The definition outlined in the following is also valid for the following chapters in the current work. In the first hundred load cycles, the peak $\Delta\sigma_{max}$ is reduced from 1,800 MPa to 1,500 MPa. From 1,000 load cycles onwards $\Delta\sigma_{max}$ at *P1* is further reduced. *P2-3* see increasing stresses. At *P1*, *R* constantly shows convergence toward -∞. At *P2*, *R* is close to 0 and at *P3* below -4. In *Figure 10*, *P1-3* are marked. The central position is set at 3.625 ±0.05 mm from the path starting point. That starting point is set at the test setup's central axis. The outer-fringe position was placed at 3.875 ±0.05 mm, the inner-fringe position at 3.375 ±0.05 mm. According to *Figure 10,* the central position sees mainly compressive stresses, while an alternation between tensile and compressive stresses occurs at the other positions.
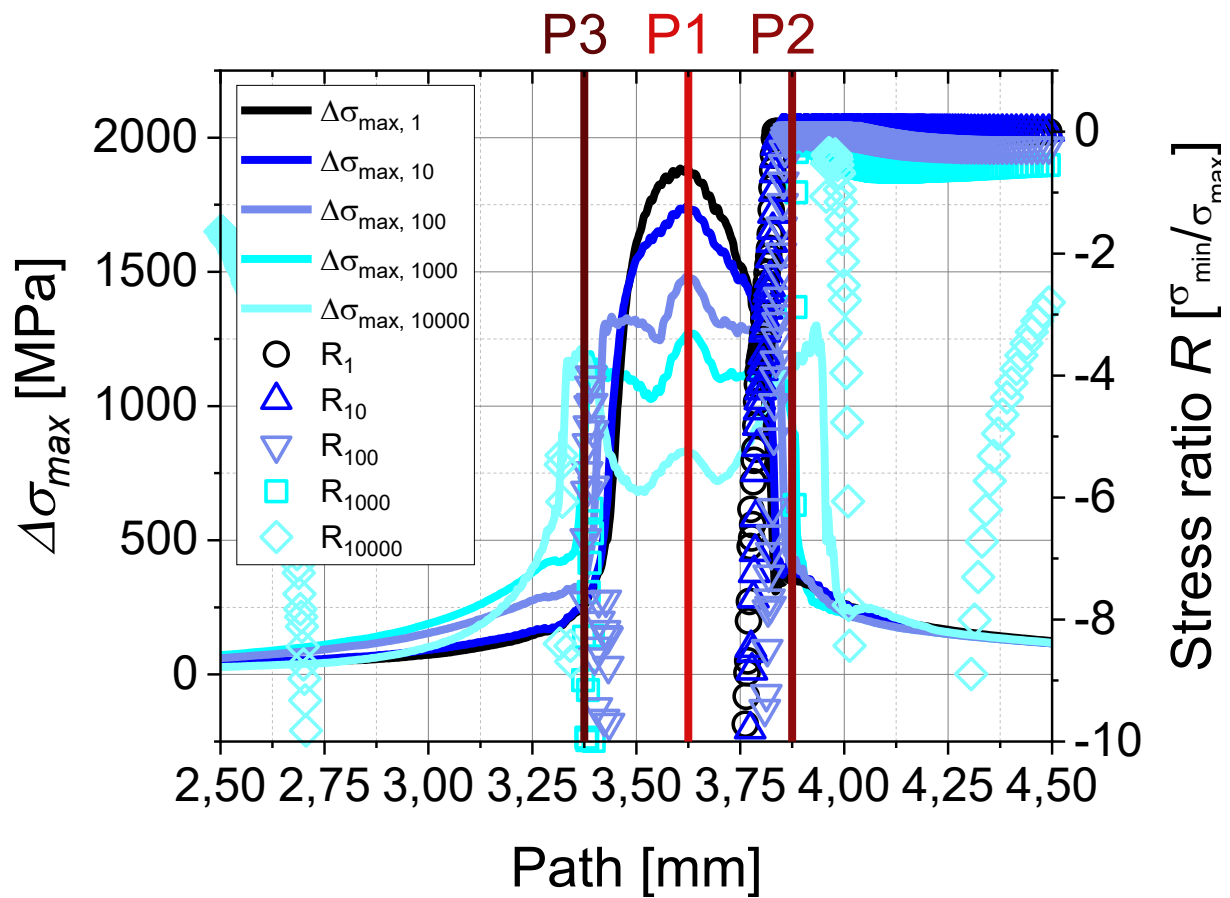
Figure 10: Development of Δσ$_{max}$ and the cyclic stress ratio R from 1 to 10,000 load cycles over the path. This path is set parallel to the cone flank 4 elements, about 4 µm, below the coating-substrate interface. The starting point is at the specimen's central axis. The end point is at the outer edge of the sample's inverted cone. At the central position (P1) the stress ratio R approaches -∞ and Δσ$_{max}$ is initially high. At the outer-fringe position (P2) the stress ratio is close to 0 and Δσ$_{max}$ is lower than at P1. At the inner-fringe position (P3) the stress ratio is below -4 and Δσ$_{max}$ similar to that at P2.

3.3.   Practical utilization of the ball-in-cone test

The greatest advantage of the *BIC* test's concept design proved to be the highly modular samples. Their design was rotationally symmetric and so are the introduced stresses. The sample could be loaded to a desired load cycle number and the microstructure investigated via a cut placed via *focused ion beam* (*FIB*) milling. This did not destroy the entire sample; it was loaded to another, higher desired load cycle number and its microstructure studied at a different azimuthal

29

position using another *FIB* cut. Keeping a sufficient distance from the prior positions was necessary because superficial defects can distort the surrounding stress situation over distances several times their diameter. This is the reason why a sufficient distance between e.g. Vickers hardness measurements on the same specimen is required [43, pp. 121–123]. The dimensions of the *FIB* cuts were approximately 30x30x30 µm³. Following the prior considerations, the minimum distance was set at 300 µm. An angular difference of the azimuthal angle ranging between 45° and 60° was deemed sufficient. Note that *Figure 11 (1) and (2)* mark an investigation each.
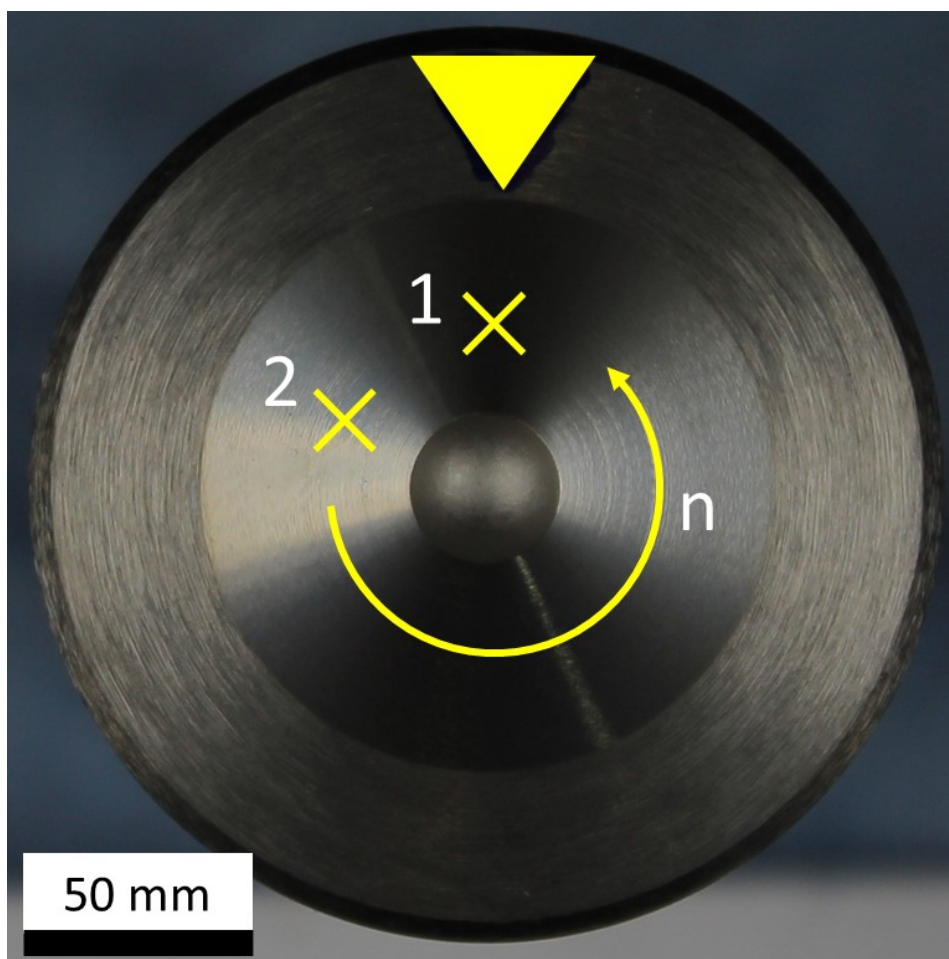
Figure 11: Visualization of repeated specimen use with the BIC test. The specimen was tested once and investigated with FIB-cuts. The azimuthal position was marked on the specimen (yellow triangle) and the FIB-cut placed at (1). Large parts of the specimen surface area remain unused. The specimen is tested again and investigated using another set of FIB-cuts at (2). The process was repeated up to 4 times (n). Cumulative microstructural damage in one specimen was documented.

4. Experimental application of the ball-in-cone test

The damage initiation in hard-coated WC-Co hard metal specimen under multi-axial loads at elevated temperatures in a vacuum environment was studied. For this, the novel ball-in-cone test was used. Because of the novelty of the setup, its usability and degradation were also observed.

4.1. Experimental details

4.1.1. Investigated material

For indenter, sample holder and specimen, two WC-Co hard metal grades were used. The specimens were coated. Further details are as follows.

4.1.1.1. Sample materials

A WC-12 wt. % Co hard metal was chosen as sample material. The mean grain size was 2 μm. The specimens were manufactured following the traditional powder-metallurgical route with the inverted cone ground into the green body followed by subsequent sintering. A TiN-TiB$_2$ multilayer coating was deposited in a method similar to those described in literature [121], [122]. As a result, the coating surface was devoid of cracks, but featured significant residual compressive stresses [121]. It was assumed that coating failure was unlikely. In total, six samples were produced by Ceratizit Austria GmbH in one and the same production batch. This was to ensure greatest possible homogeneity in defect density and distribution in the investigated samples [143]. For the investigations performed in the current work, four of those samples were randomly chosen.

4.1.1.2. Indenter and sample holder material

Indenter and sample holder were manufactured similarly to the sample. The material was a submicron-grade WC-6 wt. %Co with a mean grain size of 0.7 μm. Both components were left uncoated. Two of each component were provided by Ceratizit Austria GmbH; of the available pieces one was randomly selected for the *BIC* test and the duplicates kept in case of unexpected material degradation in the used parts.

4.1.2. Load application

For load application, the servo-hydraulic testing apparatus Instron 8803 was used; described in more detail by *Maier et al.* in [72]. Uniaxial load was introduced by the machine and split into normal and tangential loads by the *BIC* geometry.

4.1.2.1.   Ambient temperature and atmosphere

A testing temperature of 700 °C was targeted. The *BIC* test was set for isothermal conditions; i.e. the temperature unchanging during loading. Thermal stability was ensured by using two spot-welded thermocouples. One was used for temperature regulation, the other for control measurements, both positioned as shown in *Figure 12 (a-b). T*he *BIC* test setup has to endure elevated temperatures for the duration of the heating, testing and cooling period. Prior to testing, the temperature is held for 15 minutes to achieve thermal equilibrium. The procedure takes well over an hour. The *BIC* setup – uncoated indenter and sample holder especially – was therefore deemed at significant risk of oxidation. To avoid this, the servo-hydraulic testing apparatus was fitted with an auxiliary vacuum chamber. Tests were performed at a base pressure of $5*10^{-6}$ mbar. The installed setup is shown in *Figure 12 (b).*
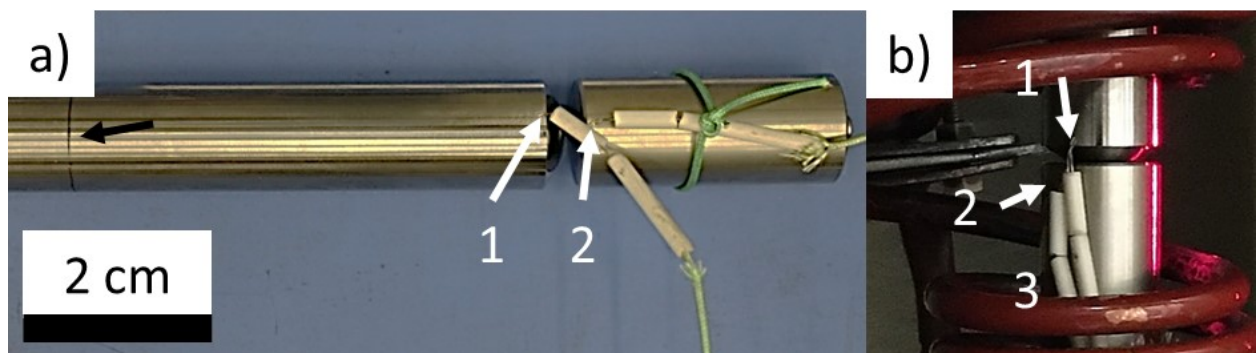
Figure 12: Photographic documentation of sample and indenter prior to and after installation. (a) Thermocouples are spot welded prior to installation on the indenter (1) and the specimen (2). The marking indicated by the black arrow gives the position of the fixation clamps. (b) In full assembly the thermocouples are still visible. The setup is installed in the vacuum chamber within the induction coil (3) used for eddy current heating.

4.1.2.2.   Target load

A target stress was chosen based on previous work on stresses seen by machining tools [18, pp. 58–72], [127], [128, pp. 113–124], [142]. The aim of the *BIC* test was to introduce these target stresses in the specimen substrate. The testing machine, however, was operated via a load cell. This was solved as discussed previously, with the targeted minimum stress of -1,800 MPa corresponding to -12,000 N uniaxial load; see *Figure 9* for further details. Most machining operations performed see segmented chipping [18, pp. 41–99], regardless of whether the cut is continuous or discontinuous. This usually results in load fluctuations (Klocke and König, 2008, pp. 41–99. An impact test was considered unfitting, because it would have introduced a more complex, less controllable stress situation, while at the same time reducing setup stability. Considering this, a cyclic loading condition with a maximum compressive load of -12,000 N and a minimum compressive load of -1,200 N with a frequency of 2 Hz was chosen. Prior to the first full load, the sample was fixated during installation and heating with ~5% of the maximum load at approximately -500 N. Since this meant a compressive stress of ~-90 MPa, resulting mechanical and creep effects were assumed as negligible [16].

4.1.2.3.   Investigated load cycles

Previously, the possibility of multiple specimen uses has been explained[3]. This was fully utilized in the here presented investigations. *Table 2* shows the progressive load cycle numbers at which the specimen microstructures were documented using FIB-cuts. The specimens were designated as Dβ01-4.

---

[3] Outlined in Chapter 3.3. *Practical utilization of the ball-in-cone test*.

Table 2: Overview of the target load cycle numbers at which the specimen microstructure was investigated using FIB-cuts, placed according the previous definition of ROIs[4].

Target load cycle numbers		0	10	85	850	1,700	2,500	3,400	5,000	10,000
Sample	Dβ01	-	P1-2	P1-2	P1-3	-	-	-	-	-
	Dβ02	-	-	-	-	-	P1-2	P1-2	P1-3	P1-3
	Dβ03	-	-	-	P1-3	P1-2	P1-3	-	-	-
	Dβ04	P1-2	P1-2	-	-	-	-	-	-	-

4.1.3. Sample documentation

To observe the damage evolution of both specimen and indenter, several methods of documentation were employed. Visual inspection of the samples was used to determine large-scale changes to the specimen surface area. Discolorations and macroscopically visual aberrations from the initial state of indenter or specimen were detected and subsequently documented using photography. Exposure of the microstructure was enabled by utilization of a Dual-Beam *FIB-*capable *SEM* (a Zeiss AURIGA-CrossBeam work station). Prior to the *FIB* milling, the sample was prepared by deposition of a thin layer of platinum with a thickness < 1 μm. The pit was cut with a Ga+ ion beam, stimulated with an excitation voltage of 30 kV. For microscopic documentation a Zeiss EVO MA 25 work station was used. *Secondary electron* (*SE*) and *electron back-scattered* (*EBS*) contrast modes were used for visualization of the specimen microstructure. Excitation voltage varied from 2 kV to 10 kV with a working distance of 5 mm to 8 mm. As for the indenter: apart from macroscopic documentation via standard photography, *SEM* micrographs were used to visualize the superficial material degradation of the indenter. For these investigations, *SE* contrast with an excitation voltage of 15 kV at a working distance of 11 mm was employed.

---

[4] As defined in Chapter 3.2.3. *Load cycles from 1 to 10,000 load cycles.*

4.2.   Performed investigations

4.2.1. Investigations regarding the viability of the BIC test

The *BIC* test is a novel testing method with a complex load situation. Several investigations regarding the viability of its results were performed as follows.

4.2.1.1.   *Installation and temperature calibration*

Any novel test method must, after successful conception, pass the test of practical application. This was also the case for the *BIC* test. Consequently, the installation process was well-documented. Even more crucially, so was the temperature calibration procedure. A temperature rise was induced via an induction coil in a setup consisting of three distinctive components differing in volume. One of these components also featured a coating layer. While the thermal properties for indenter, sample holder, sample and coating material were of similar magnitude, temperature gradients of some kind were expected and studied. The main investigative tool hereby was positional variation of the sample with its indenter and holder with respect to the induction coil. Temperature control was provided via the aforementioned thermocouples[5]. Since the specimen used for calibration designated as *Dβ01* was also used in subsequent testing, two investigations at 10 and 850 load cycles were replicated with other specimen to determine the influence of creep on the observed magnitude of damage.

4.2.1.2.   *Test setup degradation*

One major unknown quantity of the *BIC* test was the rate of material degradation in the indenter. The initial state was only documented via standard photography. Subsequent surface documentation was performed via *SEM* after 3,360 load cycles and after 15,110 load cycles.

---

[5] For more details, see Chapter 4.1.2. *Ambient temperature and atmosphere*.

4.2.2. Investigations regarding damage introduced by the ball-in-cone test

Concurrent with the aforementioned investigations were those studying the damage occurring in the specimen substrate due to stresses introduced by the *BIC* test.

4.2.2.1. *Sample documentation and defect frequency*

As described in the previous section, the specimens' relevant surfaces as well as their microstructure were investigated. The latter was exposed using a *FIB* with subsequent visualization via *SEM* micrographs. The surface documentation was inspected regarding artifacts stemming from manufacture (e.g. grinding grooves, coating flaws) and therefore with a particular focus on deviations from an ideal surface.

Regarding the microstructure, defect size and frequency were investigated in consideration to their possible origin; i.e. whether they were introduced during manufacture or testing. Every detectable defect, regardless of size, was counted. They were sorted in broad categories of size magnitude. As discussed before, defect size influences the fracture behavior of WC-Co hard metals [41]. The greatest dimension of a defect is thereby of significant relevance. For size classification, only the largest measurable diameter of each defect was considered. Defects with a *maximum diameter* ($\emptyset_{max}$) smaller than 0.1 µm were denoted *nanodefects* (*NDs*); those with a maximum diameter greater than 1 µm were denoted *defects* (*Ds*) and those in-between 0.1 µm and 1 µm *microdefects* (*MDs*). They were counted and categorized separately for every position at which a *FIB*-cut was placed. In addition to this quantitative approach, a qualitative assessment of the investigated microstructure was undertaken.

4.2.2.2. *Measuring contiguity and mean free path of the binder phase*

Contiguity and the mean free path of the binder phase (l_{Co}) have already been linked to the mechanical properties of WC-Co hard metals [28, pp. 107–110], [75]. Both were obtained for each specimen. The applied methodology is outlined in Appendix D for contiguity values and in Appendix E for the mean free path of the binder phase. All obtained results are included in Appendix F.

4.3. Results

4.3.1. Ball-in-cone test applicability

The results of all investigations concerning the viability and validity of the *BIC* test are presented in the following. Particular attention was paid to the control, setup degradation and the evaluation method, i.e. the accuracy of *FIB* cut placement.

4.3.1.1. Installation and temperature control

While the installation of the *BIC* test setup was possible without problems regarding either stability or fixation, the temperature calibration proved to be of greater difficulty. Great differences between the temperatures measured by the thermocouples installed on specimen and indenter were an issue. These were primarily attributed to the volume differences of specimen and indenter in combination with thermal barriers created by both the use of different materials for the components and vacuum in-between the parts. The complex *BIC* test setup geometry was expected to result in inhomogeneous eddy currents. The temperature field in the test setup was therefore expected to also be inhomogeneous. For temperature calibration, setup and specimen Dβ01 were heated repeatedly. The sample positions relative to the induction coil were varied several times. The temperature range was from *RT* to ~850 °C. The results as well as the identified temperature trend are displayed in *Figure 13*.
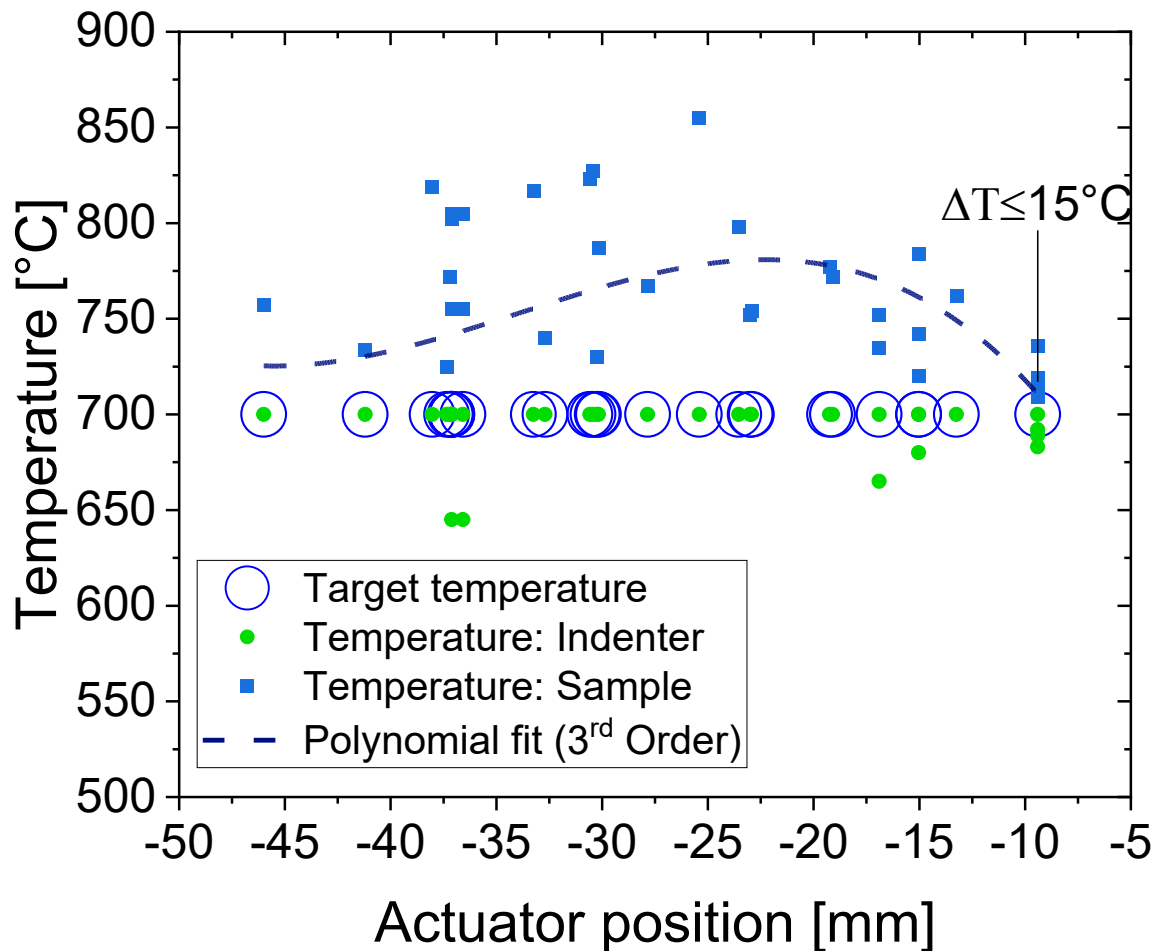
Figure 13: Temperature signals from thermocouples mounted at sample and indenter as a function of actuator position. A polynomial fit of the 3rd order shows an ideal position close to -5 mm with a minimum temperature difference between sample and indenter below 15 °C.

The abscissa shows the positional range of the servo-hydraulic testing machine's actuator with a full range from -50 to +50 mm. The positions described in the following are outlined in *Figure 14 (a-c)*. An actuator positional value of -50 mm denotes a position with the sample located in the middle section of the induction coil, see *Figure 14 (a)*. At -25 mm in *Figure 14 (b)* the sample is only partially immersed in the lower part of the induction coil. It is almost fully immersed at -5 mm. The sensitivity of the setup's temperature to positional changes proved the main hindrance to temperature control. Without change in position the same temperature was achievable. However, maintaining the exact same position while e.g. changing a sample proved impossible. Consequently, a range with acceptable tolerance to slight positional changes was sought. A sufficient range was found in actuator positions -10 to 0 mm visualized in *Figure 14* (*c*). In this

positional range the temperature differences were always below 35 °C. To minimize the asymmetry of temperature differences in sample and indenter the following procedure was used: Once the temperature had not changed within 15 minutes the actuator position of the *BIC* test setup was adjusted. Thereafter the temperature difference to 700 °C for indenter and sample was identical. The resulting temperature difference was e.g. 695 °C and 705 °C for indenter and sample thermocouples respectively instead of 700 °C and 710 °C. For most performed tests, the so achieved temperature difference was smaller than 15 °C.
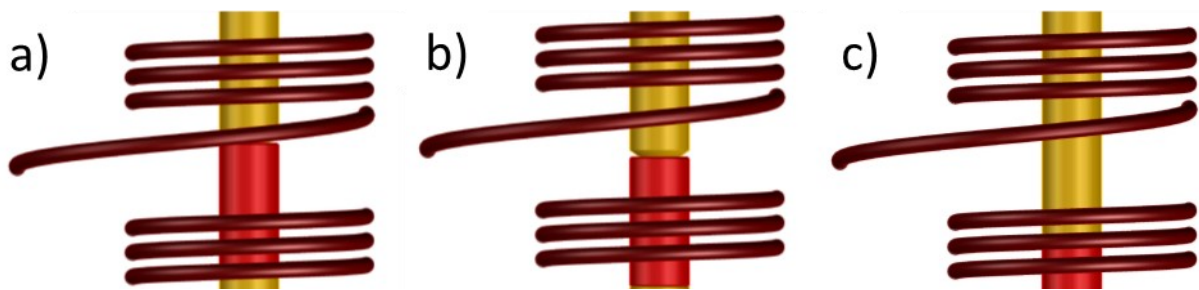
Figure 14: Three positions of the sample in the BIC test setup as a function of the imposed actuator position: (a) -50 mm, (b) -25 mm, (c) -5 mm.

4.3.1.2.   Degradation of the indenter

Regarding the degradation of the indenter, especially of the surface in contact with the specimen, the performed investigations yielded the results shown in Figure 15 *(a-b)* in *SEM* micrographs in *SE* contrast mode. The graphs show a particularly damaged part of contact area on the spherical indenter surface. From the shown point of view, the tangential load is applied along the horizontal axis; the central axis is on the left side. The shown graphs were taken after setup calibration and 3,360 load cycles as well as 15,110 load cycles. Only macroscopic documentation of the initial state of the indenter surface was done.

While the indenter surface showed some defects and faults after 3,360 load cycles, most are oriented arbitrarily to the tangential load direction, which is vertical from right to left in *Figure 15 (a)*. Some fine grooves and scratches are visible, predominantly diagonal from the bottom left to the top right of the graphs. Larger grooves for the most part share this orientation. Only few grooves on the outer fringes of the contact area are parallel to the tangential load direction. Any aberrations suffered from the normal load are undetectable with the employed methods. As a

whole, the indenter surface appears largely unchanged by use in the *BIC* test. Individual scratches, grooves or defects can be explained by the indenter's seen use. The vast majority of visible aberrations from an ideal spherical surface are however inexplicable with only the *BIC* test and most likely stem from manufacture.

After 15,110 load cycles the situation has somewhat reversed. Now the majority of visible grooves, however shallow, is oriented parallel to the tangential load direction. The center of the contact area also shows a marked discoloration compared to the outer fringes and earlier documentation, visible in *Figure 15 (b)*. Former deep grooves and scratches appear distinctly shallower while new ones are detectable, oriented in parallel to the tangential load direction. After 15,110 load cycles the damage remained superficial. However, the contact surface of the indenter slightly changed. This also allowed visual determination of the remaining contact area width. The width of the contact area between sample and indenter was determined from *Figure 15 (b)* via measurement of the remaining discolorations on the indenter. It was assumed that the constant load of -1,200 N was the cause of the more intense discoloration marked by *Figure 15 (b-1)*. The so measurable contact width was at ~100 µm. Due to elastic-plastic deformation of specimen and indenter, the measured width was ~500 µm for the -12,000 N load.
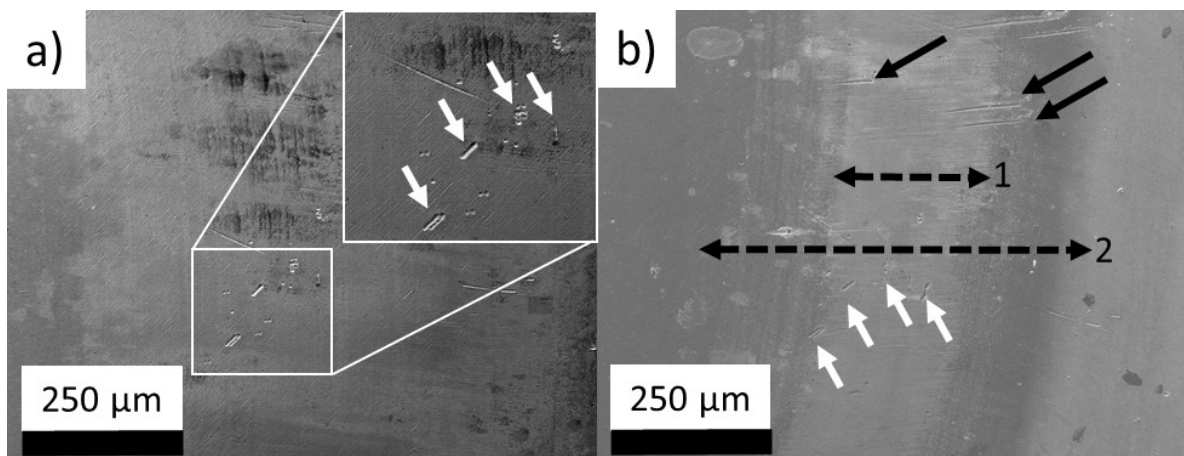
Figure 15: SEM micrographs showing the surface of the indenter. (a) After temperature calibration and 3,360 load cycles some superficial damage is visible. (b) After 15,110 load cycles (N) new superficial damage is observable. Defects detectable in (a-b) are marked with white arrows. Defects only *visible in (b) are marked with black arrows. Measured contact widths for -1,200 N (1) and -12,000 N (2) are indicated by the black, dotted double arrows.*

4.3.1.3.   Accuracy of ROI positioning

Finally, the positioning of the *FIB* cuts in the *ROI* was investigated. Whether the positions correlated with their actual placements shall be answered in the following. No designated investigation for the positioning itself was performed. Rather, it was conducted using a simple pattern: From the simulation, the radial distance of the relevant positions was well known. This distance had to be adjusted in consideration of the 14° skewering angle of the samples inverted cone. The approximate azimuthal position was fixed in respect to circumferential markers placed at 120°, shown in *Figure 16 (a)*. With this procedure the positions were each hit with an approximate accuracy of ± 50 µm in radial direction. *FIB*-cuts for the central position (*P1*) and the fringe positions (*P2-3*) obtained via this procedure are representatively shown in *Figure 16 (b)*.
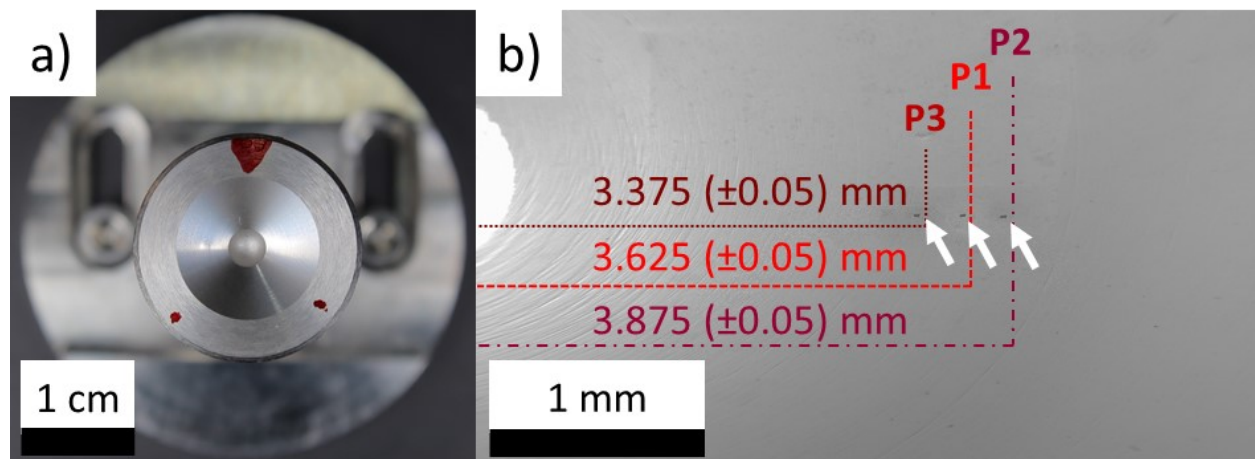
Figure 16: Azimuthal and radial positioning of the FIB-cuts by example of specimen Dβ02*. (a) Documentation by standard photography. Markers for the correct azimuthal positioning of the FIB cuts are visible. The first azimuthal position was chosen randomly; the following with respect to the first. (b) A SEM surface micrograph of the same specimen after 5,000 load cycles. The distances of the positions from the specimen's central axis are indicated with dotted lines. The visible FIB-cuts are marked with white arrows.*

4.3.2. Substrate damage evolution with progressive load cycles

Before any substrate-focused investigation, the specimen surface in the area of specimen-indenter contact was investigated. The most relevant results are shown in *Figure 17*. Direct comparison shows that visually, the specimen changes on a macroscopic level. From 10 load

cycles in *Figure 17 (a)* to 10,000 load cycles in *Figure 17 (b)* those alterations, while visible, remain minor. In the main, change is expressed by a slight discoloration after 10,000 load cycles of the specimen as a whole and the contact area in particular.

On a microscopic level, no clear distinction between a specimen surface in its initial state and loaded for 10 or 10,000 load cycles was possible. While clear grooves are visible in *Figure 17 (a-c)* their most likely causes are manufacturing processes. Distinctive asperities are visible regardless of load cycle count; they represent deviations from an ideally flat surface usually assumed e.g. for simulations.
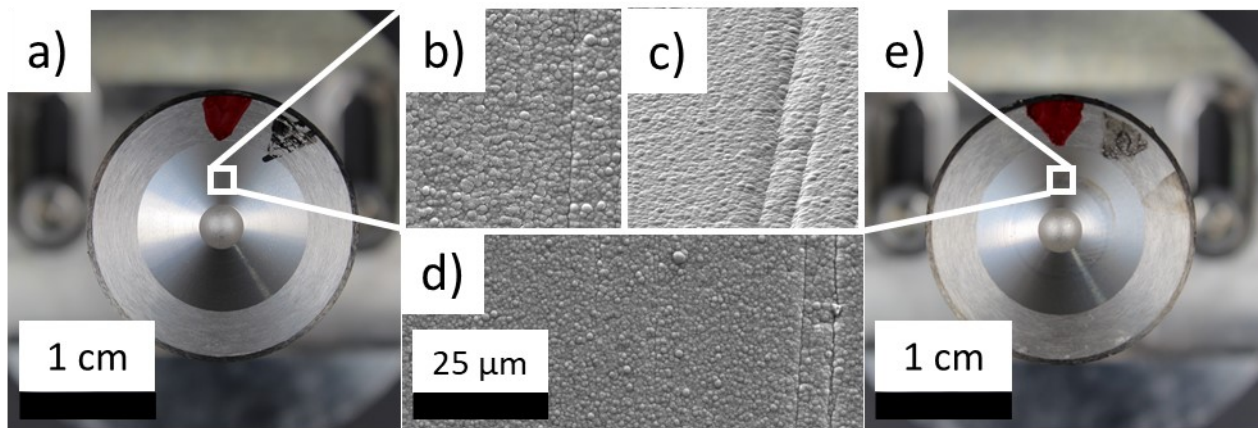
Figure 17: Macroscopic (a, e) and microscopic (b, c, d) surface documentation of specimens in virgin and tested states. The macroscopic documentation was conducted using standard photography. The SEM micrographs are in SE contrast mode. Differences in brightness are due to differences in the viewing angles. (a-b) Macroscopic and microscopic surface documentation of specimen DΒ04 after 10 load cycles. (c, e) Microscopic and macroscopic surface documentation of specimen DΒ02 after 10,000 load cycles. (d) Microscopic surface documentation of specimen DΒ04 in virgin state. The scale in (d) is also valid for (b-c).

As first result of the investigations focused on the specimen substrate, the microstructure of a representative specimen is shown on a *FIB* cut in *Figure 18* from the surface to the substrate.
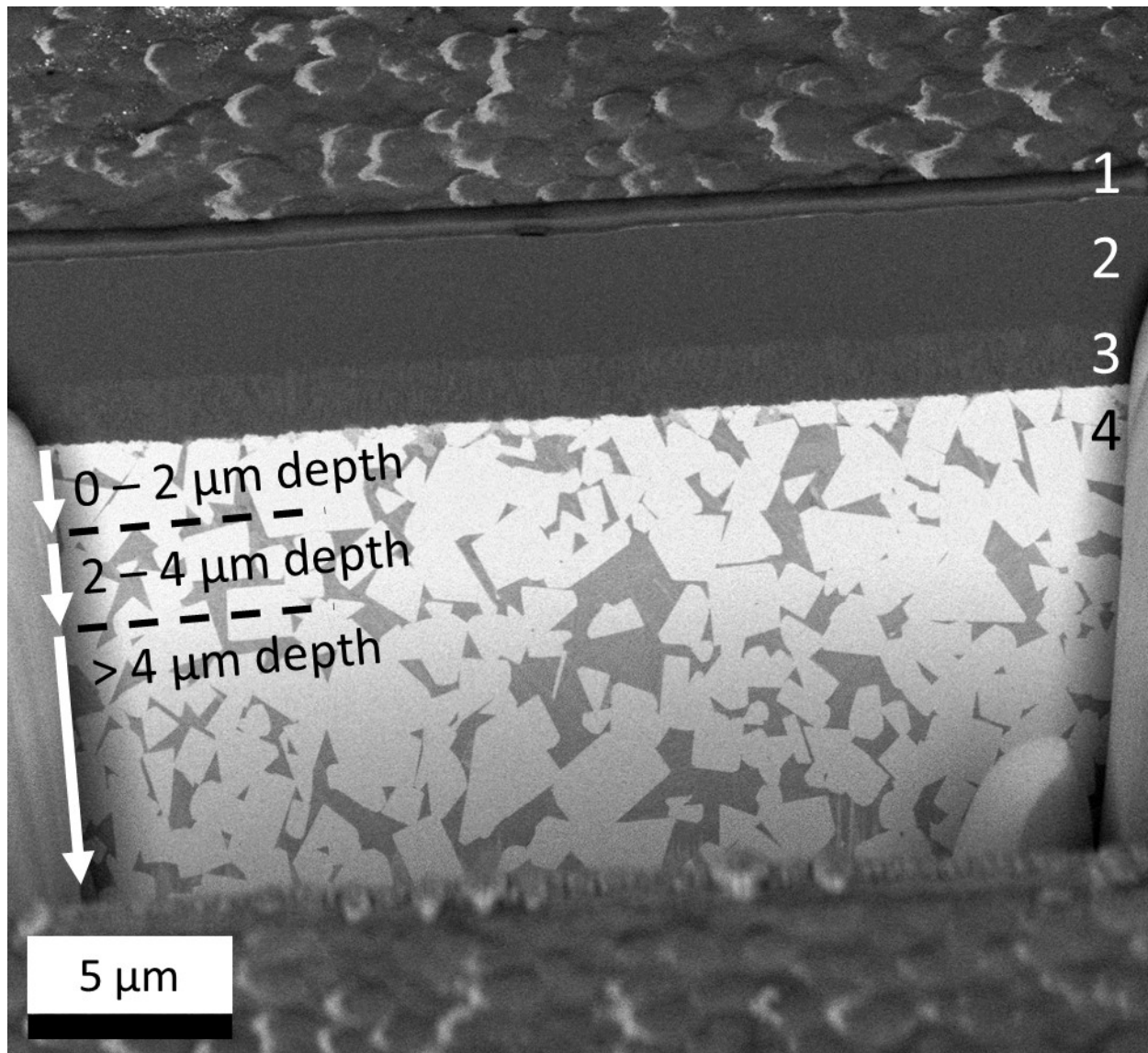
Figure 18: SEM micrograph in EBS contrast mode of a FIB-cut on specimen Dβ02 after 5,000 load cycles. From the surface downwards the for FIB-cutting necessary Pt-layer (1) is first. Below follow the TiB$_2$ (2) and the TiN (3). Last is the substrate (4). The in this contrast brighter tungsten-carbide grains (WC) are clearly distinguishable from the darker Cobalt-phases (Co). The distances to the coating-substrate interface (depths) relevant for later analysis are highlighted on the left side.

To count defects, proper differentiation of a defect from its surrounding phases is required. To this end the *SE* and *EBS* contrast mode were utilized. Every investigated position was documented in both modes; by comparing a position in both contrast modes, even a defect of

poor visibility was exposed due to the differences in contrast. The basic principle is outlined in *Figure 19 (a-b).*
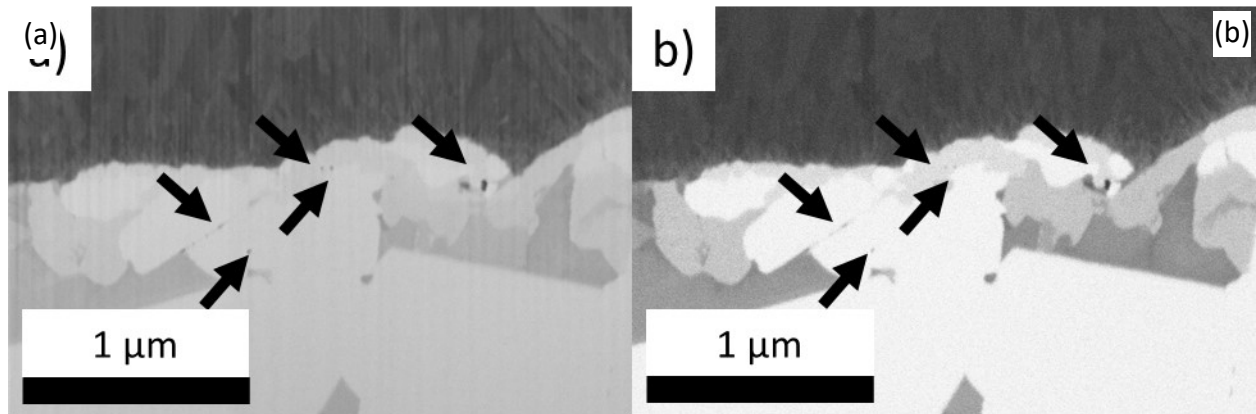
Figure 19: Process for detection of defects with poor visibility by example of specimen Dβ03 after 1,700 load cycles. (a) The SEM micrograph in SE contrast mode. (b) The SEM micrograph in EBS contrast mode. In both micrographs defects are dark in direct comparison with the surrounding substrate. Visible nanodefects are marked with black arrows in both micrographs.

On a purely qualitative basis, several distinctive types of defects were observed. While there was some fluctuation of shape and size, the main features of those defects remain unchanged, as shown in *Figure 20 (a-e)*. All three main types of categorization by size are represented; *nanodefects* (*ND*) with a maximum diameter <0.1 µm, *microdefects* (*MD*) >0.1 and <1 µm, *defects* (*D*) >1 µm. Microdefects were further distinguished by shape.
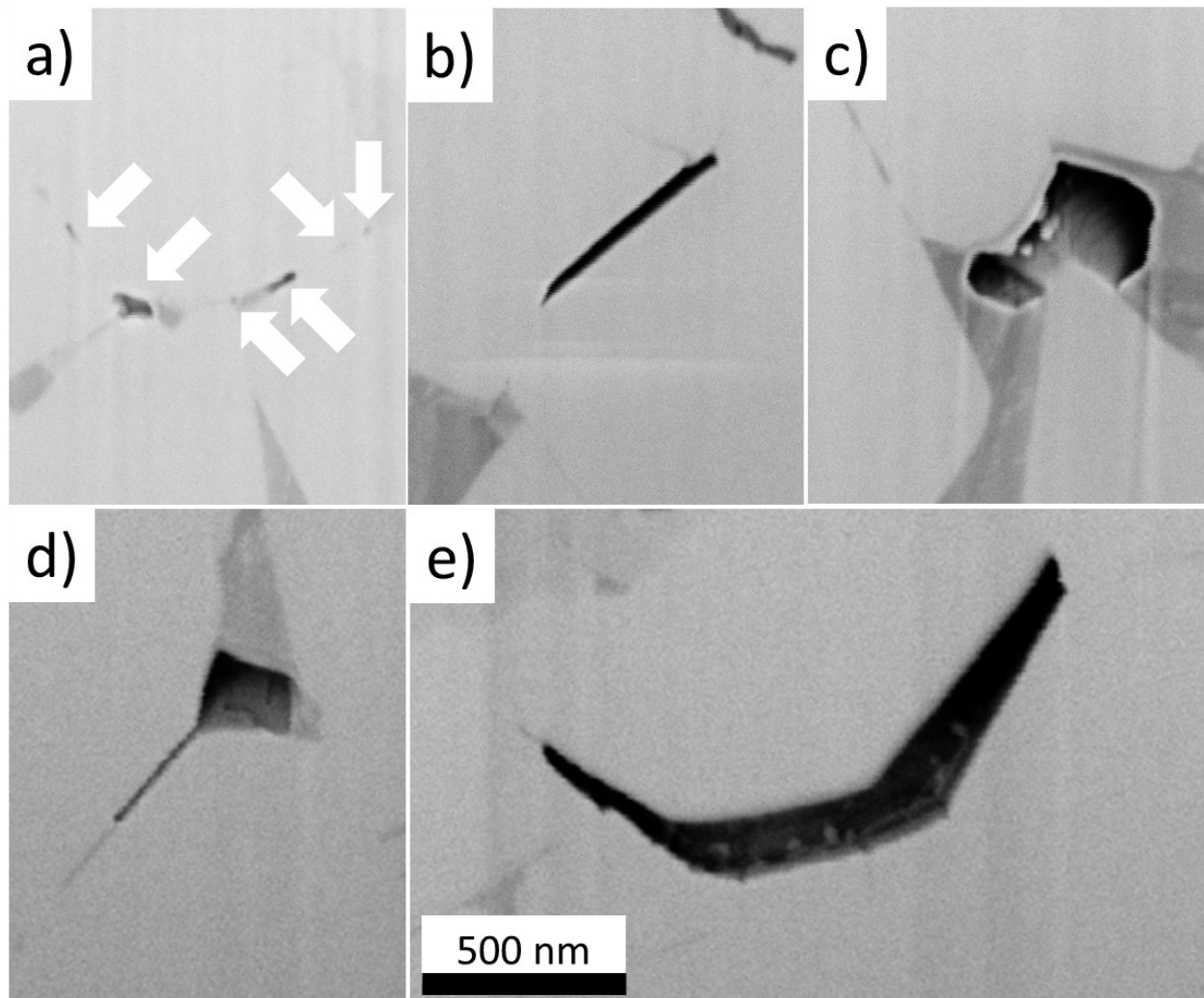
Figure 20: Several size and shape categories were distinguished. Representative examples are shown in (a-e). (a-c) Micrographs from sample Dβ02 after 3,400 load cycles in P2, in SE contrast. (d- (e) Defects documented in specimen Dβ03 after 2500 load cycles in P3, in SE contrast. The categories are as follows: (a) Nanodefects with $\varnothing_{max} < 0.1 \mu m$; (b-d) Microdefects with $0.1 \mu m \leq \varnothing_{max} \leq 1 \mu m$; (e) Defect with $1 \mu m < \varnothing_{max}$.

Figure 20 (a) shows typical *NDs*, both singular and arranged in a string, marked with white arrows. They always exhibit a circular shape. In *Figure 20 (b)* an elongated microdefect denoted type I (*TI*) is shown. Microdefects (*MDs*) with their maximum extension larger than three times their minimum extension were allocated to *TI*. In *Figure 20 (c)* the other main type of *MD* can be observed; its measured maximum and minimum extension typically do not differ by much. Consequently, it features a roughly circular shape. From here on, it will be referred to as an *MD*

45

of type II (*TII*). Finally, *Figure 20 (d)* shows a hybrid type of microdefect; an elongated *TI* joined with a circular *TII* and hence denoted as type III (*TIII*). *Figure 20 (e)* shows a typical category *D* defect. Typically, its maximum extension far exceeds that of the minimum extension. These defect types were identified as typical and counted (see Appendix C). The results are shown in *Figure 21 (a-c)* for positions *P1-3*.
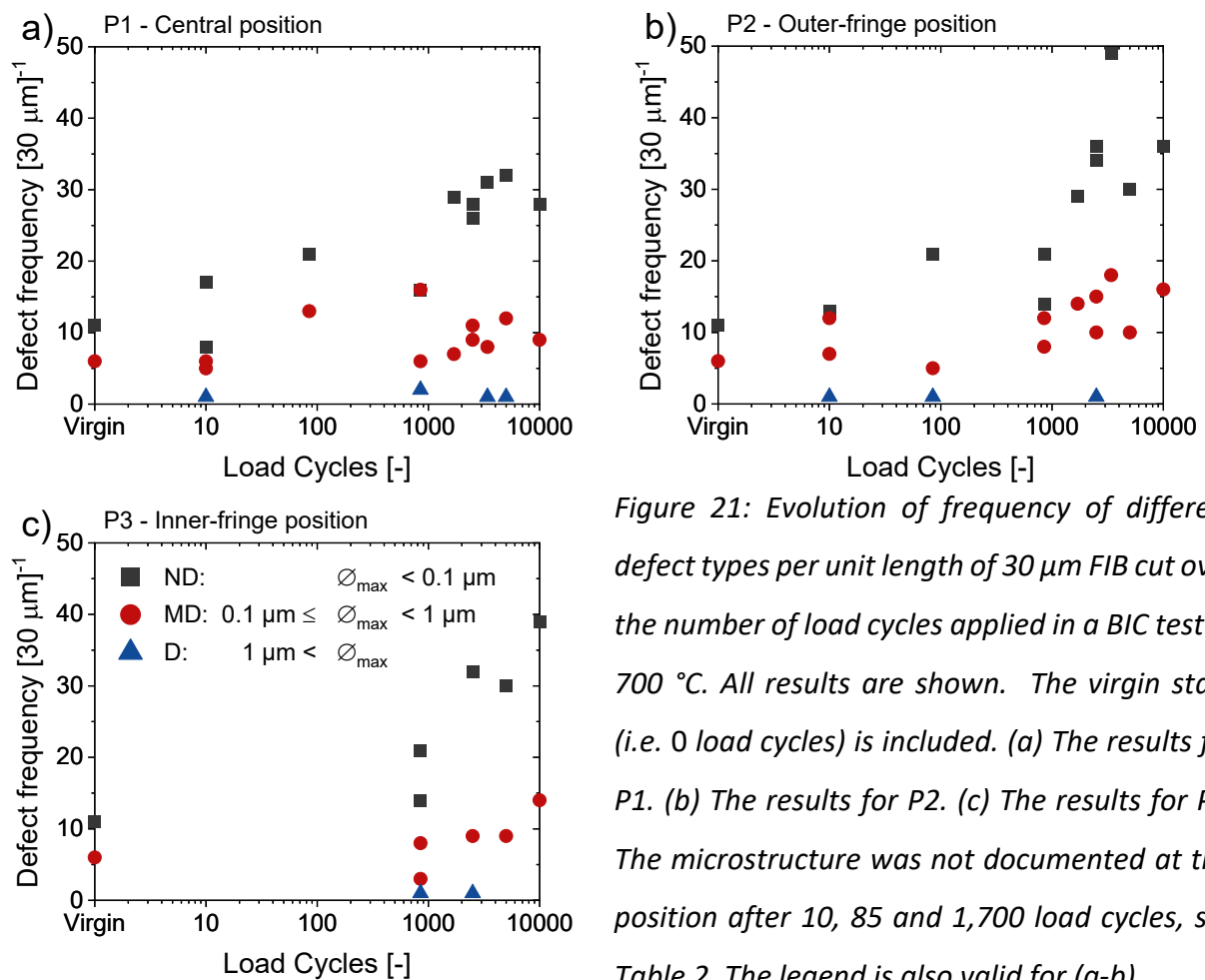
Figure 21: Evolution of frequency of different defect types per unit length of 30 µm FIB cut over the number of load cycles applied in a BIC test at 700 °C. All results are shown. The virgin state (i.e. 0 load cycles) is included. (a) The results for P1. (b) The results for P2. (c) The results for P3. The microstructure was not documented at this position after 10, 85 and 1,700 load cycles, see Table 2. The legend is also valid for (a-b).

At each position, a clear rise in defect frequency with progressing load cycles is observed. While the central position *P1* in *Figure 21 (a)* shows a clear growth in numbers of nanodefects (NDs) in the first 1,000 load cycles, their count mostly stagnates later on. *MDs* and *Ds* show only slight, if any, growth in numbers by comparison. However, no *Ds* were observed at 0 load cycles. For the outer-fringe position *P2* in *Figure 21 (b)* the defect count exhibits near-exponential growth for *NDs*. With *MDs* the situation is not as clear, but growth in numbers is still pronounced. At the inner-fringe position *P3* in *(c)* the situation is similar to that of *P2*, yet less pronounced in terms

of absolute defect count. To enhance readability, *TI-III* were not distinguished in Figure 21 *(a-c)*. However, this was done in Figure 22*, with only the development of *MD* types for the investigated load cycles shown.

In *Figure 22 (a-c)*, the ratio of each defect type count to the sum of all microdefects is displayed as a function of the applied load cycles number to highlight the development of defect shape distribution. For the central position *P1* in *Figure 22 (a)*, the ratio of *TII* defects increases in contrast to that of *TI* defects which decreases, three outliers excepted. The increase of the *TII*-ratio is observable despite the slowed *MD* formation rate at this position at load cycle numbers above 1,000. A similar development takes place at the outer-fringe position *P2* in *Figure 22 (b)*, also with several outliers. Regarding the inner-fringe position *P3* in *Figure 22 (c)*, at least for the load cycles at which investigations were performed the ratios appear relatively stable with *TI* defects most pronounced at the higher load cycle numbers. For all three positions, the ratio of *TIII* defects was at a rather constant, albeit low, level.
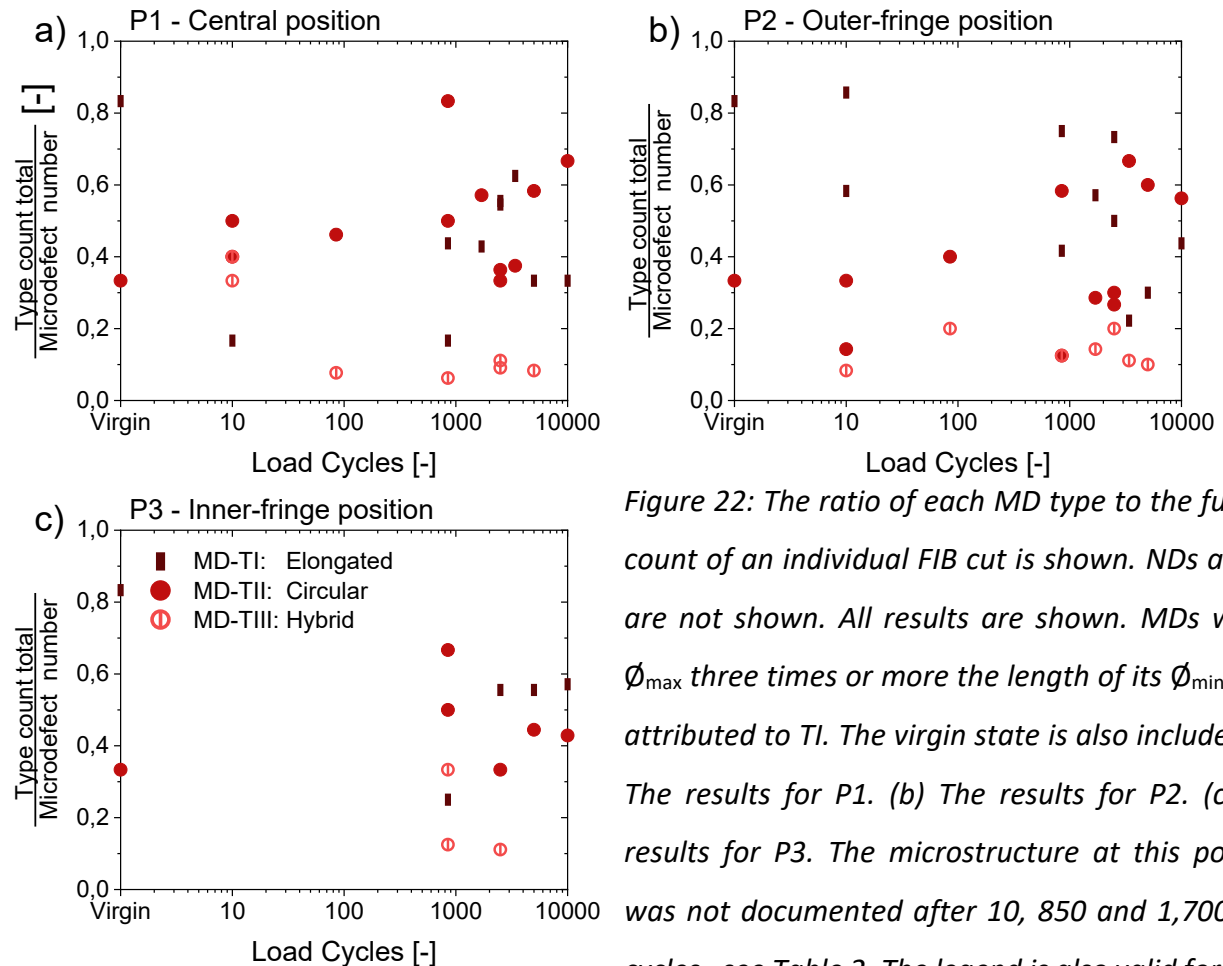
Figure 22: The ratio of each MD type to the full MD count of an individual FIB cut is shown. NDs and Ds *are not shown. All results are shown. MDs with a* $\emptyset_{max}$ *three times or more the length of its* $\emptyset_{min}$ *were attributed to TI. The virgin state is also included. (a) The results for P1. (b) The results for P2. (c) The results for P3. The microstructure at this position was not documented after 10, 850 and 1,700 load cycles. see Table 2. The legend is also valid for (a-b).*

In addition to these distinctions hereby another one was investigated: That of depth. In *Figure 23 (a-c)* defects up to 2 μm below the substrate-coating interface, below more than 4 μm and those in-between are distinguished (see Appendix C). Defects of ambiguous depth were allocated as the majority of their cross section lay. All *NDs*, *MDs* (not distinguishing type) and all *Ds* are shown by count
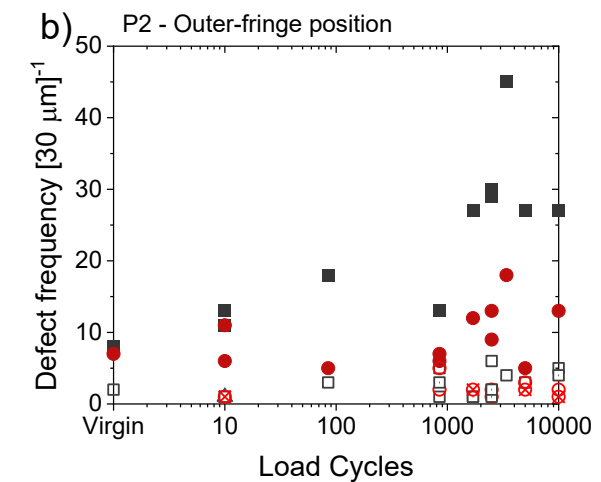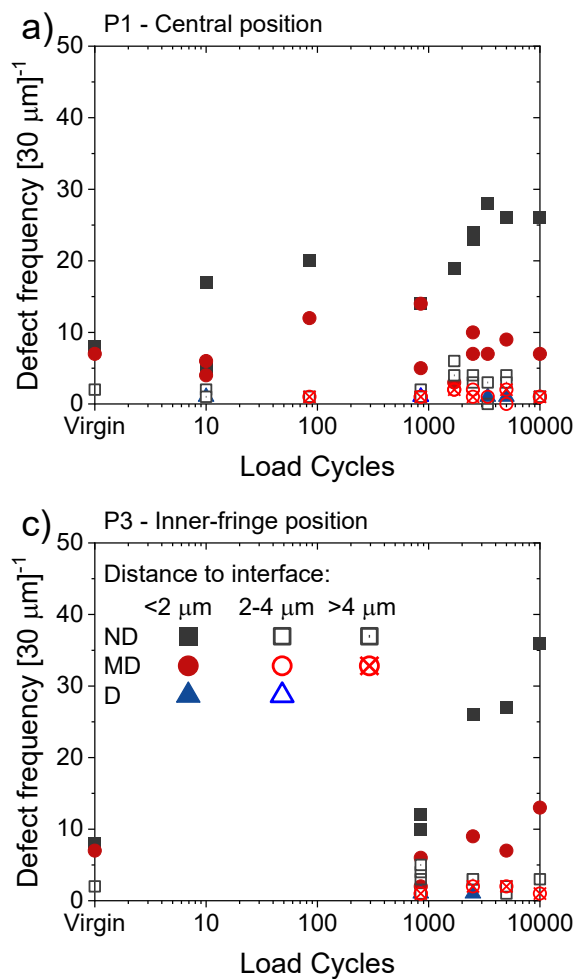
Figure 23: The full count of each defect categorized by size and distance from the interface (i.e. depth) over the load cycle number is shown. The following depths are distinguished: 2 μm, 2 μm to 4 μm and below 4 μm. (a) The results for P1. (b) The results for P2. (c) The results for P3 with no data for 10, 85, 1,700 load cycles, see Table 2. The legend is also valid for (a-b).

For all three positions the predominance of defects at above 2 μm is observable. However, with increasing load cycle count, the number of defects at greater depths also increases. At the central position *P1* in *Figure 23 (a)* defects, particularly nanodefects, are found below 2 μm depth after the first few load cycles; their rate of initiation approximately proportional to that of defects above 2 μm. At the outer-fringe position *P2* in *Figure 23 (b)* and inner-fringe position *P3* in *Figure 23 (c)* the observed developments are similar. Across all investigated positons, the *ND* nucleation rate appears relatively constant regardless whether *NDs*, *MDs* or *Ds* are considered.

4.4. Discussion

4.4.1. The ball-in-cone test: Introducing multi-axial loads into coated WC-Co substrates

As the investigations have shown, installation of the *BIC* test in the testing apparatus as well as the testing procedure per se posed no difficulties. The induction heating, however, did. As presented in the previous chapter[6], considerable temperature gradients proved a hindrance to initial testing. During temperature calibration, this could be resolved. The specimen Dβ01 was used for temperature calibration and was exposed to elevated temperatures up to 800 °C at a constant load of ~500 N for several hours. It was later also tested and its microstructure compared to that of specimens Dβ03-4 which were tested in the same conditions, to the same load cycle number. However, they had not been exposed to elevated temperatures for a comparable time-span. The number and size of observable defects was similar in all three specimens. Consequently, creep in specimen Dβ01 during temperature calibration was likely negligible.

Once temperature calibration was finished and a procedure had been established by placing the specimen in the found optimal position, the measured temperatures homogenized. In the vicinity of the indenter-specimen contact the temperature gradient was seen as negligible. Considering the complexity of inductive heating, that assumption needs to be critically observed. Due to the vacuum, the conductive heat transmission coefficient between test setup and surrounding atmosphere can be assumed as close to zero, since convective heat transmission is reliant on a fluid medium [144, Ch. F]. At the same time WC-Co hard metals are known for their high thermal conductivity [35]. Following the idealized Biot-concept for thermal gradients in bodies, any such gradients are assumedly negligible in the studied specimen [144, Ch. E]. Consequently, the temperature field of the specimen body is assumed to be roughly homogenous with no significant differences from edge to core temperature. This in part validates the basic assumption of correct temperature measurement in the described *BIC* test setup.

However, taking into account eddy current effects of induction heating like the skin effect the situation is less clear. These effects after all cause non-uniform current distribution throughout sample and indenter, with increased power density in surface-near regions. The skin

---

[6] See Chapter 4.3.1.1. *Installation and temperature calibration*.

effect is most pronounced for magnetic materials below their Curie temperature [145, pp. 60–66]. Due to the ferromagnetic Co, WC-Co hard metals are magnetic at *RT*. However, the chosen testing temperature is in the vicinity of the Curie temperature of the sample material, which has been measured at 750 to 1000 °C and linked with the amount of WC dissolved in Co [146]. This means that the skin effect likely is somewhat dampened in its magnitude. This, in all probability, extends to related effects like the longitudinal end effect, which sees increased power density for the coil-submerged end of cylindrical bodies [145, pp. 79–85]. To conclude, the impact of the skin effect is hard to estimate by theoretical considerations alone.

An indication may be provided in [147]: The temperature gradient in induction coil-submerged WNiCo heavy alloy cylinders of similar proportions to the *BIC* test setup was studied. Numerical simulation and experimental validation of several minutes of inductive heating was conducted. At the cylindrical ends, the predicted temperature difference between shell and central axis of the cylinder was ~30 °C. Yet the temperatures were not held constant for an extended time span as is the case with the *BIC* test. Assuming an equally or more homogenous temperature distribution in thermal equilibrium consequently seems admissible. The assumption of appropriately accurate temperature measurements at the allocated positions close to the contact area as shown in Figure 12 (a) can be considered sufficient for initial testing. Nonetheless, further measures regarding the temperature control and the accuracy of measurements merit consideration in future applications of the *BIC* test. Those may include e.g. additional thermocouples installed at a greater distance to the contact area or thermal imagining of sample and indenter at test temperature for improved knowledge of a surface temperature gradient.

Regarding prolonged use of the *BIC* test components, the multiple use of the specimens proved highly effective. A clear progress of substrate damage was observable in all specimens, as *Figure 21 (a-c)* shows. At the same time, *Figure 17 (a-c)* shows an unchanged specimen surface quality regardless of the number of load cycles they were subjected to. This indicates that the substrate, as intended, is the main recipient of plastic deformation and damage in the sample. The indenter, however, exhibited clear signs of superficial degradation shown in *Figure 15 (a-b)*.

The original orientation of the minuscule grooves shown in *Figure 15* was lost in the center of the contact area. There, permanent contact between sample and indenter was sustained

throughout the entire duration of the applied load cycles. Those grooves are oriented parallel to the direction of tangential load. In addition, several new grooves and surface damages are visible, of likewise orientation. The change of groove orientation in particular is likely due to some relative motion of specimen and indenter either during or in-between load cycles. This relative motion may be due to elastic deformation of indenter and sample. The groove orientation shows a declining gradient in discoloration intensity from the center of the contact area outwards to the outer and inner fringe. Consequently, the orientation parallel to the tangential load direction is most pronounced in the center of the contact area, where permanent contact is ensured.

The concurrent lack of concentric circular grooves and surface damage features indicates that relative azimuthal motion of indenter and specimen during testing is mostly negligible. It is therefore probable that most, if not all, relative motion of indenter and sample is restricted to that of radial slip in the course of each load cycle [148], [149]. Exemplary grooves are marked with black arrows in *Figure 15 (b).* The grooves also represent a change in indenter-specimen contact. This is a deviation from both the initial contact situation and the idealized situation assumed for the simulation. Also, the relative azimuthal position of sample and indenter was not marked. Therefore, once a specimen is removed from the testing apparatus for examination, the initial relative azimuthal position of indenter and specimen cannot be reproduced. In visual inspection the specimen surface was observably homogenous. However, roughness asperities might produce a significant yet hard to estimate change in the local stress situation. This change could be alleviated by providing a marking on both sample and indenter for correct alignment in future applications of the *BIC* test.

4.4.2. Experimental validation of the ball-in-cone test finite element simulation

The simulation was used to predict sites subjected to the highest loads. At the investigated sites, considerable damage evolution was observable. While the stress situation itself can be expected as sufficiently portrayed in the first load cycle, a distinctive deviation of experiment and simulation with progressing load cycles is concerning. At 10,000 load cycles, the contact width at the minimum compressive load of -1,200 N is, in the *FE* model, estimated at 489 µm. On the indenter after 15,000 load cycles the largest measureable extent of visible contact traces was caused by the maximum compressive load of -12,000 N. It measured ~500 µm, shown in *Figure*

15 (b). Because the employed *FE* model considers the ratchetting effect linearly, this is the most likely cause for this overestimation. The implementation of a model correctly considering the ratchetting effect should therefore be considered a priority before future use of the *BIC* test.

Ideally, the remaining indentation on a sample could also be used as a means of validation of the simulation. However, the fact that the simulation predicted a maximum indentation depth of 3 μm after 10,000 load cycles any available experimental measurement of such a small depth was considered unreliable. The maximum depth would be overestimated due to the models inherent weakness in correctly considering ratchetting. In addition, any depth measurement could only occur in relation to the surrounding surface, itself inclined at 14°. This inclination would impose additional difficulties on measuring apparatuses as e.g. atomic force microscopes. However, an optical investigation capable of both sufficient resolution and consideration of the surface inclination, as e.g. a white-light interferometer [150], could conceivably be used for validation and is hereby recommended where possible.

4.4.3. Evolution of damage in hard-coated WC-Co hard metal substrates

The microstructural parameters of contiguity and mean free path of the binder phase were measured for all investigated specimen and have shown excellent agreement with values reported in literature (see Appendices D-F). For both parameters the average values remained similar, whether the individual values were averaged by specimen or depth. The scatter of the obtained values was considerable, which was also observed in other works [151], [152].

The damage behavior of the studied WC-Co hard metal displays several distinct trends. Foremost, practically all observed defects were located in the binder phase. Very rarely, small pores in the carbide grains were found and once a carbide grain which appeared cracked was detected (see Appendix B, *Figure 27,* 3,400[th] load cycle at *P3*, blue marking). Regarding damage initiation, there is the sensitivity to stress ratio including tensile components. This has been observed in previous works and sees further validation with the results delivered by the *BIC* test [5], [98], [153]. The defect initiation, in particular of the nanodefects, initially shows faster kinetics where there are mainly compressive stresses. The defect formation rate progression remains linear and later stagnates, as shown in *Figure 21 (a)*. This stagnation also correlates with a reduced stress amplitude. In contrast, at the fringe positions where a combination of tensile-compressive

stresses was prevalent, the ND formation rate increases continuously, as seen in *Figure 21 (b-c)*. This indicates that any tensile component is more damaging than greater, mainly compressive stresses. Regarding the general formation of nanodefects, the most likely causes are Co self-diffusion and vacancy agglomeration enhanced by the elevated temperature and subsequent void formation. This has been reported in literature and the formation of such voids can be considered as origin for further cracking and failure [15].

Besides nanodefects, microdefects also show clear numerical growth at all investigated positions, as visible in *Figure 21*. The trend was more pronounced at the fringe positions than at the central position. In general, *MDs* exhibited three distinct shapes of varying frequency. The fraction of each shape type of the total microdefect count was observed to change with the number of load cycles. With progressing load cycles, the circular shape type *TII* increased in prominence, as shown in *Figure 22*. The ratio of circular-shaped *MDs* starts at approximately 0.33 at all positions studied at low load cycle numbers. With progressing load cycle numbers, this ratio increases significantly to almost double that at the central position and slightly less at the fringe positions. The hybrid *TIII* microdefects constitute a constantly small fraction.

The shape of each type can be explained by the dependency of possible shapes on the defect position. Elongated defects occur only in-between WC grains, where the Co-phase intercepts are small and there is little binder phase. Thin intermediate layers of only two monolayers thickness have been observed at straight facets of WC grains [154]. Co has a higher propensity for creep compared to WC and dislocation movement is limited in very thin binder phase layers. Considering this, the formation of elongated *MDs* may be attributable to void accumulation due to Co self-diffusion. [81], [82], [155]. Given the observed occasional clustering of nanodefects, the formation of such microdefects might occur in stages. Assumedly several NDs would form in close proximity to each other and at a later stage either join either by growth or formation of new nanodefects in the gaps between the defects. NDs were sporadically found forming strings consisting of several individual nanodefects and sometimes smaller circular microdefects (see Appendix B). This is consistent with the model concerning the formation of new *NDs*. These nanodefect strings likely form because the loaded cross section between defects is reduced and local stresses therefore increased. Also, due to the significant difference in the yield strengths of Co [156] and WC [54] at 700 °C, plastic deformation occurs more readily in the Co

phase. Consequently, nanodefect growth in thin Co intercepts is likely constrained by the WC-Co interfaces.

With increasing load cycle number, the circular-shaped microdefects made up a growing fraction of the total *MD* number, as seen in *Figure 22*. In contrast to the elongated *TI* microdefects, they are most often initiated at WC-Co interfaces with binder phase hinterland. This is most likely because their distinct shape cannot be formed in a thin Co intercept. Yet, initiation and propagation may progress similarly as for *TI-MDs*, starting at an atomic void accumulation large enough to qualify as a nanodefect with subsequent defect growth less constrained by WC-Co interfaces. That growth could be caused by further dislocation accumulation in the binder phase. In cyclic loading situations the ratchetting effect has been linked with progressing microstructural damage [91], [92]. Given the correlation of increased circular-shaped microdefect numbers with progressing load cycles, ratchetting might be a cause of increased *TII* formation rates. Considering the sensitivity of WC-Co hard metals to a critical defect size, circular shaped microdefects can be seen as the least harmful shape type [41].

The hybrid *TIII* microdefects found were located at WC grains with only thin Co intercepts in-between which opened to Co hinterland. Two formation patterns appear likely. One possibility is that the hybrid *MDs* grow from one of the other shape types into a hybrid due to their location. The other is that two separate microdefects, one elongated, one circular, form in proximity and join by growth. Because the first model only requires one microdefect to grow, it may be the more likely formation pattern.

In addition, several defects with a maximum diameter greater than 1 µm were found, as shown in *Figure 21*. Considering the possible correlation between surface fatigue and microstructural defects as proposed by *Sergejev et al.* in [157], the formation of such defects warrants attention. Due to high local stresses experienced by the WC-Co hard metal substrate the critical defect size can be estimated at only an order of a magnitude greater than defects already observed [158].

Regarding defect location, the following observation was made: At greater depths fewer defects were detectable. This clear trend was observable for all investigated positions. This would imply a quickly diminishing stress gradient with increasing distance to the substrate-coating

interface. The *FE* simulation model showed stress reduction with increasing distance to the substrate-coating interface [16]. However, that alone cannot reasonably explain the considerable difference in defect numbers above and below a distance of 2 µm from the substrate-coating interface. Consequently, the model here fails to accurately predict the real stress situation. There is no perfectly flat surface, as shown in *Figure 17* and no ideally uniform microstructure, but both were assumed for the simulation. The considerations described in the following may explain this divergence of simulation and observation.

A rough surface features asperities of varying height and width. These have been shown using *FE* models to significantly influence the stress gradient in a contact situation between two bodies [159]. They contribute to a stress gradient with the stress maxima in the surface-near region. The ratio of asperity height to width was considered as crucial indicator of the stress gradient reduction. For high ratios significant plastic shear strains were calculated close the model body surface. For small ratios the calculated plastic shear strains were lower, but more homogenous. However, for all height to width ratios a significant reduction in the plastic shear strain of the model body was calculated. This reduction was dependent on the distance to the model body surface [159]. The load situation with the ball-in-cone test setup is similar in also featuring normal and tangential loads and the *FE* simulation confirmed the presence of plastic shear strains [16]. The influence of roughness asperities on the plastic shear strain distribution can explain the observed damage gradient. Specimen surface documentation using an *SEM* showed no superficial alterations, as seen in *Figure 17*. However, roughness measurements were neither undertaken for the initial state of the specimen nor after their subjection to the *BIC* test. A change of the asperity height to width ratio due to surface wear therefore cannot be ruled out as origin of the observed trend towards defects at increased depth seen in *Figure 23 (a-c)*. Added roughness measurement in a future application of the *BIC* test to either verify or falsify this possibility is hereby recommended.

In a series of works *Yang et al.* studied the effects of grinding on a WC-Co hard metal substrate. They confirmed the existence of a micro crack network [160]. They also observed a change of the Co phase from *FCC* to its brittle *HCP* state [161]. In addition, significant residual compressive stresses to a substrate depth of about 12 µm were measured [162], [163]. All of the above were observed as most pronounced in the first 2 µm of the substrate. The residual

compressive stresses present in the ball-in-cone test specimen are likely to have been partially alleviated by prolonged exposure to the testing temperature [160], [163]. These were considered mostly beneficial to the substrate, seen as enhancing the damage resistance of the WC-Co hard [162]. The micro crack network likely is not affected by the elevated temperature. These pre-existing defects most likely grow more easily than unformed defects initiate. Such initial damage, i.e. defects of any category, were also observed in a specimen's initial microstructural state. While no investigation able to confirm the existence of the *HCP*-Co phase was employed, such grinding induced phase changes concurrent with microstructural refinement were reported in [161]. Since an *HCP* lattice has a reduced number of glide planes compared to an *FCC* lattice it is usually more brittle [25, pp. 265–272]. If an *FCC* lattice is permeated by small areas of *HCP* lattices, the interfaces between these phases may function as nuclei for *ND* formation due to local differences in strain. These differences arise because the *HCP* phase cannot deform plastically as much as the *FCC* phase. In cyclic loading conditions the cyclic deformation likely intensifies strain localizations in the *FCC* phase in the vicinity of *FCC*-*HCP* phase interfaces. This may be explained with the following effect: At maximum compressive load, the *FCC* phase likely is more deformed than the *HCP* phase. At minimum compressive load, the remaining plastic deformation in the *FCC* phase consequently is greater than in the *HCP* phase. With successive loading, this difference probably increases and so does the probability of *ND* formation. With sufficient Co hinterland, these *ND*s may also grow into *TII-MDs* [25, pp. 265–272].

5. Conclusion

The novel ball-in-cone (*BIC*) test can be considered a well-understood technique to provide an efficient and resource-saving method for the study of damage initiation in metal-ceramic composites such as WC-Co hard metals. The setup provides constructional degrees of freedom in the inclination angle of the sample's inverted cone, the radius of the indenter and component materials. Additional freedom of choice lies in the ambient atmosphere, testing temperature and applied load. The test can be executed in static or dynamic mode.

For the current work, the test was performed for a specimen made of a TiN-TiB$_2$ hard-coated WC-Co hard metal with 12 wt.% Co binder and a mean grain size of ~2 µm. Testing conditions were set at 700 °C in a vacuum atmosphere with a cyclic load of -1,200 minimum compressive and -12,000 N maximum compressive load. Concurrent with experimental testing, an *FE*-based simulation was conducted. A state of the art material model was employed to simulate the stress situation in specimen-indenter contact. The simulation was in part experimentally validated by comparing contact widths measured on the indenter in contact with the specimen at maximum compressive load in simulation. The contact width on the test setup component was measured unloaded on surface discolorations. Deviations between simulation and experimental measurements were attributable to simplifying assumptions used in the *FE* model regarding the cyclic creep behavior of the material. The simulation was used to study the stress situation in the substrate of the *BIC* test specimen.

The main deficiency of this test is its dependency on accuracy of the *SEM* operators. While accurate placement of the *FIB* cuts is possible – as has been shown in experiments – this nevertheless constitutes the greatest unknown variable. This is because a certain inaccuracy cannot be controlled or at least limited other than with strict adherence to a set, unchanging procedure. The experiments also showed further room for improvement for the practical application as well as for the simulative model. The complexities of induction heating and component degradation in particular warrant further consideration. While in theory the temperature measurements and calibrations are sufficient, the following practical measures are recommended for further use of the *BIC* test:

- Additional use of thermocouples farther from the cylindrical ends of sample and indenter to better detect eventual temperature gradients.

- Thermograph studies to visualize the temperature gradients present on indenter and sample surface.

- Indelible markings on indenter and sample to ensure consistent relative azimuthal positioning for repeated assembly and disassembly of the test setup.

- Roughness measurements from the initial state of indenter and specimen surface onwards to quantify superficial alterations caused by the *BIC* test and thereby gain insight on a possible change of the stress situation.

Regarding the simulation, the main improvement hereby recommended is a model simultaneously considering creep and ratchetting. Further precision could be achieved by including the effects of surface roughness on the stress situation in the substrate. Also considering compressive stresses, Co phase-changes and micro-crack networks induced during grinding processes in manufacture would further enhance the model. Even in its initial state, the manufacturing history of a specimen precludes a completely undamaged, uniform microstructure. With progressing damage, there is further deviation from the assumed ideal microstructure; either inclusion of the residual effects from manufacture as reported or modelling a more realistic microstructure distinguishing WC and Co phases could yield more accurate results and predictions.

Experimental application of the *BIC* test also delivered results in good agreement with literature reports. A combination of tensile and compressive stresses was found to induce higher defect formation rates than mainly compressive stresses. Also, close to the substrate-coating interface, damage was more pronounced. This could be linked with the effect of roughness asperities and the microstructural changes introduced during manufacture described above. In addition, it proved the test setup capable of providing means for studying damage initiation and accumulation in multi-axial load situations at elevated temperatures. The test was found to be an efficient way of studying the damage evolution of hard-coated specimen in conditions similar in temperature and load situation to those seen in metalworking tools used e.g. in milling processes.

List of References

[1] H. Kolaska, "Hartmetall - Gestern, Heute und Morgen," *Metall*, vol. 61, no. 12, pp. 825–832, 2007.

[2] Peter Ettmayer, Hans Kolaska, & Hugo M. Ortner, "History of Hardmetals," in *Comprehensive Hard Materials*, vol. 1, Elsevier Ltd, 2014, pp. 3–27.

[3] I. Johansson, G. Persson, & R. Hiltscher, "Determination of static and fatigue compressive strength of hard-metals," *Powder Metall.*, vol. 13, no. 26, pp. 449–464, 1970, doi: 10.1179/pom.1970.13.26.019.

[4] R. O. Ritchie, "Mechanism of Fatigue-Crack Propagation in Ductile and Brittle Materials," *Int. J. Fract.*, vol. 100, pp. 55–83, 1998.

[5] Y. Torres, V. K. Sarin, M. Anglada, & L. Llanes, "Loading mode effects on the fracture toughness and fatigue crack growth resistance of WC-Co cemented carbides," *Scr. Mater.*, vol. 52, no. 11, pp. 1087–1091, 2005, doi: 10.1016/j.scriptamat.2005.02.011.

[6] J. M. Tarragó, J. J. Roa, V. Valle, J. M. Marshall, & L. Llanes, "Fracture and fatigue behavior of WC-Co and WC-CoNi cemented carbides," *Int. J. Refract. Met. Hard Mater.*, vol. 49, no. 1, pp. 184–191, 2015, doi: 10.1016/j.ijrmhm.2014.07.027.

[7] T. Klünsner, M. Jonke, P. Supancic, C. Gettinger, M. Krobath, T. Lube, S. Marsoner, & J. Glätzle, "Fatigue behaviour of WC-Co hard metal under stress ratio and effectively loaded volume relevant to metalworking tool failure," *Int. J. Refract. Met. Hard Mater.*, vol. 80, no. November 2018, pp. 97–103, 2019, doi: 10.1016/j.ijrmhm.2019.01.003.

[8] T. Klünsner, M. Krobath, W. Ecker, S. Marsoner, M. Morstein, & B. Marklein, "Influence of localized cyclic substrate plastification on residual stress, load stress and cracking near the interface between hard coating and WC-Co hard metal substrate," *Int. J. Refract. Met. Hard Mater.*, vol. 82, no. April, pp. 113–120, 2019, doi: 10.1016/j.ijrmhm.2019.04.003.

[9] Haibo Zhang, Qingzhong Lu, Liehua Zhang, & Zhigang Zak Fang, "Dependence of microcrack number density on microstructural parameters during plastic deformation of WC-Co composite," *Int. J. Refract. Met. Hard Mater.*, vol. 28, no. 3, pp. 434–440, 2010, doi:

10.1016/j.ijrmhm.2010.01.005.

[10]   K. P. Mingard, H. G. Jones, M. G. Gee, B. Roebuck, & J. W. Nunn, "In situ observation of crack growth in a WC-Co hardmetal and characterisation of crack growth morphologies by EBSD," *Int. J. Refract. Met. Hard Mater.*, vol. 36, pp. 136–142, 2013, doi: 10.1016/j.ijrmhm.2012.08.006.

[11]   Lutz Krüger, Kristin Mandel, Rico Krause, & Markus Radajewski, "Damage evolution in WC-Co after repeated dynamic compressive loading detected by eddy current testing," *Int. J. Refract. Met. Hard Mater.*, vol. 51, pp. 324–331, 2015, doi: 10.1016/j.ijrmhm.2015.05.005.

[12]   Keng Jiang, Alexander Bezold, & Christoph Broeckmann, "Numerical modeling of the progressive damage in the microstructure of WC-Co hardmetals under fatigue loading," in *Procedia Structural Integrity*, 2019, vol. 23, pp. 451–456, doi: 10.1016/j.prostr.2020.01.128.

[13]   Andreas W. Nemetz, Werner Daves, Thomas Klünsner, Werner Ecker, Jonathan Schäfer, Christoph Czettl, & Thomas Antretter, "Cyclic heat-up and damage-relevant substrate plastification of single- and bilayer coated milling inserts evaluated numerically," *Surf. Coatings Technol.*, vol. 360, no. January, pp. 39–49, 2019, doi: 10.1016/j.surfcoat.2019.01.008.

[14]   Philipp Hoier, Amir Malakizadi, Uta Klement, & Peter Krajnik, "Characterization of abrasion- and dissolution-induced tool wear in machining," *Wear*, vol. 426–427, no. December 2018, pp. 1548–1562, 2019, doi: 10.1016/j.wear.2018.12.015.

[15]   Fuzeng Wang, Kaixun Ji, & Ziyu Guo, "Microstructural analysis of failure progression for coated carbide tools during high-speed milling of Ti-6Al-4V," *Wear*, vol. 456–457, p. 203356, Sep. 2020, doi: 10.1016/j.wear.2020.203356.

[16]   Martin Krobath, "Internal communication: FEM Simulation of the Ball-in-Cone test.," 2020.

[17]   Alexey S. Kurlov & Aleksandr I. Gusev, *Tungsten Carbides: Structure, Properties and Application in Hardmetals*, vol. 184. Cham: Springer International Publishing, 2013.

[18]   Klocke & König, *Fertigungsverfahren 1*. Berlin, Heidelberg: Springer Berlin Heidelberg, 2008.

[19]   Leo Prakash, "Fundamentals and General Applications of Hardmetals," in *Comprehensive Hard Materials*, vol. 1, Elsevier, 2014, pp. 29–90.

[20]   Pankaj K. Mehrotra, "Powder Processing and Green Shaping," in *Comprehensive Hard Materials*, vol. 1, Elsevier Ltd, 2014, pp. 213–235.

[21]   Marlies De Boeck, Micheline Kirsch-Volders, & Dominique Lison, "Cobalt and antimony: Genotoxicity and carcinogenicity," *Mutat. Res. - Fundam. Mol. Mech. Mutagen.*, vol. 533, no. 1–2, pp. 135–152, 2003, doi: 10.1016/j.mrfmmm.2003.07.012.

[22]   "Titanium Price," *15.10.2020*, 2018. https://www.metalary.com/titanium-price/.

[23]   Metalary, "Tungsten Price," *15.10.2020*, 2018. https://www.metalary.com/tungsten-price/.

[24]   A. S. Kurlov & A. I. Gusev, "Tungsten carbides and W-C phase diagram," *Inorg. Mater.*, vol. 42, no. 2, pp. 121–127, 2006, doi: 10.1134/S0020168506020051.

[25]   Günter Gottstein, *Materialwissenschaft und Werkstofftechnik*, 4th ed. Berlin: Springer Vieweg, 2015.

[26]   J. C. Slater, "Atomic radii in crystals," *J. Chem. Phys.*, vol. 41, no. 10, pp. 3199–3204, 1964, doi: 10.1063/1.1725697.

[27]   H. E. Exner, "Physical and chemical nature of cemented carbides," *Int. Met. Rev.*, vol. 24, no. 1, pp. 149–170, 1979, doi: 10.1179/imtr.1979.24.1.149.

[28]   Sabine Lay & Jean Michel Missiaen, "Microstructure and Morphology of Hardmetals," in *Comprehensive Hard Materials*, vol. 1, Elsevier, 2014, pp. 91–120.

[29]   Rico Bauer, Eric A. Jägle, Wolfgang Baumann, & Eric Jan Mittemeijer, "Kinetics of the allotropic hcp-fcc phase transformation in cobalt," *Philos. Mag.*, vol. 91, no. 3, pp. 437–457, 2011, doi: 10.1080/14786435.2010.525541.

[30]   Institut für Seltene Erden und Metalle E.V., "Cobalt," *15.10.2020*. https://institut-seltene-erden.de/seltene-erden-und-metalle/strategische-metalle-2/kobalt/.

[31]   Mehdi Eizadjou, Hansheng Chen, Christoph Czettl, Julia Pachlhofer, Sophie Primig, & Simon P. Ringer, "An observation of the binder microstructure in WC-(Co+Ru) cemented carbides

using transmission Kikuchi diffraction," *Scr. Mater.*, vol. 183, pp. 55–60, 2020, doi: 10.1016/j.scriptamat.2020.03.010.

[32] R. Kieffer & F. Benesovsky, *Hartstoffe*, 1st ed. Wien: Springer, 1963.

[33] J. Dusza, L. Parilák, J. Diblk, & M. Slesar, "Elastic and plastic behaviour of WC-Co composites," *Ceram. Int.*, vol. 9, no. 4, pp. 144–146, 1983.

[34] José García, Verónica Collado Ciprés, Andreas Blomqvist, & Bartek Kaplan, "Cemented carbide microstructures: a review," *Int. J. Refract. Met. Hard Mater.*, vol. 80, pp. 40–68, 2019, doi: 10.1016/j.ijrmhm.2018.12.004.

[35] Hongtao Wang, Tim Webb, & Jonathan W. Bitler, "Study of thermal expansion and thermal conductivity of cemented WC-Co composite," *Int. J. Refract. Met. Hard Mater.*, vol. 49, no. 1, pp. 170–177, 2015, doi: 10.1016/j.ijrmhm.2014.06.009.

[36] Krishan K. Chawla, *Composite materials: Science and engineering, third edition*, 3rd ed. New York: Springer-Verlag New York, 2012.

[37] Thomas Klünsner, "Influence of Microstructure on Material Behaviour of WC-Co Hard Metals under Static and Cyclic Loading Conditions"PhD Thesis, University of Leoben, 2011.

[38] Xuemei Liu, Jianlong Zhang, Chao Hou, Haibin Wang, Xiaoyan Song, & Zuoren Nie, "Mechanisms of WC plastic deformation in cemented carbide," *Mater. Des.*, vol. 150, pp. 154–164, 2018, doi: 10.1016/j.matdes.2018.04.025.

[39] Daniele Mari, "Mechanical Behavior of Hardmetals at High Temperature," in *Comprehensive Hard Materials*, vol. 1, Elsevier, 2014, pp. 405–421.

[40] T. Klünsner, S. Wurster, P. Supancic, R. Ebner, M. Jenko, J. Glätzle, A. Püschel, & R. Pippan, "Effect of specimen size on the tensile strength of WC-Co hard metal," *Acta Mater.*, vol. 59, no. 10, pp. 4244–4252, 2011, doi: 10.1016/j.actamat.2011.03.049.

[41] Robert Danzer, Tanja Lube, Peter Supancic, & Rajiv Damani, "Fracture of ceramics," *Adv. Eng. Mater.*, vol. 10, no. 4, pp. 275–298, 2008, doi: 10.1002/adem.200700347.

[42] Dietmar Gross & Thomas Seelig, *Bruchmechanik*, 6th ed. Berlin: Springer Vieweg, 2016.

[43] Amit Bhaduri, *Mechanical Properties and Working of Metals and Alloys*, 1st ed., vol. 264.

Singapore: Springer Singapore, 2018.

[44]   George A. Gogotsi, "Fracture toughness of ceramics and ceramic composites," *Ceram. Int.*, vol. 29, no. 7, pp. 777–784, 2003, doi: 10.1016/S0272-8842(02)00230-4.

[45]   N. M. Abd-Allah, M. S. El-Fadaly, M. M. Megahed, & A. M. Eleiche, "Fracture toughness properties of high-strength martensitic steel within a wide hardness range," *J. Mater. Eng. Perform.*, vol. 10, no. 5, pp. 576–585, 2001, doi: 10.1361/105994901770344728.

[46]   Thak Sang Byun, David T. Hoelzer, Jeoung Han Kim, & Stuart A. Maloy, "A comparative assessment of the fracture toughness behavior of ferritic-martensitic steels and nanostructured ferritic alloys," *J. Nucl. Mater.*, vol. 484, pp. 157–167, 2017, doi: 10.1016/j.jnucmat.2016.12.004.

[47]   Alex V. Shatov, S. S. Ponomarev, & S. A. Firstov, "Fracture and Strength of Hardmetals at Room Temperature," in *Comprehensive Hard Materials*, vol. 1, Elsevier, 2014, pp. 301–343.

[48]   T. Teppernegg, T. Klünsner, C. Kremsner, C. Tritremmel, C. Czettl, S. Puchegger, S. Marsoner, R. Pippan, & R. Ebner, "High temperature mechanical properties of WC–Co hard metals," *Int. J. Refract. Met. Hard Mater.*, vol. 56, pp. 139–144, 2016, doi: 10.1016/j.ijrmhm.2016.01.002.

[49]   Mark G. Gee, A. J. Gant, B. Roebuck, & K. P. Mingard, "Wear of Hardmetals," in *Comprehensive Hard Materials*, vol. 1, Elsevier, 2014, pp. 363–383.

[50]   V. Richter & M. V. Ruthendorf, "On hardness and toughness of ultrafine and nanocrystalline hard materials," *Int. J. Refract. Met. Hard Mater.*, vol. 17, no. 1, pp. 141–152, 1999, doi: 10.1016/S0263-4368(99)00003-7.

[51]   A. Vornberger, J. Pötschke, T. Gestrich, M. Herrmann, & A. Michaelis, "Influence of microstructure on hardness and thermal conductivity of hardmetals," *Int. J. Refract. Met. Hard Mater.*, vol. 88, no. November 2019, p. 105170, 2020, doi: 10.1016/j.ijrmhm.2019.105170.

[52]   Z. Zak Fang, Mark C. Koopman, & Hongtao Wang, "Cemented Tungsten Carbide Hardmetal-An Introduction," in *Comprehensive Hard Materials*, vol. 1, Elsevier, 2014, pp. 123–137.

[53]   Igor Konyashin, "Cemented Carbides for Mining, Construction and Wear Parts," in *Comprehensive Hard Materials*, vol. 1, Elsevier Ltd, 2014, pp. 425–451.

[54]   Lukáš Faksa, Werner Daves, Thomas Klünsner, Kathrin Maier, Thomas Antretter, Christoph Czettl, & Werner Ecker, "Shot peening-induced plastic deformation of individual phases within a coated WC-Co hard metal composite material including stress-strain curves for WC as a function of temperature," *Surf. Coatings Technol.*, vol. 380, 2019, doi: 10.1016/j.surfcoat.2019.125026.

[55]   Charles E. Mortimer & Müller Ulrich, *Chemie*, 12th ed. Stuttgart: Georg Thieme Verlag KG, 2015.

[56]   S. C. Cifuentes, M. A. Monge, & P. Pérez, "On the oxidation mechanism of pure tungsten in the temperature range 600-800°C," *Corros. Sci.*, vol. 57, pp. 114–121, 2012, doi: 10.1016/j.corsci.2011.12.027.

[57]   Anna Warren, Anders Nylund, & Ingemar Olefjord, "Oxidation of tungsten and tungsten carbide in dry and humid atmospheres," *Int. J. Refract. Met. Hard Mater.*, vol. 14, no. 5–6, pp. 345–353, 1996, doi: 10.1016/s0263-4368(96)00027-3.

[58]   Wang Hoi Gu, Yeon Seok Jeong, Kyeongmi Kim, Jin Chun Kim, Seong Ho Son, & Sunjung Kim, "Thermal oxidation behavior of WC-Co hard metal machining tool tip scraps," *J. Mater. Process. Technol.*, vol. 212, no. 6, pp. 1250–1256, 2012, doi: 10.1016/j.jmatprotec.2012.01.009.

[59]   Watt Wetmore Webb, "Oxidtion studies in metal-carbon systems" PhD Thesis, Massachusetts Institute of Technology, 1955.

[60]   S. N. Basu & V. K. Sarin, "Oxidation behavior of WC-Co," *Mater. Sci. Eng. A*, vol. 209, pp. 206–212, 1996.

[61]   Liyong Chen, Danqing Yi, Bin Wang, Huiqun Liu, & Chunping Wu, "Mechanism of the early stages of oxidation of WC-Co cemented carbides," *Corros. Sci.*, vol. 103, pp. 75–87, 2016, doi: 10.1016/j.corsci.2015.11.007.

[62]   V. B. Voitovich, V. V. Sverdel, R. F. Voitovich, & E. I. Golovko, "Oxidation of WC-Co, WC-Ni and WC-Co-Ni Hard Metals in the Temperature Range 500-800°C," *Int. J. Refract. Met. Hard*

Mater., vol. 14, no. 4, pp. 289–295, 1996, doi: 10.1016/0263-4368(96)00009-1.

[63]   W. Acchar, U. U. Gomes, W. A. Kaysser, & J. Goring, "Strength degradation of a tungsten carbide-cobalt composite at elevated temperatures," *Mater. Charact.*, vol. 43, no. 1, pp. 27–32, 1999, doi: 10.1016/S1044-5803(98)00056-4.

[64]   Randall M. German, "Consolidation Techniques," in *Comprehensive Hard Materials*, vol. 1, Elsevier Ltd, 2014, pp. 237–263.

[65]   Hermann Sicius & Hermann Sicius, *Cobaltgruppe: Elemente der neunten Nebengruppe*. 2019.

[66]   I. Konyashin, H. Hinners, B. Ries, A. Kirchner, B. Klöden, B. Kieback, R. W. N. Nilen, & D. Sidorenko, "Additive manufacturing of WC-13%Co by selective electron beam melting: Achievements and challenges," *Int. J. Refract. Met. Hard Mater.*, vol. 84, 2019, doi: 10.1016/j.ijrmhm.2019.105028.

[67]   Corson L. Cramer, Peeyush Nandwana, Richard A. Lowden, & Amy M. Elliott, "Infiltration studies of additive manufacture of WC with Co using binder jetting and pressureless melt method," *Addit. Manuf.*, vol. 28, pp. 333–343, 2019, doi: 10.1016/j.addma.2019.04.009.

[68]   Aaron D. Krawitz & Eric F. Drake, "Residual Stresses," in *Comprehensive Hard Materials*, vol. 1, Elsevier, 2014, pp. 385–404.

[69]   Aaron Krawitz & Eric Drake, "Residual stresses in cemented carbides - An overview," *Int. J. Refract. Met. Hard Mater.*, vol. 49, no. 1, pp. 27–35, 2015, doi: 10.1016/j.ijrmhm.2014.07.018.

[70]   M. F. Ashby, "A first report on deformation-mechanism maps," *Acta Metall.*, vol. 20, no. 7, pp. 887–897, 1972, doi: 10.1016/0001-6160(72)90082-X.

[71]   N. V. Novikov, V. P. Bondarenko, & V. T. Golovchan, "High-temperature mechanical properties of WC-Co hard metals (Review)," *J. Superhard Mater.*, vol. 29, no. 5, pp. 261–280, 2007, doi: 10.3103/s1063457607050012.

[72]   Kathrin Maier, Thomas Klünsner, Martin Krobath, Christian Tritremmel, Stefan Marsoner, & Christoph Czettl, "Uniaxial step loading test setup for determination of creep curves of

oxidation-sensitive high strength materials in vacuum under tensile and compressive load," *Int. J. Refract. Met. Hard Mater.*, vol. 92, no. July, p. 105327, 2020, doi: 10.1016/j.ijrmhm.2020.105327.

[73]   Jiaqi Che, Hanxiang Wang, Yanwen Zhang, Yanxin Liu, Mingchao Du, & Shaohua Ma, "Experimental and numerical studies on chip formation mechanism and working performance of the milling tool with single abrasive grain," *J. Pet. Sci. Eng.*, vol. 195, p. 107645, 2020, doi: 10.1016/j.petrol.2020.107645.

[74]   Thomas Klünsner, "Influence of Microstructure on Material Behaviour of WC-Co Hard Metals under Static and Cyclic Loading Conditions"PhD Thesis, Montanuniversität Leoben, 2011.

[75]   J. Gurland, "The measurement of grain contiguity in two-phase alloys," *Trans. AIME*, vol. 212, pp. 452–455, 1958.

[76]   B. Roebuck & E. A. Almond, "Deformation and fracture processes and the physical metallurgy of WC-Co hardmetals," *Int. Mater. Rev.*, vol. 33, no. 2, pp. 91–112, 1988.

[77]   W. Betteridge, "The properties of metallic cobalt," *Prog. Mater. Sci.*, vol. 24, no. C, pp. 51–142, 1980, doi: 10.1016/0079-6425(79)90004-5.

[78]   S. B. Luyckx, "Slip system of tungsten carbide crystals at room temperature," *Acta Metall.*, vol. 18, no. 2, pp. 233–236, 1970, doi: 10.1016/0001-6160(70)90028-3.

[79]   Alex V. Shatov, S. S. Ponomarev, & S. A. Firstov, "Hardness and Deformation of Hardmetals at Room Temperature," in *Comprehensive Hard Materials*, vol. 1, Elsevier, 2014, pp. 267–299.

[80]   R. Spiegler & H. F. Fischmeister, "Prediction of crack paths in WCCo alloys," *Acta Metall. Mater.*, vol. 40, no. 7, pp. 1653–1661, 1992, doi: 10.1016/0956-7151(92)90108-Q.

[81]   D. Mari, "Understanding the mechanical properties of hardmetals through mechanical spectroscopy," *Mater. Sci. Eng. A*, vol. 521–522, pp. 322–328, 2009, doi: 10.1016/j.msea.2008.10.064.

[82]   Yu V. Milman, S. Luyckx, V. A. Goncharuck, & J. T. Northrop, "Results from bending tests on

submicron and micron WC-Co grades at elevated temperatures," *Int. J. Refract. Met. Hard Mater.*, vol. 20, no. 1, pp. 71–79, 2002, doi: 10.1016/S0263-4368(01)00072-5.

[83]   Katharina Buss, "High Temperature Deformation Mechanisms of Cemented Carbides and Cermets, PhD Thesis"PhD Thesis, ÉCOLE POLYTECHNIQUE FÉDÉRALE DE LAUSANNE, 2004.

[84]   F. Ueda, H. Doi, F. Fujiwara, & H. Masatomi, "BEND DEFORMATION AND FRACTURE OF WC-Co ALLOYS AT ELEVATED TEMPERATURES.," *Trans Jpn Inst Met*, vol. 18, no. 3, pp. 247–256, 1977, doi: 10.2320/matertrans1960.18.247.

[85]   D. Mari, U. Marti, & P. C. Silva, "A new photolithographic technique to detect the local deformation of materials: application to WCCo composites," *Mater. Sci. Eng. A*, vol. 158, no. 2, pp. 203–206, 1992, doi: 10.1016/0921-5093(92)90009-P.

[86]   M. V. G. Petisme, M. A. Gren, & G. Wahnström, "Molecular dynamics simulation ofWC/WC grain boundary sliding resistance in WC-Co cemented carbides at high temperature," *Int. J. Refract. Met. Hard Mater.*, vol. 49, no. 1, pp. 75–80, 2015, doi: 10.1016/j.ijrmhm.2014.07.037.

[87]   Jean Lemaitre, *A Course on Damage Mechancis*, 2nd ed. Berlin Heidelberg: Springer-Verlag Berlin Heidelberg GmbH, 1996.

[88]   J. T. Smith & J. D. Wood, "Elevated temperature compressive creep behavior of tungsten carbide-cobalt alloys," *Acta Metall.*, vol. 16, no. 10, pp. 1219–1226, 1968, doi: 10.1016/0001-6160(68)90003-5.

[89]   J. L. Chaboche, K. Dang Van, & G. Cordier, "Modelization of the Strain Memory Effect on the Cyclic Hardening of 316 Stainless Steel," in *Transactions of the International Conference on Structural Mechanics in Reactor Technology*, 1979, vol. L.

[90]   J. L. Chaboche, "Time-independent constitutive theories for cyclic plasticity," *Int. J. Plast.*, vol. 2, no. 2, pp. 149–188, 1986, doi: 10.1016/0749-6419(86)90010-0.

[91]   J. L. Chaboche & D. Nouailhas, "Constitutive modeling of ratchetting effects-part I: Experimental facts and properties of the classical models," *J. Eng. Mater. Technol. Trans. ASME*, vol. 111, no. 4, pp. 384–392, 1989, doi: 10.1115/1.3226484.

[92]   Michal Kotoul, "Constitutive modeling of ratcheting of metal particulate-reinforced ceramic matrix composites," *Mater. Sci. Eng. A*, vol. 319–321, pp. 657–661, Dec. 2001, doi: 10.1016/S0921-5093(01)00983-2.

[93]   Thomas Klünsner, Stefan Marsoner, Reinhold Ebner, Reinhard Pippan, Johannes Glätzle, & Arndt Püschel, "Effect of microstructure on fatigue properties of WC-Co hard metals," *Procedia Eng.*, vol. 2, no. 1, pp. 2001–2010, 2010, doi: 10.1016/j.proeng.2010.03.215.

[94]   Luis Llanes, Marc Anglada, & Yadir Torres, "Fatigue of Cemented Carbides," in *Comprehensive Hard Materials*, vol. 1, Elsevier, 2014, pp. 345–362.

[95]   N. N. Sereda, A. K. Gerikhanov, M. S. Koval'chenko, V. A. Tsyban', & L. G. Pedanov, "Cyclic strength of hard metals," *Sov. Powder Metall. Met. Ceram.*, vol. 24, no. 9, pp. 721–724, 1985, doi: 10.1007/BF00792172.

[96]   P. R. Fry & G. G. Garrett, "Fatigue crack growth behaviour of tungsten carbide-cobalt hardmetals," *J. Mater. Sci.*, vol. 23, no. 7, pp. 2325–2338, 1988, doi: 10.1007/BF01111884.

[97]   Y. Torres, M. Anglada, & L. Llanes, "Fatigue mechanics of WC-Co cemented carbides," *Int. J. Refract. Met. Hard Mater.*, vol. 19, no. 4–6, pp. 341–348, 2001, doi: 10.1016/S0263-4368(01)00032-4.

[98]   L. Llanes, Y. Torres, & M. Anglada, "On the fatigue crack growth behavior of WC-Co cemented carbides: Kinetics description, microstructural effects and fatigue sensitivity," *Acta Mater.*, vol. 50, no. 9, pp. 2381–2393, 2002, doi: 10.1016/S1359-6454(02)00071-X.

[99]   S. Luyckx & A. Love, "The dependence of the contiguity of WC on Co content and its independence from WC grain size in WC-Co alloys," *Int. J. Refract. Met. Hard Mater.*, vol. 24, no. 1–2, pp. 75–79, 2006, doi: 10.1016/j.ijrmhm.2005.04.012.

[100]   J. M. Tarragó, E. Jiménez-Piqué, L. Schneider, D. Casellas, Y. Torres, & L. Llanes, "FIB/FESEM experimental and analytical assessment of R-curve behavior of WC-Co cemented carbides," *Mater. Sci. Eng. A*, vol. 645, pp. 142–149, 2015, doi: 10.1016/j.msea.2015.07.090.

[101]   D. Stephenson, "The effect of surface conditions on the fatigue strength of cemented carbides"PhD Thesis, Loughborough University of Technology, 1984.

[102] P. Kindermann, P. Schlund, H. G. Sockel, M. Herr, W. Heinrich, K. Görting, & U. Schleinkofer, "High-temperature fatigue of cemented carbides under cyclic loads," *Int. J. Refract. Met. Hard Mater.*, vol. 17, no. 1, pp. 55–68, 1999, doi: 10.1016/S0263-4368(99)00014-1.

[103] Heinrich Dubbel, *Dubbel*, 25th ed. Berlin: Springer Vieweg, 2018.

[104] M. G. Gee, C. Phatak, & R. Darling, "Determination of wear mechanisms by stepwise erosion and stereological analysis," in *Wear*, 2005, vol. 258, no. 1-4 SPEC. ISS., pp. 412–425, doi: 10.1016/j.wear.2004.02.013.

[105] M. G. Gee, A. Gant, & B. Roebuck, "Wear mechanisms in abrasion and erosion of WC/Co and related hardmetals," *Wear*, vol. 263, no. 1-6 SPEC. ISS., pp. 137–148, 2007, doi: 10.1016/j.wear.2006.12.046.

[106] K. Bonny, P. De Baets, J. Vleugels, S. Huang, O. Van der Biest, & B. Lauwers, "Impact of Cr3C2/VC addition on the dry sliding friction and wear response of WC-Co cemented carbides," *Wear*, vol. 267, no. 9–10, pp. 1642–1652, 2009, doi: 10.1016/j.wear.2009.06.013.

[107] K. Bonny, P. De Baets, Y. Perez, J. Vleugels, & B. Lauwers, "Friction and wear characteristics of WC-Co cemented carbides in dry reciprocating sliding contact," *Wear*, vol. 268, no. 11–12, pp. 1504–1517, 2010, doi: 10.1016/j.wear.2010.02.029.

[108] H. Engqvist, U. Beste, & N. Axén, "Influence of pH on sliding wear of WC-based materials," *Int. J. Refract. Met. Hard Mater.*, vol. 18, no. 2, pp. 103–109, 2000, doi: 10.1016/S0263-4368(00)00007-X.

[109] Eberhard Roos & Karl Maile, *Werkstoffkunde für Ingenieure*, 5th ed. Berlin, Heidelberg: Springer Berlin Heidelberg, 2015.

[110] K. Anand, C. Morrison, R. O. Scattergood, H. Conrad, J. L. Routbort, & R. Warren, "Erosion of Multiphase Materials.," in *Institute of Physics Conference Series*, Aug. 1986, no. 75, pp. 949–961.

[111] K. Anand & H. Conrad, "Microstructure and scaling effects in the damage of WC-Co alloys by single impacts of hard particles," *J. Mater. Sci.*, vol. 23, no. 8, pp. 2931–2942, 1988, doi: 10.1007/BF00547472.

[112] K. Anand & H. Conrad, "Local impact damage and erosion mechanisms in WC-6wt.%Co alloys," *Mater. Sci. Eng.*, vol. 105–106, no. PART 2, pp. 411–421, 1988, doi: 10.1016/0025-5416(88)90725-2.

[113] Robert Boker, "Die Mechanik der bleibenden Formanderung in kristallinisch aufgebauten Korpern"PhD Thesis, Technische Hochschule Aachen, 1915.

[114] Andreas W. Nemetz, Werner Daves, Thomas Klünsner, Werner Ecker, Tamara Teppernegg, Christoph Czettl, & Ivan Krajinović, "FE temperature- and residual stress prediction in milling inserts and correlation with experimentally observed damage mechanisms," *J. Mater. Process. Technol.*, vol. 256, no. November 2017, pp. 98–108, 2018, doi: 10.1016/j.jmatprotec.2018.01.039.

[115] A. W. Nemetz, W. Daves, T. Klünsner, C. Praetzas, W. Liu, T. Teppernegg, C. Czettl, F. Haas, C. Bölling, & J. Schäfer, "Experimentally validated calculation of the cutting edge temperature during dry milling of Ti6Al4V," *J. Mater. Process. Technol.*, vol. 278, no. September 2019, p. 116544, 2020, doi: 10.1016/j.jmatprotec.2019.116544.

[116] Uwe Schleinkofer, Christoph Czettl, & Claude Michotte, "Coating Applications for Cutting Tools," in *Comprehensive Hard Materials*, vol. 1, Elsevier Ltd, 2014, pp. 453–469.

[117] W. Kalss, A. Reiter, V. Derflinger, C. Gey, & J. L. Endrino, "Modern coatings in high performance cutting applications," *Int. J. Refract. Met. Hard Mater.*, vol. 24, no. 5, pp. 399–404, 2006, doi: 10.1016/j.ijrmhm.2005.11.005.

[118] C. Pfohl, A. Bulak, & K. T. Rie, "Development of titanium diboride coatings deposited by PACVD," *Surf. Coatings Technol.*, vol. 131, no. 1–3, pp. 141–146, 2000, doi: 10.1016/S0257-8972(00)00752-0.

[119] M. Berger, L. Karlsson, M. Larsson, & S. Hogmark, "Low stress TiB2 coatings with improved tribological properties," *Thin Solid Films*, vol. 401, no. 1–2, pp. 179–186, 2001, doi: 10.1016/S0040-6090(01)01481-X.

[120] R. Kullmer, C. Lugmair, A. Figueras, J. Bassas, M. Stoiber, & C. Mitterer, "Microstructure, mechanical and tribological properties of PACVD Ti(B,N) and TiB2 coatings," *Surf. Coatings Technol.*, vol. 174–175, no. 03, pp. 1229–1233, 2003, doi: 10.1016/S0257-8972(03)00532-

2.

[121] Nina Schalk, Jozef Keckes, Christoph Czettl, Manfred Burghammer, Marianne Penoy, Claude Michotte, & Christian Mitterer, "Investigation of the origin of compressive residual stress in CVD TiB2 hard coatings using synchrotron X-ray nanodiffraction," *Surf. Coatings Technol.*, vol. 258, pp. 121–126, 2014, doi: 10.1016/j.surfcoat.2014.09.050.

[122] Jihui Zhu, Houming Zhou, Bo Qin, & Zhenyu Zhao, "Design, fabrication and properties of TiB2/TiN/WC gradient ceramic tool materials," *Ceram. Int.*, vol. 46, no. 5, pp. 6497–6506, Apr. 2020, doi: 10.1016/j.ceramint.2019.11.131.

[123] C. E. MOROSANU, "Evolution of CVD Films," in *Thin Films by Chemical Vapour Deposition*, 1990, pp. 19–27.

[124] C. E. MOROSANU, "Uses of CVD Thin Films," in *Thin Films by Chemical Vapour Deposition*, 1990, pp. 465–515.

[125] Martina Gassner, Nina Schalk, Michael Tkadletz, Christoph Czettl, & Christian Mitterer, "Thermal crack network on CVD TiCN/α-Al 2 O 3 coated cemented carbide cutting tools," *Int. J. Refract. Met. Hard Mater.*, vol. 81, no. September 2018, pp. 1–6, 2019, doi: 10.1016/j.ijrmhm.2019.02.006.

[126] A. De S. Jayatilaka & K. Trustrum, "Statistical approach to brittle fracture," *J. Mater. Sci.*, vol. 12, no. 7, pp. 1426–1430, 1977, doi: 10.1007/BF00540858.

[127] Fritz Klocke, Alexander Krämer, Hubertus Sangermann, & Dieter Lung, "Thermo-mechanical tool load during high performance cutting of hard-to-cut materials," in *Procedia CIRP*, 2012, vol. 1, no. 1, pp. 295–300, doi: 10.1016/j.procir.2012.04.053.

[128] Stefan Hoppe, "Experimental and numerical analysis of chip formation in metal cutting"PhD Thesis, Technische Hochschule Aachen, 2003.

[129] Peng Wang, Hongjian Ni, Xueying Wang, & Ruihe Wang, "Modelling the load transfer and tool surface for friction reduction drilling by vibrating drill-string," *J. Pet. Sci. Eng.*, vol. 164, pp. 333–343, 2018, doi: 10.1016/j.petrol.2018.01.078.

[130] Meng Li, Shuli Hu, Kanhua Su, Lifu Wan, Xiaole Guo, Huiqun He, & Weiqing Chen,

"Orientation load prediction method based on randomness/stochasticity of multi-source parameters in coiled tubing drilling," *J. Pet. Sci. Eng.*, vol. 189, no. January, p. 107017, 2020, doi: 10.1016/j.petrol.2020.107017.

[131] B. Denkena, A. Lucas, & E. Bassett, "Effects of the cutting edge microgeometry on tool wear and its thermo-mechanical load," *CIRP Ann. - Manuf. Technol.*, vol. 60, no. 1, pp. 73–76, 2011, doi: 10.1016/j.cirp.2011.03.098.

[132] Andreas W. Nemetz, "Internal communication: FE simulation of normal and tangential loads in the substrate of a milling tool during machining.," 2017.

[133] Lukas Walch, "Test setup for analyzing damaging of coated WC-Co hardmetal substrates at elevated temperatures Bachelor thesis"PhD Thesis, University of Leoben, 2019.

[134] K. D. Bouzakis, A. Asimakopoulos, G. Skordaris, J. Anastopoulos, E. Pavlidou, & G. Erkens, "a Novel Method To Characterize Cohesion and Adhesion Properties of Coatings By Means of the Inclined Impact Test," *Proc. 16th Int. Plansee Sem.*, vol. 27, no. 2, pp. 1221–1234, 2005.

[135] K. D. Bouzakis, A. Asimakopoulos, G. Skordaris, E. Pavlidou, & G. Erkens, "The inclined impact test: A novel method for the quantification of the adhesion properties of PVD films," *Wear*, vol. 262, no. 11–12, pp. 1471–1478, 2007, doi: 10.1016/j.wear.2007.01.027.

[136] Ying Chen & Xueyuan Nie, "Study on fatigue and wear behaviors of a TiN coating using an inclined impact-sliding test," *Surf. Coatings Technol.*, vol. 206, no. 7, pp. 1977–1982, 2011, doi: 10.1016/j.surfcoat.2011.09.032.

[137] Constantin Tiganesteanu, Lucian Capitanu, & Liliana Laura Badita, "Characterisation of cohesion and adhesion of thin coatings by cyclic inclined impact test," *Rom. Rev. Precis. Mech. Opt. Mechatronics*, vol. 2015, no. 48, pp. 237–245, 2015.

[138] Lucian Capitanu, Virgil Florescu, Constantin Tiganesteanu, & Liliana-laura Badita, "ADHESION OF THE COATINGS WITH THIN LAYERS TESTING BY THE INCLINED CYCLIC IMPACT," *Acta Electrotech.*, vol. 58, no. 1–2, pp. 15–25, 2017.

[139] G. Skordaris, K. D. Bouzakis, P. Charalampous, T. Kotsanis, E. Bouzakis, & R. Bejjani, "Bias voltage effect on the mechanical properties, adhesion and milling performance of PVD

films on cemented carbide inserts," *Wear*, vol. 404–405, no. November 2017, pp. 50–61, 2018, doi: 10.1016/j.wear.2018.03.001.

[140] Dassault Systemes, "Abaqus Unified FEA," 2013. https://www.3ds.com/de/produkte-und-services/simulia/produkte/abaqus/.

[141] Du Hong, Yaran Niu, Hong Li, Xin Zhong, Wenhua Tu, Xuebin Zheng, & Jinliang Sun, "Comparison of microstructure and tribological properties of plasma-sprayed TiN, TiC and TiB2 coatings," *Surf. Coatings Technol.*, vol. 374, no. December 2018, pp. 181–188, 2019, doi: 10.1016/j.surfcoat.2019.05.071.

[142] Thomas Kaltenbrunner, "Internal communication: Simulative and experimental study of the load situation and substrate degradation in coated hard metal cutting inserts.," 2019.

[143] "Internal communications with Ceratizit S.A.," 2020.

[144] Stephan Kabelac, Matthias Kind, Holger Martin, Dieter Mewes, Karlheinz Schaber, & Peter Stephan, *VDI-Wärmeatlas, 11. Auflage*. 2013.

[145] Valery Rudnev, Don Loveless, & Raymond L. Cook, *Handbook of Induction Heating, Second Edition*. 2018.

[146] Atsushi Nishiyama & Ryuichi Ishida, "The Purity of the Cobalt Phase in Cemented Carbide Hard Alloys," *Trans. Japan Inst. Met.*, vol. 3, no. 4, pp. 185–189, 1962, doi: 10.2320/matertrans1960.3.185.

[147] Radim Kocich, "Design and optimization of induction heating for tungsten heavy alloy prior to rotary swaging," *Int. J. Refract. Met. Hard Mater.*, vol. 93, no. July, p. 105353, 2020, doi: 10.1016/j.ijrmhm.2020.105353.

[148] Enrico Gnecco, Ernst Meyer, Enrico Gnecco, & Ernst Meyer, "Plastic contacts," *Elem. Frict. Theory Nanotribology*, vol. 3, pp. 115–132, 2015, doi: 10.1017/cbo9780511795039.013.

[149] Edward Dintwa, Engelbert Tijskens, & Herman Ramon, "On the accuracy of the Hertz model to describe the normal contact of soft elastic spheres," *Granul. Matter*, vol. 10, no. 3, pp. 209–221, 2008, doi: 10.1007/s10035-007-0078-7.

[150] Filmetrics, "Profilometer and 3D Optical Profiler - Filmetrics."

https://www.filmetrics.com/profilometers/profilm3d.

[151] Zhigang Zak Fang, "Correlation of transverse rupture strength of WC-Co with hardness," *Int. J. Refract. Met. Hard Mater.*, vol. 23, no. 2, pp. 119–127, 2005, doi: 10.1016/j.ijrmhm.2004.11.005.

[152] B. Roebuck, K. P. Mingard, H. Jones, & E. G. Bennett, "Aspects of the metrology of contiguity measurements in WC based hard materials," *Int. J. Refract. Met. Hard Mater.*, vol. 62, pp. 161–169, 2017, doi: 10.1016/j.ijrmhm.2016.05.011.

[153] S. Ishihara, T. Goshima, Y. Yoshimoto, T. Sabu, & A. J. McEvily, "Influence of the stress ratio on fatigue crack growth in a cermet," *J. Mater. Sci.*, vol. 35, no. 22, pp. 5661–5665, 2000, doi: 10.1023/A:1004846205548.

[154] I. Konyashin, A. Sologubenko, T. Weirich, & B. Ries, "Complexion at WC-Co grain boundaries of cemented carbides," *Mater. Lett.*, vol. 187, pp. 7–10, 2017, doi: 10.1016/j.matlet.2016.10.055.

[155] Gustaf Östberg, Katharina Buss, Mikael Christensen, Susanne Norgren, Hans Olof Andrén, Daniele Mari, Göran Wahnström, & Ingrid Reineck, "Mechanisms of plastic deformation of WC-Co and Ti(C, N)-WC-Co," *Int. J. Refract. Met. Hard Mater.*, vol. 24, no. 1–2, pp. 135–144, 2006, doi: 10.1016/j.ijrmhm.2005.04.009.

[156] B. Paul, R. Kapoor, J. K. Chakravartty, A. C. Bidaye, I. G. Sharma, & A. K. Suri, "Hot working characteristics of cobalt in the temperature range 600-950 °C," *Scr. Mater.*, vol. 60, no. 2, pp. 104–107, 2009, doi: 10.1016/j.scriptamat.2008.09.012.

[157] Fjodor Sergejev, Irina Preis, Jakob Kübarsepp, & Maksim Antonov, "Correlation between surface fatigue and microstructural defects of cemented carbides," *Wear*, vol. 264, no. 9–10, pp. 770–774, 2008, doi: 10.1016/j.wear.2007.02.024.

[158] J. A. M. Ferreira, M. A. Pin. Amaral, F. V. Antunes, & J. D. M. Costa, "A study on the mechanical behaviour of WC/Co hardmetals," *Int. J. Refract. Met. Hard Mater.*, vol. 27, no. 1, pp. 1–8, 2009, doi: 10.1016/j.ijrmhm.2008.01.013.

[159] W. K. Kubin, M. Pletz, W. Daves, & S. Scheriau, "A new roughness parameter to evaluate the near-surface deformation in dry rolling/sliding contact," *Tribol. Int.*, vol. 67, pp. 132–

139, 2013, doi: 10.1016/j.triboint.2013.07.007.

[160] J. Yang, M. Odén, M. P. Johansson-Jõesaar, & L. Llanes, "Grinding effects on surface integrity and mechanical strength of WC-Co cemented carbides," in *Procedia CIRP*, 2014, vol. 13, pp. 257–263, doi: 10.1016/j.procir.2014.04.044.

[161] J. Yang, J. J. Roa, M. Schwind, M. Odén, M. P. Johansson-Jõesaar, & L. Llanes, "Grinding-induced metallurgical alterations in the binder phase of WC-Co cemented carbides," *Mater. Charact.*, vol. 134, no. August, pp. 302–310, 2017, doi: 10.1016/j.matchar.2017.11.004.

[162] J. Yang, F. García Marro, T. Trifonov, M. Odén, M. P. Johansson-Jõesaar, & L. Llanes, "Contact damage resistance of TiN-coated hardmetals: Beneficial effects associated with substrate grinding," *Surf. Coatings Technol.*, vol. 275, pp. 133–141, 2015, doi: 10.1016/j.surfcoat.2015.05.028.

[163] J. Yang, J. J. Roa, M. Odén, M. P. Johansson-Jõesaar, J. Esteve, & L. Llanes, "Substrate surface finish effects on scratch resistance and failure mechanisms of TiN-coated hardmetals," *Surf. Coatings Technol.*, vol. 265, pp. 174–184, 2015, doi: 10.1016/j.surfcoat.2015.01.038.

[164] Cyril Stanley Smith & Lester Guttman, "Measurement of Internal Boundaries in Three-Dimensional Structures By Random Sectioning," *J. Met.*, vol. 5, no. 1, pp. 81–87, 1953, doi: 10.1007/bf03397456.

List of Figures

Appendix A

The constructional drawings used to manufacture the components for the *BIC* test setup (i.e. indenter, sample holder and sample) are shown. They were provided by the Ceratizit Austria GmbH [143] and used for manufacture.

First, the indenter, referred to as indenterstamp in the constructional drawing, is attached. Second, the sample can be found. A 0.7 mm post-processing reduction on the cone-sided end necessary for improved compatibility with the Zeiss AURIGA-CrossBeam work station is not included. After manufacture, the specimen is coated with a TiN-TiB$_2$ multilayer coating using a *CVD* process. Third, the sample holder is also included.

Sorte: CTD12D

Detail A

Indenterstamp

Schleifzeichnung

Detail A

Sorte: CTH594 wird beigestellt

Pos	Stk.	Vertriebstext		Name		SAP Material	Kommentar	Teil
Konstruiert	kuhnmi		Dat. 04.02.2020	V=	- cm³	m= - kg	SAP	
Geprüft			Dat.	A=	- mm²		Material	
Geänd.	von kuhnmi		Dat. 04.02.2020					
	Kurztext							
Kunde						Sample		
Kunden- Nr.						Schleifzeichnung		

Oberfläche		Dok	Zeichnung - Änderung - Blatt
	0.3 / 0.8 /	F05	50101108-00-S2
Allgemein Toleranz ISO 2768 m K		Einheit mm	Maßst. 2:1 Format A4

CERATIZIT GROUP

Detail B
10040309

∅ 4.25

60°

∅ 2

∅ 20 +0 −0,02

B

0.5 x 45°

0.8

80 ±0.05

A

0.5 x 45°

A

Detail A

0.5 x 45°

(5)

0.8

∅ 5 E8 (+0.038 +0.02)

0.02 A

min,3 tief

Sorte: CTS12D

Pos	Stk.	Vertriebstext		Name		SAP Material	Kommentar	Teil
Konstruiert	kuhnmi		Dat. 04.02.2020	V=	- cm³	m=	- kg	SAP
Geprüft			Dat.	A=	- mm²			Material
Geänd.	von kuhnmi		Dat. 04.02.2020					
	Kurztext							
Kunde					Sampleholder			
Kunden- Nr.					Schleifzeichnung			

Oberfläche

√ (0.8/▽)

CERATIZIT GROUP

Dok	Zeichnung - Änderung - Blatt
F05	50101116-00-S3
Einheit mm	Maßst. 1:1	Format A4

Allgemein Toleranz ISO 2768 m K

Appendix B

In the following, the *SEM* micrographs in *SE* contrast mode used for defect marking are shown, grouped by specimen and ordered in matrices. Progressive load cycle numbers correlate with matrix rows; higher load cycle numbers are placed lower. The leftmost column features a micrograph showing the inner-fringe position *P3*. Rightmost is the outer-fringe position *P2* and in the middle the central position *P1*. Where there was no *FIB*-cut (e.g. at *P3* for load cycles numbers < 850) the space was left grey. *NDs* are marked with green circles, *MDs* with red circles with an attached line and *Ds* with light blue double circles. The horizontal lines mark a 2 and 4 μm distance to the substrate-coating interface (i.e. depth). Occasionally, visible vertical lines measure 2 μm and were used as a visual aid signifying a depth of 2 μm.
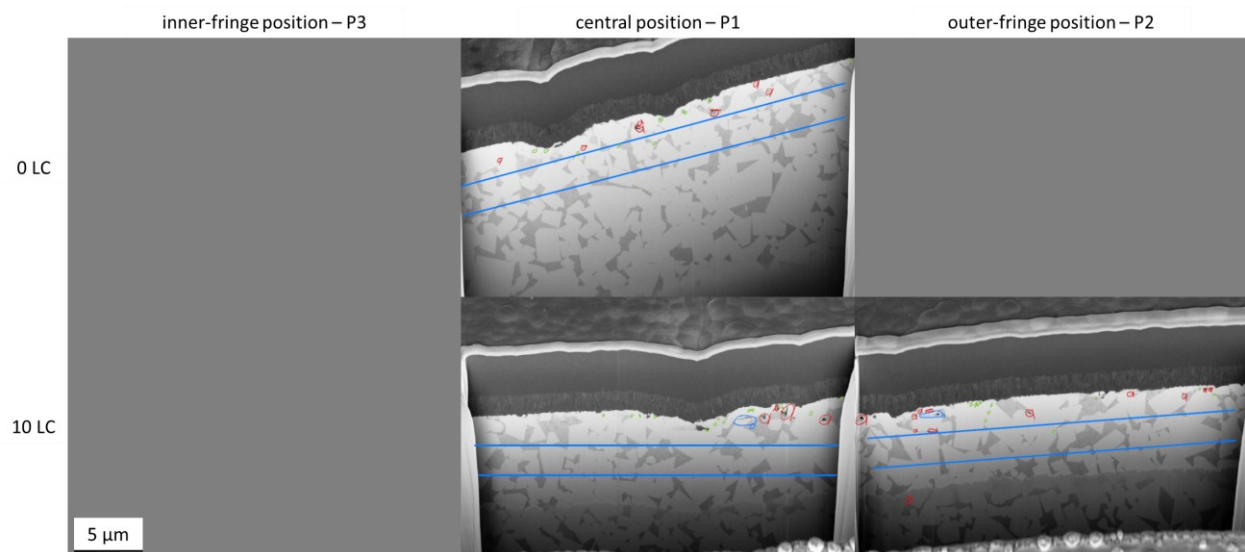
Figure 24: This matrix shows the SEM-*micrographs for the specimen* Dβ04. *The initial state of the microstructure at 0 load cycles is attributed to* P1; *since no load had yet been applied, the microstructure was assumed as identical for the other positions.*
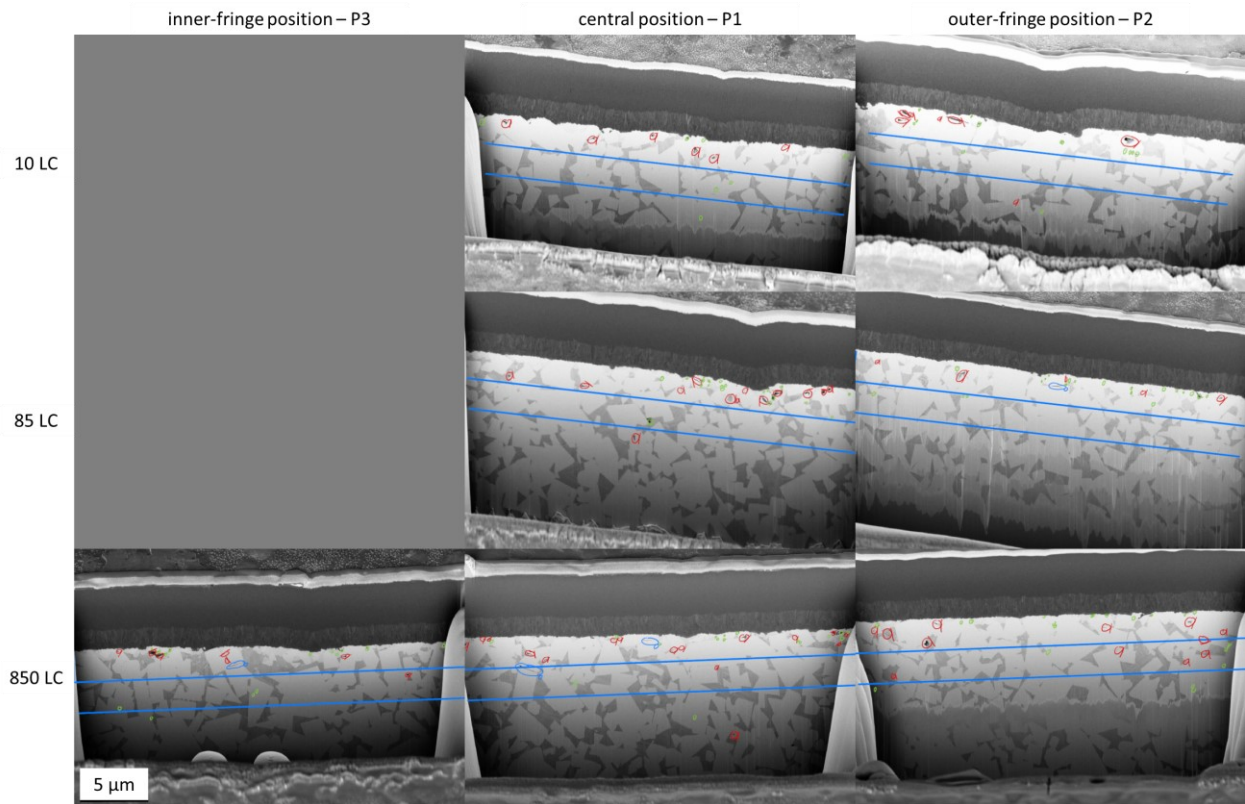
Figure 25: Here, the SEM-micrographs for specimen Dβ01 are shown. This specimen was also used for temperature calibration and saw elevated temperatures and a constant load of ~500 N for several hours before first testing. Direct comparison with other specimen (i.e. Dβ04 and Dβ03) at identical load cycles showed no significant microstructural alteration not attributable to the BIC test.
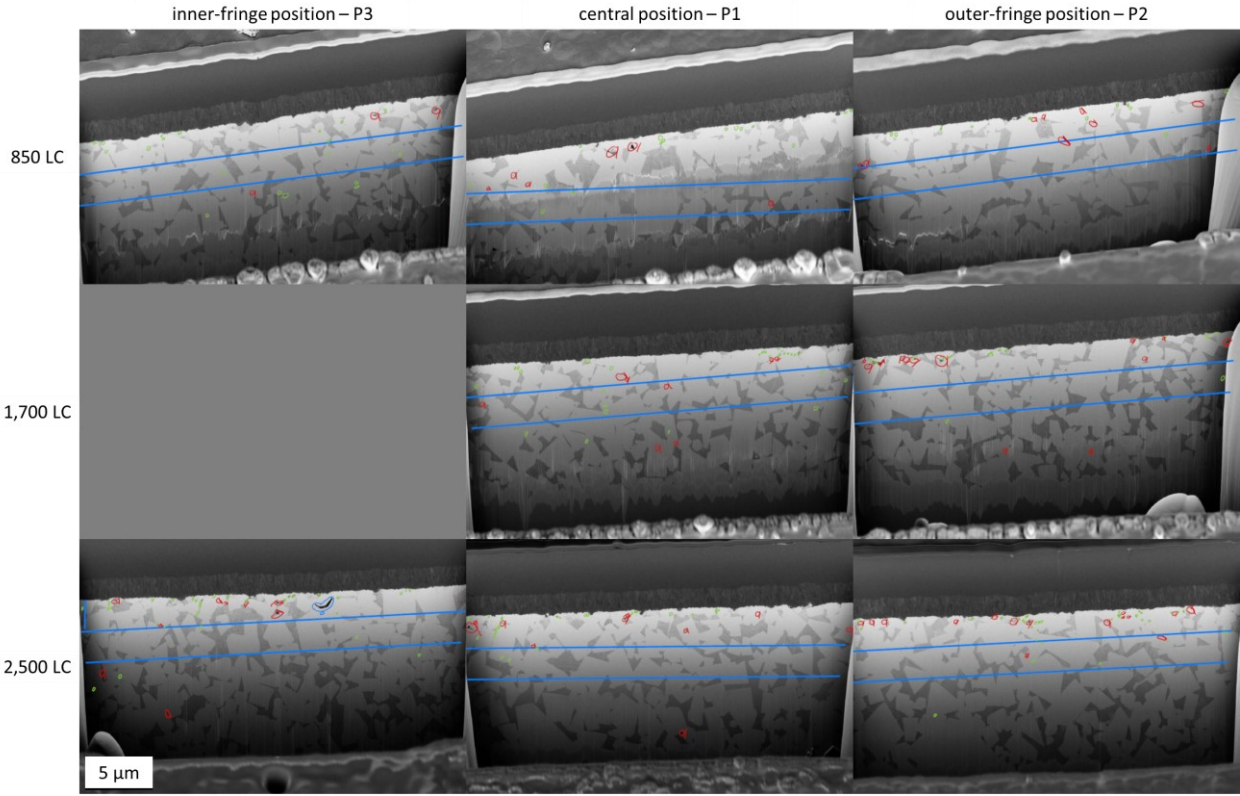
Figure 26: With specimen DꞵO3 the change from higher defect counts at P1 to P2 was observable. Here shown are the micrographs for all FIB-cut used in this work.
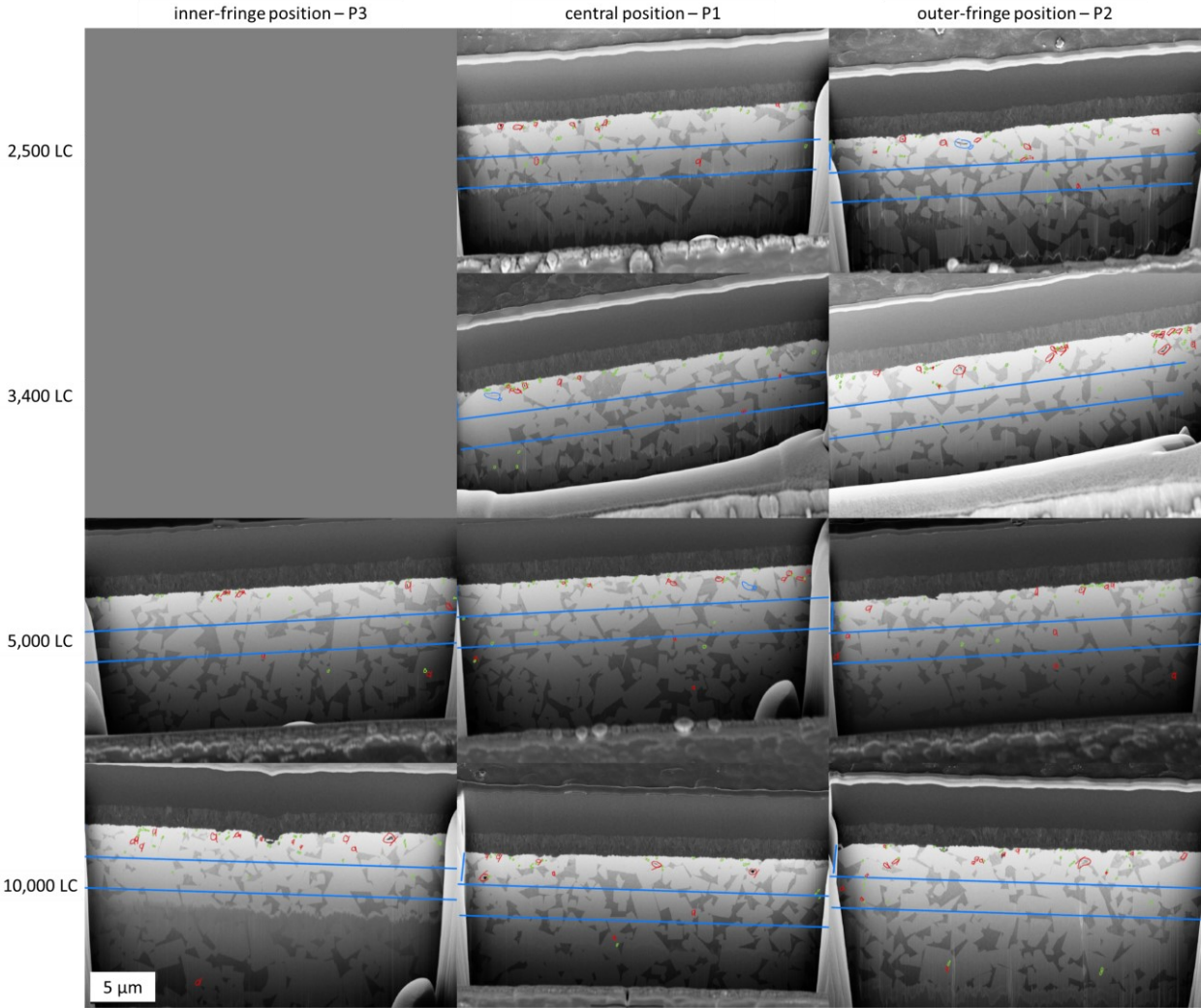
Figure 27: The highest load cycles numbers were applied to specimen Dβ02. *The particular trends at higher load cycles were all observable in this specimen.*

Appendix C

The here presented tables show the results of the defect count with added categorization by defect distance from substrate-coating interface (i.e. depth) and *MD* shape type. Additional information is conveyed via formatting. Rows with a light grey background signify a local microstructural deviation from the measured norm. Bold letters mark mean free paths of Co that are significantly higher than specimen average. Those that are significantly lower are marked in cursive (see Appendix E). Where a contiguity value significantly lower than specimen average was measured letters are underlined (see Appendix D).

Table 3: This table shows the total defect counts for each FIB-cut, categorized by size (NDs: $\emptyset_{max}<$ 0.1 µm; MDs: 0.1< $\emptyset_{max}$ <1µm; Ds: $\emptyset_{max}$ >1 µm), by position and by load cycle count after which the FIB-cut was placed. The results for the virgin state (0 load cycle) were used for all positions.

Load cycles	Specimen	P1			P2			P3		
		NDs	MDs	Ds	NDs	MDs	Ds	NDs	MDs	Ds
0	Dβ04-0°	**10**	**7**	**-**	**10**	**7**	**-**	**10**	**7**	**-**
10	Dβ04-60°	*17*	*4*	*1*	<u>13</u>	<u>12</u>	<u>0</u>	-	-	-
10	Dβ01-0°	8	6	0	13	7	0	-	-	-
85	Dβ01-60°	21	13	-	*21*	*5*	*1*	-	-	-
850	Dβ01-120°	<u>16</u>	<u>16</u>	<u>2</u>	21	12	0	14	7	1
850	Dβ03-0°	14	8	0	16	6	0	21	3	0
1700	Dβ03-60°	*29*	*7*	*0*	29	14	0	-	-	-
2500	Dβ03-120°	<u>26</u>	<u>11</u>	<u>0</u>	**36**	**15**	**0**	*32*	*9*	*1*
2500	Dβ02-0°	28	9	0	34	10	1	0	0	0
3400	Dβ02-60°	31	8	1	49	18	0	0	0	0
5000	Dβ02-120°	**32**	**12**	**1**	30	10	0	*30*	*9*	*0*
10000	Dβ02-180°	28	9	0	*36*	*16*	*0*	*39*	*14*	*0*

Table 4: Here the absolute counts for each shape type observed with microdefects (MDs) are shown. The formatting conveys information as defined at the beginning of this chapter.

Load cycles	Specimen	P1			P2			P3		
		TI	TII	TIII	TI	TII	TIII	TI	TII	TIII
0	Dβ04-0°	**5**	**2**	**-**	**5**	**2**	**-**	**5**	**2**	**-**
10	Dβ04-60°	*0*	*2*	*2*	*7*	*4*	*1*	-	-	-
10	Dβ01-0°	1	3	2	6	1	0	-	-	-
85	Dβ01-60°	6	6	1	*2*	*2*	*1*	-	-	-
850	Dβ01-120°	<u>7</u>	<u>8</u>	<u>1</u>	5	7	0	2	4	1
850	Dβ03-0°	1	5	0	6	1	1	0	2	1
1700	Dβ03-60°	*3*	*4*	*0*	8	4	2	-	-	-
2500	Dβ03-120°	<u>6</u>	<u>4</u>	<u>1</u>	**11**	**4**	**0**	*5*	*3*	*1*
2500	Dβ02-0°	5	3	1	5	3	2	-	-	-
3400	Dβ02-60°	5	3	0	4	12	2	-	-	-
5000	Dβ02-120°	**4**	**7**	**1**	3	6	1	5	4	0
10000	Dβ02-180°	3	6	0	*7*	*9*	*0*	8	6	0

Table 5: This table shows the absolute count of defects (categorized by $\varnothing_{max}$) for the central position P1. Additionally, the defects are distinguished by their location (i.e. distance to the substrate-coating interface), referred to as depth.

Load cycles	Specimen	central position P1								
		Depth <2 µm			2 µm < Depth <4 µm			Depth > 4 µm		
		NDs	MDs	Ds	NDs	MDs	Ds	NDs	MDs	Ds
0	Dβ04-0°	**8**	**7**	**0**	**2**	**0**	**0**	**0**	**0**	**0**
10	Dβ04-60°	*17*	*4*	*1*	<u>0</u>	<u>0</u>	<u>0</u>	0	0	0
10	Dβ01-0°	5	6	0	2	0	0	1	0	0
85	Dβ01-60°	20	12	0	*1*	*0*	*0*	0	1	0
850	Dβ01-120°	<u>14</u>	<u>14</u>	<u>1</u>	1	1	1	1	1	0
850	Dβ03-0°	14	5	0	2	1	0	0	0	0
1700	Dβ03-60°	*19*	*3*	*0*	6	2	0	4	2	0
2500	Dβ03-120°	<u>23</u>	<u>10</u>	<u>0</u>	**3**	**0**	**0**	*0*	*1*	
2500	Dβ02-0°	24	7	0	4	2	0	0	0	0
3400	Dβ02-60°	28	7	1	0	1	0	3	0	0
5000	Dβ02-120°	**26**	**9**	**1**	4	0	0	*3*	*2*	*0*
10000	Dβ02-180°	26	7	0	*1*	*1*	*0*	1	1	0

Table 6: This table shows the absolute count of defects for the outer-fringe position P2 *with the same categorization methods as used previously in* Table 5*.*

Load cycles	Specimen	outer-fringe position P2								
		Depth <2 µm			2 µm < Depth <4 µm			Depth > 4 µm		
		NDs	MDs	Ds	NDs	MDs	Ds	NDs	MDs	Ds
0	Dβ04-0°	**8**	**7**	**0**	**2**	**0**	**0**	**0**	**0**	**0**
10	Dβ04-60°	*13*	*11*	*1*	*-*	*-*	*-*	-		-
10	Dβ01-0°	11	6		1			1	1	
85	Dβ01-60°	18	5	1	*3*					
850	Dβ01-120°	13	7	0	5	5	0	3		
850	Dβ03-0°	13	6	0	1	2	0			
1700	Dβ03-60°	*27*	*12*	*0*	1	0	0	1	2	
2500	Dβ03-120°	29	13	0	**6**	**2**	**0**	*1*		
2500	Dβ02-0°	30	9	0	2	1	0	2		
3400	Dβ02-60°	45	18	0	4	0	0			
5000	Dβ02-120°	**27**	**5**	**0**	3	3	0	*0*	*2*	*0*
10000	Dβ02-180°	27	13	0	*5*	*2*	*0*	*4*	*1*	*0*

Table 7: This table shows the absolute count of defects for the inner-fringe position P3 *with the same categorization methods as used previously in* Table 5*.*

Load cycles	Specimen	inner-fringe position P3								
		Depth <2 µm			2 µm < Depth <4 µm			Depth > 4 µm		
		NDs	MDs	Ds	NDs	MDs	Ds	NDs	MDs	Ds
0	Dβ04-0°	**8**	**7**	**0**	**2**	**0**	**0**	**0**	**0**	**0**
10	Dβ04-60°	-	-	-	*-*	*-*	*-*	-	-	-
10	Dβ01-0°	-	-	-	-	-	-	-	-	-
85	Dβ01-60°	-	-	-	-	-	-		-	-
850	Dβ01-120°	10	6	1	3	1	0	1		
850	Dβ03-0°	12	2	0	4	0	0	5	1	0
1700	Dβ03-60°	-	-	-	-	-	-	-	-	-
2500	Dβ03-120°	26	9	1	**3**	**0**	**0**	*3*	*2*	
2500	Dβ02-0°	-	-	-	-	-	-	-	-	-
3400	Dβ02-60°	-	-	-	-	-	-	-	-	-
5000	Dβ02-120°	**27**	**7**	**0**	1	0	0	*2*	*2*	*0*
10000	Dβ02-180°	36	13	0	*3*	*0*	*0*	*0*	*1*	*0*

Appendix D

Contiguity has already been linked to the mechanical properties and consequently to failure and fatigue behavior of WC-Co hard metals [28, pp. 107–110], [75]. In general, the contiguity parameter C_{WC} is defined as the result of *Equation D.1*, where $S_{WC/WC}$ and $S_{WC/Co}$ denote the grain boundary area of *WC/WC* and *WC/Co* interface areas respectively [28, pp. 107–110], [152].

$$C_{WC} = \frac{2S_{WC/WC}}{2S_{WC/WC} + S_{WC/Co}}$$
(D.1)

A simple metallographic approach was e.g. proposed by *Smith and Guttman* in [164], states that the numerical fraction of internal boundaries in respect to the total number of boundaries in three dimensional structures can be calculated by measuring plane sections. In the case of C_{WC} calculation, this can be achieved by substituting the previously mentioned grain boundary and interface areas with the number of intersections of a straight line with grain boundaries and interfaces in a plane section. This leads to *Equation D.2*, where $N_{WC/WC}$ and $N_{WC/Co}$ denote the line intersections with *WC/WC* grain boundaries and *WC/Co* interfaces respectively [28, pp. 107–110], [164].

$$C_{WC} = \frac{2N_{WC/WC}}{2N_{WC/WC} + N_{WC/Co}}$$
(D.2)

Adhering to the recommendations presented by *Roebuck et al.* in [152], *SEM* micrographs in *EBS* contrast mode were used as basis for contiguity measurement; the proceeding was as follows: For each *FIB* cut one investigated position was randomly chosen for contiguity measurement. For each of these positions, three lines at 1 to 3 µm, 3 to 5 µm and 5 to 7 µm below the coating-substrate interface were drawn parallel to the same; measurements at the initial microstructure, i.e. 0 load cycles, were offset by 0.5 µm to shallower depths. The visible intersections were counted by one person. The average of the contiguity values for the three lines was then calculated as the valid C_{WC} (see Appendix D). The results are shown in Figure 28 *(a-b)*
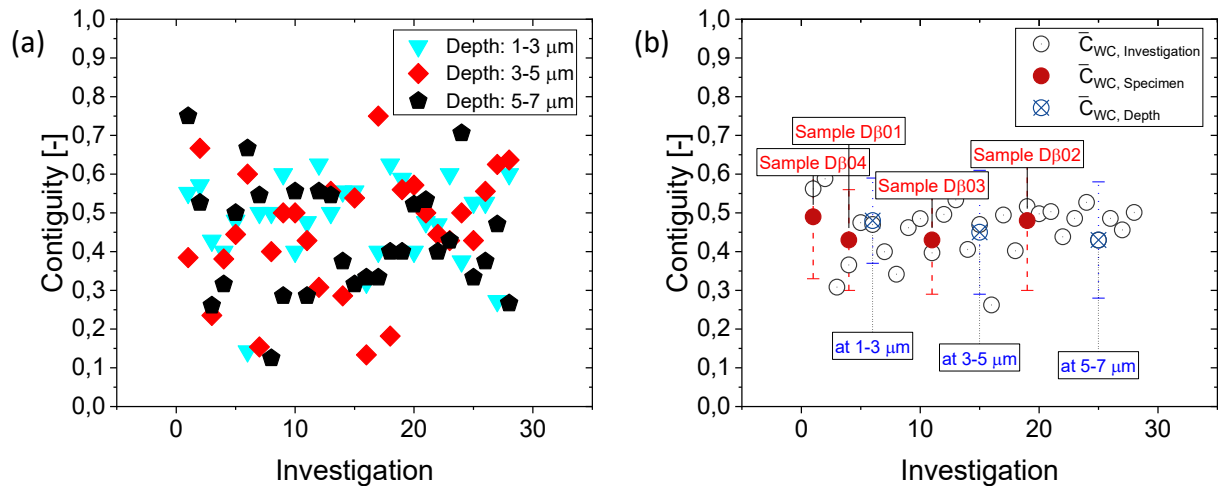
Figure 28: Measured contiguity values and averages by FIB-cut, specimen and depth are shown. (a) shows all data points with three measurements for each FIB-cut. Each measurement was conducted at a specified depth: Either at 1-3 µm, at 3-5 µm or 5-7 µm. In (b) the average contiguity values for every investigation, every specimen and every depth are shown, including their standard deviations.

Considering Figure 28 *(a)* the measured C_{WC} values exhibit great scatter and are distributed across a spectrum ranging from 0.10 to 0.80 (see Appendix F). This however is in good agreement with previous measurements of contiguity in WC-Co hard metals by other authors [99], [152]. The averaged values ($\bar{C}_{WC}$) shown in Figure 28 *(b)* are scattered over a more narrow spectrum from 0.30 to 0.60; the average contiguity values for the specimen are 0.49 for sample *Dβ04*, 0.43 for sample *Dβ01* and *Dβ03* and 0.48 for sample *Dβ02*. These values are also satisfactorily similar to those reported in literature for WC-Co hard metals with a binder phase content of about 12 wt.% [99], [152]. With the average values for every measured depth – not distinguishing individual specimens – this does not change; the values are quite similar in both mean value and standard deviation (*Std*).

Appendix E

Early in the current work, the mean free path (l_{Co}) was mentioned as having been linked to the fatigue behavior of WC-Co hard metals [6], [98]. Consequently, l_{Co} was measured by averaging the lengths of linear intercepts of the binder phase along parallel lines in planer sections in *SEM* micrographs [28, p. 107]. Otherwise, the employed proceeding is identical to the one described above for obtaining the C_{WC} values (see Appendix D). The mean free path values were calculated as shown in *Equation E.1*, with the sum of the Co phase intercept lengths (th_{Co}) in µm divided by the number of Co intercepts (N_{Co}) [28, p. 107]. The results for the mean free binder path values of Co are shown in *Figure 29 (a-b)*.

$$l_{Co} = \frac{\sum th_{Co}}{N_{Co}} \tag{E.1}$$
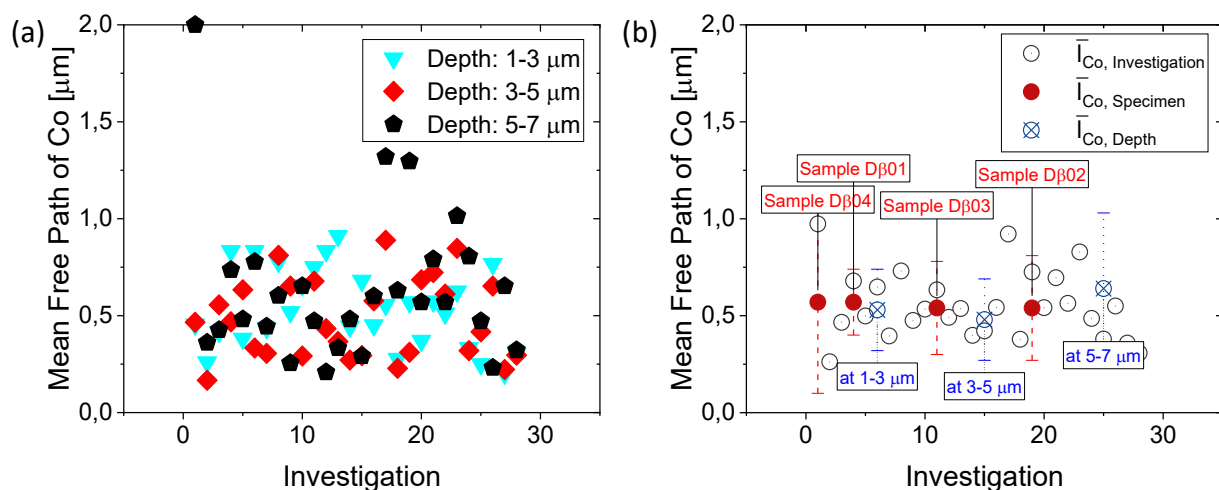
Figure 29: Measured values for the mean free path of the binder phase and averages by FIB-cut, specimen and depth are shown. (a) All data points with three measurements for each FIB-cut are shown. Each measurement was conducted at a specified depth: Either at 1-3 µm, at 3-5 µm or 5-7 µm. (b) The average mean free path values for the Co binder phase for every investigation, every specimen and every depth are shown with the standard deviation displayed for the latter two.

In Figure 29 *(a)* all measured $\overline{l}_{Co}$ values are shown; excepting three outliers they range from ~0.25 to 1.00 µm. The average mean free path values for each investigation displayed in *Figure 29-b* show a similar range. For the specimen average values of 0.57 µm for samples *Dβ04* and *Dβ01* as well as 0.54 µm for samples *Dβ03* and *Dβ02* were calculated (see Appendix F). They are

included in *Figure 29 (b)* with their respective standard deviations. The measured values, both individual and averaged are in good agreement with results reported in literature [9], [99], [151]. All obtained values for contiguity and mean free path of the binder phase are included in Appendix F.

Appendix F
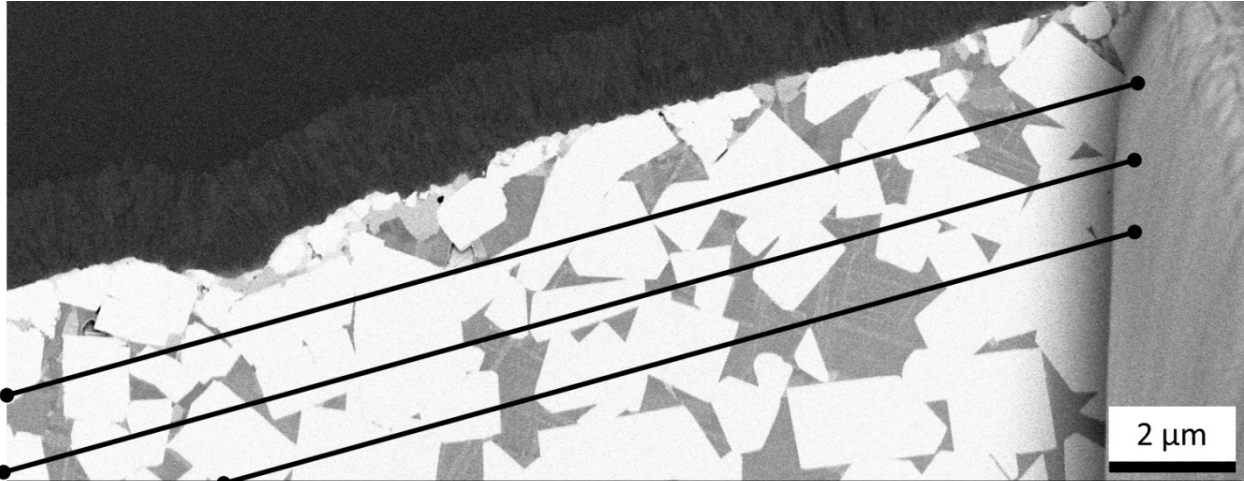
Figure 30: The SEM micrograph used for measuring contiguity and mean free path of Co, shown in the plots as investigation 1.
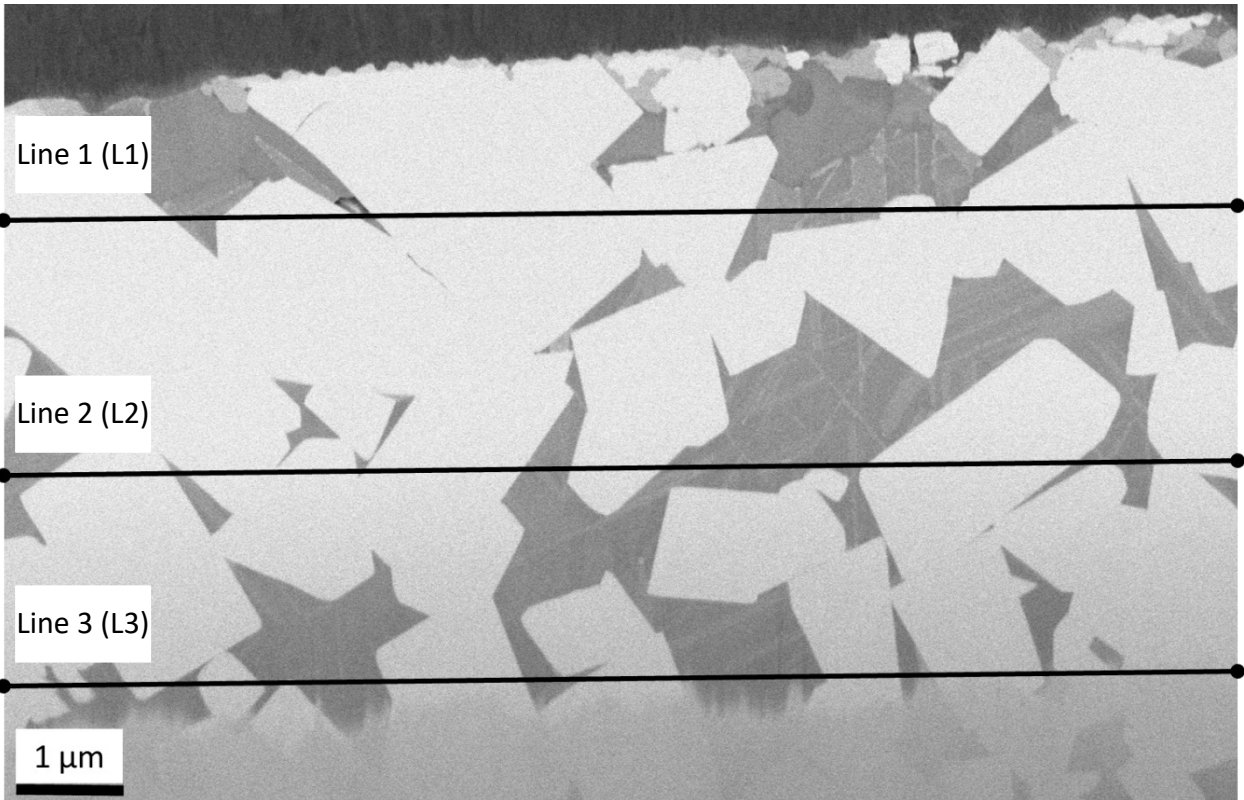
Figure 31: An exemplary SEM micrograph as used for all subsequent measurements.

Table 8: All measured values used for subsequent calculation of contiguity and mean free path of Co values are included in this table.

Nr.	Sample	$N_{WC/WC}$			$N_{WC/Co}$			th_{Co}			N_{Co}		
-	-	L1	L2	L3	L1	L2	L3	L1	L2	L3	L1	L2	L3
		-	-	-	-	-	-	cm	cm	cm	-	-	-
1	Dβ04-0°	8	5	6	13	16	4	2.5	4.1	4.4	5	8	2
2	Dβ04-60°	4	6	5	6	6	9	1.4	1.2	2.6	3	4	4
3	Dβ04-60°	3	2	3	8	13	17	3	6	6.9	4	6	9
4	Dβ01-0°	3	4	3	9	13	13	6	5.9	5.3	4	7	4
5	Dβ01-0°	6	4	3	13	10	6	4.8	5.7	2.6	7	5	3
6	Dβ01-60°	1	3	5	12	4	5	9	1.2	4.2	6	2	3
7	Dβ01-60°	7	1	6	14	11	10	5.5	3.3	5.6	7	6	7
8	Dβ01-120°	3	3	1	6	9	14	2.8	7.3	7.6	2	5	7
9	Dβ01-120°	6	3	2	8	6	10	2.8	4.7	2.3	3	4	5
10	Dβ01-120°	4	5	5	12	10	8	7.1	2.1	4.7	6	4	4
11	Dβ03-0°	5	3	2	11	8	10	5.4	6.1	5.1	4	5	6
12	Dβ03-0°	5	2	5	6	9	8	4.5	3.9	1.5	3	5	4
13	Dβ03-0°	4	5	6	8	8	10	8.2	3.3	3	5	5	5
14	Dβ03-60°	5	3	3	8	15	10	3.2	3.9	5.2	4	8	6
15	Dβ03-60°	5	7	3	8	12	13	4.9	3.7	4.2	4	7	8
16	Dβ03-120°	4	1	3	17	13	12	7.3	8.3	10.8	9	8	10
17	Dβ03-120°	4	6	2	12	4	8	5	3.2	9.5	5	2	4
18	Dβ03-120°	5	2	4	6	18	12	1.5	3.7	6.8	3	9	6
19	Dβ02-0°	5	7	2	7	11	6	4.1	2.8	7	4	5	3
20	Dβ02-0°	4	4	6	12	6	11	4	3.7	4.1	6	3	4
21	Dβ02-60°	5	3	4	11	6	7	6.2	5.2	5.7	6	4	4
22	Dβ02-60°	4	4	4	9	10	12	4.6	5.5	4.1	5	5	4
23	Dβ02-120°	6	3	3	8	8	8	4.5	6.1	7.3	4	4	4
24	Dβ02-120°	3	4	6	10	8	5	3	2.3	5.8	5	4	4
25	Dβ02-120°	5	3	3	9	8	12	2.7	4.5	5.1	6	6	6
26	Dβ02-180°	5	5	3	9	8	10	6.9	4.7	2.5	5	4	6
27	Dβ02-180°	3	5	4	16	6	9	2.9	0.8	4.7	8	2	4
28	Dβ02-180°	6	7	2	8	8	11	2.2	1.6	2.9	4	3	5

Table 9: All calculated values for contiguity, including averages and standard deviations are included here. Particularly low contiguity values, as defined in Chapter 4.4. Discussion, are underlined.

No.	Sample	C_{WC}			$\bar{C}_{WC}$	Std_C	$\bar{C}_{WC, Specimen}$	$Std_{C, Specimen}$	$\bar{C}_{WC, Depth}$		
-	-	L1	L2	L3	-	-	-	-	-		
1	Dβ04-0°	0.55	0.38	0.75	0.56	0.15					
2	Dβ04-60°	0.57	0.67	0.53	0.59	0.06	0.49	0.16			
3	D̲β̲0̲4̲-̲6̲0̲°̲	0.43	0.24	0.26	0.31	0.09					
4	Dβ01-0°	0.40	0.38	0.32	0.37	0.04					
5	Dβ01-0°	0.48	0.44	0.50	0.47	0.02					
6	Dβ01-60°	0.14	0.60	0.67	0.47	0.23					
7	Dβ01-60°	0.50	0.15	0.55	0.40	0.17	0.43	0.13	0.48	0.45	0.43
8	D̲β̲0̲1̲-̲1̲2̲0̲°̲	0.50	0.40	0.13	0.34	0.16					
9	Dβ01-120°	0.60	0.50	0.29	0.46	0.13					
10	Dβ01-120°	0.40	0.50	0.56	0.49	0.06					
11	Dβ03-0°	0.48	0.43	0.29	0.40	0.08					
12	Dβ03-0°	0.63	0.31	0.56	0.50	0.14					
13	Dβ03-0°	0.50	0.56	0.55	0.53	0.02					
14	Dβ03-60°	0.56	0.29	0.38	0.41	0.11	0.43	0.14	$s_{C, Depth}$		
15	Dβ03-60°	0.56	0.54	0.32	0.47	0.11			-		
16	D̲β̲0̲3̲-̲1̲2̲0̲°̲	0.32	0.13	0.33	0.26	0.09					
17	Dβ03-120°	0.40	0.75	0.33	0.49	0.18					
18	Dβ03-120°	0.63	0.18	0.40	0.40	0.18					
19	Dβ02-0°	0.59	0.56	0.40	0.52	0.08					
20	Dβ02-0°	0.40	0.57	0.52	0.50	0.07					
21	Dβ02-60°	0.48	0.50	0.53	0.50	0.02					
22	Dβ02-60°	0.47	0.44	0.40	0.44	0.03			0.11	0.16	0.15
23	Dβ02-120°	0.60	0.43	0.43	0.49	0.08	0.48	0.18			
24	Dβ02-120°	0.38	0.50	0.71	0.53	0.14					
25	Dβ02-120°	0.53	0.43	0.33	0.43	0.08					
26	Dβ02-180°	0.53	0.56	0.38	0.49	0.08					
27	Dβ02-180°	0.27	0.63	0.47	0.46	0.14					
28	Dβ02-180°	0.60	0.64	0.27	0.50	0.17					

Table 10: All calculated values for the mean free path of Co are listed here, the conversion ratio from cm to µm was 2/2.2 for Dβ04-0° and 1/1.8 for the rest. Particularly low mean free path values (as defined in Chapter 4.4. Discussion) are cursive, those with particularly high values bold.

Nr.	Sample	I_{Co}			$\overline{T}_{Co}$	$Std_{\overline{T}}$	$\overline{T}_{Co, Specimen}$	$Std_{\overline{T}, Specimen}$	$\overline{I}_{Co, Specimen}$		
-	-	L1	L2	L3	-	-	-	-	-		
		µm	µm	µm	µm	µm	µm	µm	µm		
1	**Dβ04-0°**	0.45	0.47	2.00	0.97	0.73	0.57	0.47			
2	*Dβ04-60°*	0.26	0.17	0.36	0.26	0.08					
3	Dβ04-60°	0.42	0.56	0.43	0.47	0.06					
4	Dβ01-0°	0.83	0.47	0.74	0.68	0.15	0.57	0.17	0.53	0.48	0.64
5	Dβ01-0°	0.38	0.63	0.48	0.50	0.10					
6	Dβ01-60°	0.83	0.33	0.78	0.65	0.22					
7	*Dβ01-60°*	0.44	0.31	0.44	0.40	0.06					
8	Dβ01-120°	0.78	0.81	0.60	0.73	0.09					
9	Dβ01-120°	0.52	0.65	0.26	0.48	0.16					
10	Dβ01-120°	0.66	0.29	0.65	0.53	0.17					
11	Dβ03-0°	0.75	0.68	0.47	0.63	0.12	0.54	0.24			
12	Dβ03-0°	0.83	0.43	0.21	0.49	0.26					
13	Dβ03-0°	0.91	0.37	0.33	0.54	0.26					
14	Dβ03-60°	0.44	0.27	0.48	0.40	0.09			$s_{\overline{T}, Specimen}$		
15	Dβ03-60°	0.68	0.29	0.29	0.42	0.18			µm		
16	Dβ03-120°	0.45	0.58	0.60	0.54	0.07					
17	**Dβ03-120°**	0.56	0.89	1.32	0.92	0.31					
18	*Dβ03-120°*	0.28	0.23	0.63	0.38	0.18					
19	Dβ02-0°	0.57	0.31	1.30	0.73	0.42	0.54	0.27			
20	Dβ02-0°	0.37	0.69	0.57	0.54	0.13					
21	Dβ02-60°	0.57	0.72	0.79	0.70	0.09					
22	Dβ02-60°	0.51	0.61	0.57	0.56	0.04			0.21	0.21	0.39
23	**Dβ02-120°**	0.63	0.85	1.01	0.83	0.16					
24	Dβ02-120°	0.33	0.32	0.81	0.49	0.23					
25	*Dβ02-120°*	0.25	0.42	0.47	0.38	0.09					
26	Dβ02-180°	0.77	0.65	0.23	0.55	0.23					
27	*Dβ02-180°*	0.20	0.22	0.65	0.36	0.21					
28	*Dβ02-180°*	0.31	0.30	0.32	0.31	0.01					